Controllable Self-Assembly of Nanostructured Artificial Pinning Centers (APCs) in High Temperature Superconductor Epitaxial Thin Films

By

Bibek Gautam
Department of Physics and Astronomy
The University of Kansas, Lawrence, KS

Submitted to the graduate degree program in Physics and Astronomy, the College of Liberal Arts and Science in partial fulfilment of the requirements for the degree of

Doctor of Philosophy

Chair: Judy Wu, PhD, University distinguished Professor

Siyuan Han, PhD, Professor

Michael J. Murray, PhD, Professor

Wai-Lun Chan, PhD, Associate Professor

Cindy L. Berrie, PhD, Professor

Date defended: May 07, 2019

The dissertation committee for **Bibek Gautam** certifies that this is the approved version of the following dissertation:

Controllable Self-Assembly of Nanostructured Artificial Pinning Centers (APCs) in High Temperature Superconductor Epitaxial Thin Films

_____
Judy Wu, PhD,
University distinguished Professor
Chair of Committee

Date Approved: July 12, 2019

Abstract

A Superconductor exhibits dc zero-resistance below a critical temperature (T_c). The possible uses of superconductors in a high temperature range of 50-77 K are greatly expanded by the discovery of high temperature superconductors (HTS) in 1986. One of the most important parameters for the industrial applications of high temperature superconductors (HTS) is a high value of critical current density J_c, in applied magnetic fields (H) up to tens of Teslas. In HTS, magnetic flux would be expected to penetrate the superconductor in the form of filaments containing one flux quantum (Φ_o) in each filament. These flux lines are surrounded by circulating current that acts as screening current and give rise to the mixed state known as vortex state. Application challenges involve preventing vortex motion in HTS and determining the high value of J_c at the high magnetic field (H). The vortex motion increases with increasing applied field and hence decreases the J_c due to dissipation induced by the vortex motion. Obtaining a high $J_c(H)$ requires stoppage of vortex motion in HTS. This can be done using pinning centers which capture the vortices and prevent their motion. Therefore, reaching high $J_c(H)$ in HTS requires the insertion of strong pinning centers of dimension comparable to the superconducting coherence length on the order of few nanometers. Such pinning centers improve the critical current density and strengthen the pinning force density. Various innovative approaches have been developed in the last decade to generate optimally efficient artificial pinning centers (APCs) in $YBa_2Cu_3O_{7-x}$ (YBCO) nanocomposite films. However, controllable generation of self-assembled nanostructures during sample growth stage remains a challenge. Therefore, in this study, we generate a landscape of one-dimensional (1D) plus three-dimensional (3D) APCs of flexible elastic materials to improve strong and

isotropic pinning which is beneficial for many industrial applications such as motors and generators. Specifically, a study of 3 vol.% Y_2O_3+2-6 vol.% $BaHfO_3$ (BHO) double doped $YBa_2Cu_3O_{7-x}$ epitaxial thin films is carried out and compared to the same concentration of $BaZrO_3$ (BZO) doping materials to explore the morphologic adaptation of the *c*-axis aligned 1D APCs to the 3D APCs. A significant reduction of J_c anisotropy is found for low doping $BaHfO_3$ and 3 vol.% Y_2O_3 doped YBCO nanocomposite films (BHO double doped films). The self-assembly of 1D APCs in YBCO film matrix driven by the strain field is influenced by the lattice mismatch at the APC/YBCO interface. To answer the fundamental question on how the pinning efficiency of 1D APCs is affected by the APC/YBCO interface, electrical transport properties J_c (*H*, *T*) of the comparable diameter of $BaZrO_3$ and $BaHfO_3$ 1D APCs on single doped YBCO nanocomposite films have been studied. The pinning force density is found to be significantly larger for a coherent, a less defective, BHO 1D APC/YBCO interface compared to a semicoherent, defective and oxygen deficient, BZO 1D APC/YBCO interface of epitaxial YBCO nanocomposite thin films. Transmission Electron Microscopy (TEM) images are utilized to study the difference of the nanostructures' morphology, and 1D APC/YBCO interface of single and double doped nanocomposite thin films. It is found that less rigid BHO material forms a mixed APCs morphology reducing J_c anisotropy to about 20 % for 2 vol.% BHO double doped YBCO thin film at temperature of 65 K and at magnetic field of 9.0 T. A coherent APC/YBCO interface enhances the pinning efficiency of 1D APCs in BHO doped YBCO thin films. Significantly reduced pinning efficiency of BZO 1D APCs is observed for a defective BZO/YBCO interface. A method of repairing defective APC/YBCO interface through calcium doping is explored and recommended to enhance the pinning efficiency of one-dimensional APCs.

This work is dedicated to my respected parents

Mr. Chakrapani Gautam and Ms. Kapila Gautam

and

to my beloved Family

Ms. Bindu KC, Avighna Gautam and Shaleen Gautam

Declaration

I hereby declare that except where otherwise stated, the contents in this dissertation is the result of my own work. Any outcomes of the work done in collaboration are duly acknowledged**.** The results have not been submitted in whole or in part for consideration for any other degree or qualification in the University of Kansas, or any other University. This dissertation contains less than 34,000 words including bibliography, footnotes, figures, tables, and equations, and has less than 43 figures.

Bibek Gautam

May 07, 2019

Acknowledgements

I would like to express my sincere thanks to my committee chair, Dr. Judy Z. Wu, for all her advice and encouragement during the PhD research journey. A big thanks for the opportunity to work in the field of superconductor thin films fabrication and characterization, providing constant mentorship during past years. I would also like to express special thanks to all my committee members for their valuable time, support, and dedication: Dr. Michael J. Murray, Dr. Siyuan Han, Dr. Wai-Lun Chan, and Dr. Cindy L. Berrie. I also would like to express my appreciation to academic graduate advisors for their advice at the beginning days of my graduate study and continuous encouragement in this journey.

My thanks go to collaborators at Air Force Research laboratory (AFRL) Dr. Mary Ann Sebastian, Dr. Timothy Haugan for making samples for us as well as providing XRD data for the crystallinity of the thin films. All the $BaHfO_3$ singled doped, and $BaHfO_3$ plus Y_2O_3 double doped $YBa_2Cu_3O_{7-x}$ samples were prepared by AFRL research group. In addition, the crystallinity of these samples were checked by the same research group. I appreciate Dr. Haiyan Wang's research group at Purdue University for the high-quality TEM images of the $BaHfO_3$ single and double doped YBCO thin films presented in this dissertation. In addition, TEM images for $BaZrO_3$ doped YBCO films in this work were obtained from the AFRL research group. Silver electrodes deposition in all samples using DC sputtering high vacuum system, microbridge pattern development utilizing standard photolithography, thickness of the films utilizing profilometer, wiring of the samples, and electrical transport measurements of these samples, for examples, *R-T*

curves for T_c measurements, and *I-V* curves for critical current density (J_c) were carried out at Wu research laboratory at the University of the Kansas.

I would also like to acknowledge all my colleagues and co-workers for their support and assistance in keeping the lab run smoothly. This work would not be complete without funding support from NSF contracts Nos: NSF-DMR-1337737 and NSF-DMR-1508494, the AFRL Aerospace Systems Directorate, the Air Force Office of Scientific Research (AFOSR), and the U.S. National Science Foundation (DMR-1565822) for TEM characterization, special thanks to them.

The most important, I am greatly indebted to all my family member for their kind encouragement and support during my studies over the past many years of my high school to PhD research work. The help, encouragement and constant love from my father, Mr. Chakrapani Gautam, mother Ms. Kapila Gautam, and siblings, Bishal, Pratibha and Pratikhsha Gautam all made it possible for me to complete most of my educational journey. Thanks to all my immediate family members, friends, to whom I spent most of the time during my growth who each played a unique and significant role.

My deepest and utmost appreciation goes to my Love, my wife, Dr. Bindu KC. Any of my work during graduate study would be mute without her endless support and help. There are no words to express my gratitude and to express my deepest love to you. My little ones: son Avighna Gautam and daughter Shaleen Gautam for bringing love and happiness in my family and taking all the tiredness of work away. I spent most precious and memorable time in your childhood.

Contents

List of Figures

List of Tables

Symbols

APC	Artificial pinning centers
D	Diameter
F_L	Lorentz Force
F_p	Pinning force density
I_c	Critical current
H	Applied magnetic field
H^*	Accommodation field
HTS	High temperature superconductor
J_c	Critical current density
J_{dp}	Depairing current density
k_B	Boltzmann constant
PLD	Pulsed Laser Deposition
R	Resistance
T	Temperature
T_c	Critical temperature
λ	Penetration depth of magnetic field
ξ	Coherence length of superconductor
ρ	Resistivity
$\mu\Omega$	microohm

Chapter 1 Introduction

1.1 Superconductivity: an overview

Superconductivity is a phenomenon of zero dc electrical resistance of the materials when cooled below characteristic critical temperature (T_c). Superconductors were first noted by Kammerlingh Onnes during resistivity measurements of mercury at 4.2 K in 1911 [1]. The phenomenon of superconductivity exhibits a transition of metal from a normal state to a superconducting state at T_c involves the second order phase transition (i.e. there is no latent heat involves in the phase transition) [1]. For the thermodynamic phase transition to happen, the overall free energy must be lower in the superconducting state than in the normal state. When a superconductor is cooled to below T_c, it expels magnetic field from its interior**,** an effect that was observed by Meissner and Ochsenfeld in 1933 [2, 3]. Aside from having zero resistance below T_c, Meissner also observed that when a superconductor is placed in a magnetic field, the field is abruptly expelled from the bulk of the material, that is, magnetic induction $B = 0$ and the material becomes perfectly diamagnetic [1]. In addition, superconducting properties of the materials are destroyed with the application of an external magnetic field above a critical field (H_c). This phenomenon was first observed by K. Onnes in 1914 [1]. On the other hand, a pure "zero resistance" conductor would not be expected to follow the Meissner effect, but would be expected to set up a current that prevents the internal flux from changing with the variation of the externally applied magnetic field. For a superconductor, the critical field (H_c) can be defined in terms of the difference between the free energy densities in the normal state and the superconducting state. For example, for a long thin superconductor in a parallel field, the critical field can be estimated as $\frac{H_c^2(T)}{2} \sim f_n(T) - f_s(T)$ where f_n and f_s are the free energy densities of the normal and superconducting

states and are functions of temperature [1]. These observations imply that a superconducting material has a limitation to its current carrying capability in the superconducting state.

In the superconducting state at $T<T_c$, Cooper pairs, paired electrons, are formed through phonon-mediated interaction and steer through the crystal lattice without any collision, leading to no resistance [2]. This phenomenon was first explained by Bardeen, Cooper, and Schrieffer (BCS) in 1957. The BCS theory is a complete quantum mechanical microscopic description of superconductivity and it applies to any phonon-mediated pairing mechanism, irrespective of T_c**.** An electron moving through the crystal lattice with momentum k distorts the lattice and gets scattered by creating a virtual phonon. This phonon of momentum q is absorbed by a second electron with momentum k', which gets scattered with a momentum k'+ q (Figure 1) [1]. This leads to an effective attractive interaction between electrons and forms a Copper pair. The formation of Copper pairs can be depicted in the Feynman diagram shown in Figure 1.

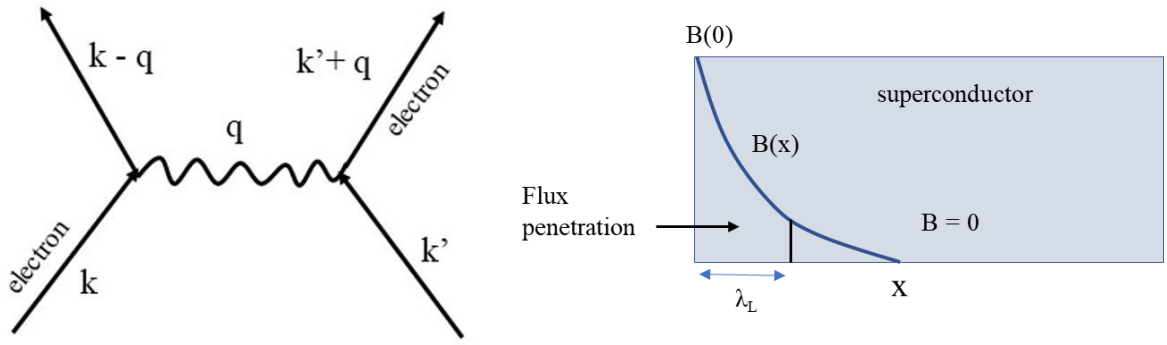

Figure 1: Left: Feynman diagram of a Cooper pair. Right: a schematic of flux penetration in superconductor over the distance λ, the penetration depth.

The electrons forming the Cooper pairs have equal and opposite momentum. In addition, the electron pairs have total zero spin because they are composed of two electrons with opposite spins.

This suggests that the Cooper pairs may have the same quantum state at the same time. The Cooper pairs occupy a condensed momentum state. The net interaction of the paired electrons mediated by the phonon occurs within a very small energy range $\hbar\omega_D$ where ω_D is the Debye frequency [1]. Thus, in a superconducting state, all Cooper pairs can move together and are correlated. Furthermore, each Cooper pair occupies a volume characterized by the dimensions equivalent to the coherence length (ξ). However, the exact nature of the pairing in high temperature superconductor has not been determined.

To explain the Meissner effect, Fritz and Heinz London (1935) proposed a model describing electrodynamics in superconductors [2, 3]. This model was not derived from the first principle but justified from the observations of the behaviors related to the electromagnetic fields in and around the superconductors [2, 3]. Therefore, it is a phenomenological theory. According to the London theory, superconductivity arises from superelectrons different from normal electrons. The following two equations are added to the Maxwell's equations:

$$\boldsymbol{E} = \frac{m}{ne^2}\boldsymbol{J} = \mu_o\lambda_L^2\boldsymbol{J} \qquad (1)$$

where $\lambda_L = \sqrt{\frac{m}{\mu_0\, n_s e^2}}$ is the London penetration depth and μ_o is the permeability of free space.

$$\mu_o\lambda^2\nabla\times\boldsymbol{J} + \boldsymbol{B} = 0 \qquad (2)$$

$\boldsymbol{J} = ne\boldsymbol{v}$ is the current density. The *m*, *e*, and *n* are the mass, charge, and number density of charge carriers. Applying Maxwell's equation $\nabla\times\boldsymbol{B} = \mu_o\boldsymbol{J}$ and further simplifications of Equation (2), Equation (3) can be obtained.

$$\nabla^2 \boldsymbol{B} = \frac{1}{\lambda_L^2} \boldsymbol{B} \qquad (3)$$

For a semi-infinite thin slab of superconductor (Figure 1) and the applied field perpendicular to the surface of the superconductor, a solution of this equation can be written as

$\boldsymbol{B}(x) = \boldsymbol{B}(0) \exp(-x/\lambda_L)$**.** For $x >> \lambda_L$, $\boldsymbol{B}(x)=0$, in accordance with the Meissner effect [1]. The London equation describes for a finite penetration of the applied magnetic field over a characteristic length λ_L and is known as the London penetration depth.

Ginzburg-Landau (G-L) theory (1950) described the simultaneous presence of both normal and superconducting electrons at a temperature below critical temperature ($T < T_c$). The superconducting electrons were described by an order parameter in the form of wave function ψ. The normalized wave function $|\psi|^2 = n_s$ provides the number density of superconducting electrons. G-L theory also introduced the concept that the free energy might also depend on the derivative of ψ in space. The G-L theory and equations can be found in several references [2, 3]. The general form of the Ginzburg-Landau free energy expression in the presence of an external magnetic field is represented by Equation (4).

$$f_s = f_n + a(T)|\psi|^2 + \frac{1}{2} b(T)|\psi|^4 + \frac{1}{4m}\left|\left(\frac{\hbar}{i}\nabla - \frac{2e}{c}\boldsymbol{A}\right)\psi\right|^2 + \frac{1}{2}\mu_o H^2 \qquad (4)$$

where f_s and f_n are the free energy densities of superconducting and normal states, *a* and *b* are temperature dependent coefficients, *m* and *e* are the mass and charge of the electron respectively,

and *A* is the vector potential. Minimizing this free energy with respect to ψ and *A* respectively, the following two G-L equations can be obtained

$$a(T)\psi + b(T)|\psi|^2\psi + \frac{1}{4m}\left(\frac{\hbar}{i}\nabla - \frac{2e}{c}\boldsymbol{A}\right)^2\psi = 0 \qquad (5)$$

$$\boldsymbol{J} = \frac{ie\hbar}{m}(\psi^*\nabla\psi - \psi\nabla\psi^*) - \frac{4e^2}{mc}\boldsymbol{A}|\psi|^2. \qquad (6)$$

Equation (5) describes the equilibrium spatial variation of ψ. As expected, order parameter ψ is zero in the center and recovers its maximum value at the distance of ξ. Equation (6) gives the current density and describes the supercurrent distribution in the superconductor. From the G-L Equations (5) and (6) two parameters can be obtained. The coherence length $\xi(T) = \frac{\hbar}{[2ma(T)]^{\frac{1}{2}}}$ is the characteristic length for the decay of small perturbation in the superconducting order parameter, where *a*(*T*) is a constant [1]. The G-L penetration depth can be obtained as $\lambda(T) = \left[\frac{mc^2 b(T)}{4\pi e^2 a(T)}\right]^{\frac{1}{2}}$, where *c* is the velocity of light. Ginzburg-Landau penetration depth is, like the London penetration depth as discussed in the previous paragraph, a characteristic length for the decay of the magnetic field in a superconductor.

Type I superconductors have only one critical field H_c. These superconductors return to a normal state when the applied field exceeds the critical field H_c. Type II superconductors have a lower critical field (H_{c1}) and an upper critical field (H_{c2}) as shown in Figure 2. Abrikosov (1957) noted that the ratio of $\frac{\lambda}{\xi}$ is less than $\frac{1}{\sqrt{2}}$ for type I superconductors. For $\frac{\lambda}{\xi} < \frac{1}{\sqrt{2}}$, the surface energy between the normal and superconducting phases is positive. The Meissner effect is observed below H_c in type I superconductors while in type II superconductors, this effect is

observed when $H_c < H_{c1}$. In type II superconductors, $\frac{\lambda}{\xi} > \frac{1}{\sqrt{2}}$. For $\frac{\lambda}{\xi} > \frac{1}{\sqrt{2}}$ however, the surface energy of the interface between the normal and superconducting phases is negative and it will, therefore, be energetically favorable for flux to exist within the superconducting material [3, 4]. Abrikosov predicted that the magnetic flux would penetrate the superconductor in the form of filaments (flux lines) surrounded by the circulating current and form the vortices.

In type II superconductors, superconductivity exists through the mixed phase, known as vortex state, when the field is increased above H_{c1} (see Figure 2). When the magnetic field is increased from zero to H_{c1}, the magnetic flux is completely excluded as in a type I superconductor and superconductivity exists until the field reaches the upper critical point H_{c2}. The normal state again is restored above the upper critical field H_{c2}.

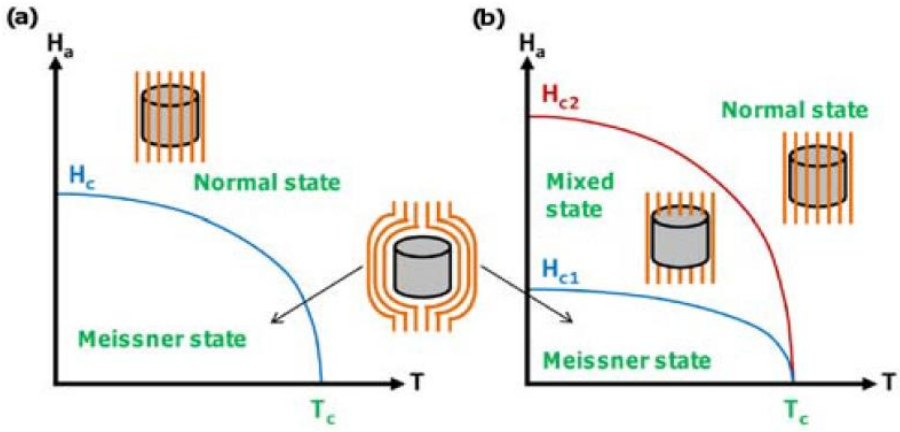

Figure 2: Schematic of a phase diagram of type I (a) and type II (b) superconductors showing normal state, Meissner state, and mixed state. This Figure is adapted from Norton et.al, MSE Report, 2004 [5].

Vortices are introduced when the field reaches the H_{c1}. As the applied magnetic field is increased beyond the H_{c1}, more and more vortices enter the superconductor. Each vortex generates a microscopic field at the same orientation and hence they experience a repulsive force from

neighboring vortices. The co-existence of the superconducting phase with the normal phase penetration by a magnetic field in $H_{c1} < H < H_{c2}$ is shown in Figure 2(b). The magnetic field is at maximum at the center of the vortex and decays exponentially away from the center with the characteristic length λ [2].

Vortices are the quantization of flux formed in superconductors. Each vortex carries a flux quantum, a constant quantity, $\Phi_o = h/2e = 2.07\times10^{-15}$ Tm^2 that runs parallel to the applied field (H), and h is the Planck's constant. Increasing H increases the number density of vortices that is number of vortices per unit area (n) with relation $H = n\Phi_o$. At the field $H=H_{c2}$, the vortex lattice becomes so dense that the spacing of the vortices is at the order of ξ. The coherence length (ξ) measures the distance between the paired electrons that form the Cooper pairs and is equivalent to the radius of the normal core of the vortices as shown in Figure 3 [2]. This means that at $H=H_{c2}$, the normal cores of the vortices come in contact with each other. The superconducting order parameter becomes zero ($\psi=0$) in the normal core of the vortex and reaches its maximum ($\psi=1$) in the superconducting region. Beyond H_{c2}, the cores of the neighboring vortices overlap and superconductivity is lost.

In $YBa_2Cu_3O_{7-x}$ (YBCO), a type II superconductor, the approximate values of these parameters are $\xi_c \sim 0.14 – 0.8$ nm, $\xi_{ab} \sim 1.2 – 4$ nm, $\lambda_c \sim 800 – 1121$ nm, and $\lambda_{ab} \sim 150 – 210$ nm, where the subscripts denote the length along the *c*-axis and *ab*-plane, respectively. The lower values listed are for $T = 0$ K and larger for $T = 77$ K [3, 4].

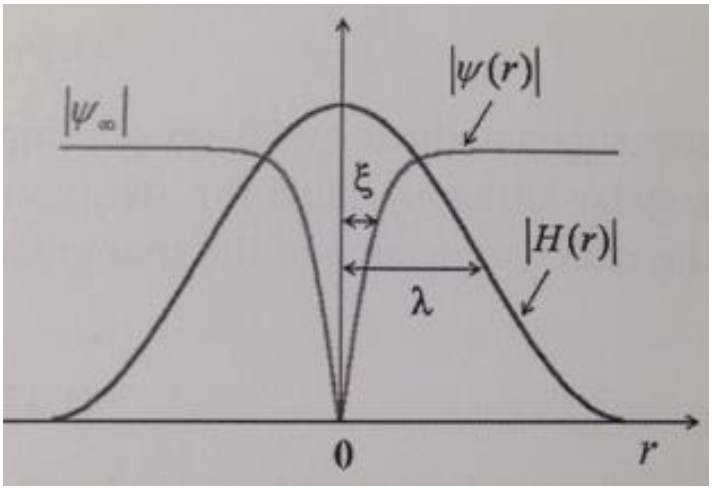

Figure 3: Spatial variation of the superconducting order parameter and field for isolated vortex. This Figure is adapted from Kittel C., Wiley, 2004 [2].

The depairing current density (J_{dp}) is a maximum theoretical limit of the current carrying capability of a superconductor before losing its superconductivity. The J_{dp} becomes zero at critical temperature (T_c) and field (H_c for type I superconductor and H_{c2} for type II superconductor). Type II superconductors have high critical current densities in large magnetic field. The depairing current density in the superconducting state of a type II superconductor can be estimated using Equation (7).

$$J_{dp} = {}^{y\Phi_o}/_{\lambda^2 \xi}, \quad \text{y is a constant.} \qquad (7)$$

For a type II superconductor such as $YBa_2Cu_3O_{7-x}$, the magnitude of the J_{dp} is about 10^8 A/cm^2 at 77 K [3]. However, in practice J_c is approximately two orders of magnitude smaller than the theoretical limit due to vortex motion. Typically, the experimental J_c is about 2-4×10^6 A/cm^2 for $YBa_2Cu_3O_{7-x}$ (YBCO) thin film at 77 K. To increase the J_c, the vortices need to be pinned. The ideal pinning entities should have a dimension as small as the vortices with radius ~ξ and number

density equivalent to the number of vortices at upper critical field H_{c2}. The upper critical field, the point at which the nucleation of superconducting regions occurs, can be calculated utilizing

$$H_{c2} \sim \frac{\Phi_0}{\pi \xi^2} \tag{8}$$

The general form of the depairing current density can be derived as follows.

$$\boldsymbol{J}_{dp} = n_s e \boldsymbol{v} \tag{9}$$

Where n_s is number density of electrons, e is the charge, and $\boldsymbol{v}$ is the velocity of electrons. At $T=T_c$, thermal energy ($k_B T_c$) is equal to depairing energy (the energy that breaks a Cooper pair into two normal electrons) of a Cooper pair in terms of energy gap (Δ) as given by Equation (10).

$$\gamma k_B T_c = 2\Delta, \tag{10}$$

where $\gamma = 3.52$ is a universal constant value regardless of material's nature according to BCS theory [1]. Equation (11) represents the relation of maximum energy of a Cooper pair in terms of velocity and gap energy where m^* is the mass of a Cooper pair (=2 m, m is the mass of a single electron)

$$\frac{1}{2} m^* v^2 = 2\Delta \tag{11}$$

Using Equations (10) and (11), Equation (9) can be written as the depairing current density

$$\boldsymbol{J}_{dp} = n_s e \sqrt{\frac{2\Delta}{m}} \tag{12}$$

Considering $n_s = 10^{28}$ /m^3, e =1.6×10^{-19} C, m =9.11×10^{-31} kg, T_c = 91 K for YBCO and k_B=0.86×10^{-4} eV/K, the depairing current density is estimated to be about 10^8 A/cm^2.

Unfortunately, the theoretical limit of the depairing current density $\boldsymbol{J}_{dp}$, has not been achieved so far in YBCO superconductor experimentally**.** Thus, the fundamental questions arise: what really limits the J_c in this type of superconductor and how high of J_c values can be achieved. One of the motivations to work in this field is to explore the answers of these questions through electrical transport measurements of YBCO at the high magnetic field.

1.2 High temperature superconductors

The 1986 discovery of high temperature superconductors (HTSs), such as $YBa_2Cu_3O_{7-x}$ (YBCO), which has a superconducting critical temperature T_c ~ 91 K [6, 7], well above the boiling point of liquid nitrogen (77 K), triggered a worldwide effort to push industrial applications. High temperature superconductors are type II superconductors. The last few decades have witnessed exciting progress [8-12]. The compound YBCO is one of the most promising for industrial applications. It is the least anisotropic (~5-7) and has a high H_{c2} (>80 T). One of the most important parameters for applications is the electrical current carrying capability, measured by critical current density J_c, in applied magnetic fields (H) in the range of few to tens of Teslas. For example: motors and generators require uniform J_c at the varying magnetic field orientations and at the range of 3-5 T, while high temperature superconductor (HTS) coated conductors (CCs) need to carry larger J_c, on the order of thousands of amperes per squared centimeters at 77 K. The world's first high temperature superconductor power transmission cables on a commercial power grid can transmit a 575 MW of electric power. HTS transformers cooled by liquid nitrogen generate significantly less heat waste than conventional oil cooled voltage transformers. Significant progress has been made by the research community to improve critical current density (J_c) in YBCO thin films and in coated conductors for power applications. Key to the high J_c (H) in HTS are strong effective

artificial pinning centers (APCs) of dimensions comparable to the superconducting coherence length, a few nanometers, that can pin the flux lines at higher fields and higher temperatures.

Despite the exciting progress of vortex pinning in HTS, there are several factors that obstruct the enhancement of J_c and the practical application of HTS materials. One of the major hurdles is to minimize the fast drop of J_c with the application of a magnetic field. In addition, flexibility to meet the demand of the practical applications of HTS materials through strong and isotropic vortex pinning is a challenging task and is still lacking. A big challenge to realize strong and isotropic pinning is to generate a landscape of APCs that is optimal for that purpose. A controllable generation of APCs through low-cost strain-mediated self-assembly of APCs during $YBa_2Cu_3O_{7-x}$ (YBCO) nanocomposite thin film growth stage is even more challenging. The strained YBCO lattice due to insertion of the APCs introduces a large amount of strained and defective interfaces through epitaxy of APCs in the epitaxial YBCO lattice. This results in a reduction of both J_c and the pinning efficiency of APCs. Achieving a quantitative evaluation of the interplay between the pinning efficiency and the interface quality is critical to engineering (or repairing) such an interface for optimal pinning efficiency. The first part of the dissertation focuses on how to create self-assembled APCs with optimal dimensions, morphology, and concentrations to enhance and strengthen isotropic pinning. Additionally, we aim to explain the effect of the APC/YBCO interface on pinning efficiency of 1D APCs both qualitatively and quantitatively.

Experimentally it has been found that the materials with a higher rigidity tend to form *c*-axis (axis along the thickness of the YBCO film) aligned 1D APCs (for examples, $BaZrO_3$ and $BaSnO_3$) while the materials with lesser rigidity (for example, $BaHfO_3$) may tend to form misaligned 1D APCs away from *c*-axis and mixed (1D+2D+3D) APCs [13]. The $BaHfO_3$ may

create a coherent interface, a less defective and oxygen deficient interface, with YBCO matrix. On the other hand, the $BaZrO_3$ with higher rigidity in forming the *c*-axis aligned 1D APCs create a semicoherent interface. The former shows significantly higher pinning force density ($F_p=J_c \times H$) compared to the latter. In addition, microstructure analysis has revealed that a nanocolumn of width 1-2 nm close to the BZO 1D APC/YBCO interface forms a defective interface leading to an oxygen deficient column, which is semicoherent in nature. This reduces the pinning force density significantly due to lowering the pinning potential energy of the YBCO column. Such oxygen deficient columns can be repaired using calcium rich materials.

A record high maximum pinning force density ($F_{p,max}$) of the BHO material that forms a coherent interface with YBCO matrix is reported. The last part of the of this dissertation explains the calcium (Ca) induced repair mechanism for the defective YBCO column in 6 vol.% BZO/YBCO and $Ca_{0.3}Y_{0.7}Ba_2Cu_3O_{7-x}$ (CaY-123) multilayers (ML) films. The thickness of the CaY-123 spacer layers would be approximately 5-15 nm in between the thickness of 50 nm of 6 vol.% BZO/YBCO layers. A record high pinning force density of 6 vol.% BZO doped multilayer (ML) nanocomposite films would be reported. Similarly, a ratio of the H_{max}, a maximum field at which $F_{p,max}$ is obtained, and matching field (H^*) will also be reported. The optimized growth parameters of ML films will be discussed, and the results of ML films will be compared to the same doping of a single layer film.

It is critical for the practical applications of HTS materials that the J_c should be independent of the magnetic field orientation and have strong isotropic vortex pinning, but that would require further study. Additionally, self-assembled *c*-axis aligned one-dimensional (1D) APCs are desirable to achieve strong correlated pinning [14] of the vortices when the applied magnetic field is parallel to the 1D APCs. The benefit of such 1D APCs is the constant F_p through HTS

nanocomposite film thickness. Such nanocomposite films can carry critical current density (J_c) values on the order of hundreds to thousands of Amperes per centimeter squared for power applications. However, the desirable high F_p value for 1D APCs is still not at its optimal value due to the insufficient information of the factors that influence pinning efficiency of pinning centers. This certainly requires further study.

1.3 Basic Physics of vortex pinning

In an HTS, vortices must be pinned since vortex motion induces dissipation and hence destroys superconductivity. The driving force of the vortex motion is called the Lorentz force density (force per unit volume) $\boldsymbol{F}_L$ represented by Equation (13) [4].

$$\boldsymbol{F}_L = \boldsymbol{J} \times \boldsymbol{H} \qquad (13)$$

Since $\boldsymbol{F}_L$ is proportional to $\boldsymbol{J}$ and $\boldsymbol{H}$, strongly pinned vortices are necessary to achieve high critical current in a high magnetic field. Pinning of vortices occurs when vortices move out of the equilibrium position to interact or accommodate the pinning centers. The pinning force density $\boldsymbol{F}_\mathbf{p}$, which could be compared to "friction force" in classical mechanics, describes quantitatively the pinning strength of individual pinning centers and the concentration of the pinning center per unit volume [15]. J_c is determined by the force balance equation (critical state).

$$\boldsymbol{F}_L = \boldsymbol{F}_p \qquad (14)$$

For an individual pinning center, the strength of the pinning force is proportional to the gradient of the order parameter across the interface between the normal and the superconducting regions [4]. The sharpness of the interface between the normal and the superconductor is therefore critical to achieve a high $\boldsymbol{F}_p$ on each individual pinning center. This is particularly important in

APC/YBCO nanocomposite because a strained APC/YBCO interface due to lattice mismatch and chemical inter-diffusion between APC and YBCO results in a poor interface with suboptimal pinning strength. In addition, if such an interface extends to finite thickness, it will waste a substantial portion of the superconducting phase, reducing the cross-sectional area of the superconductor for transport current. This latter issue becomes more significant at high concentrations (n = number of pinning centers per volume) of pinning centers. Considering one vortex pinned at one pinning center, the matching field $H_m = n\Phi_o$ illustrates a peak of pinning force density $\boldsymbol{F}_{p,\,max}$ that corresponds to the field H_{max} (these curves are shown in the latter sections of this dissertation). The peak value of the $\boldsymbol{F}_p$ at the H_{max} is an illustration of the pinning strength of the individual pinning center while the peak location H_{max} is proportional to the concentration of the pinning center.

1.3.1 Intrinsic pinning of YBCO and angular dependence of J_c

As shown in Figure 4, the insulating layer between copper oxide planes of the anisotropic layered structure of YBCO intrinsically provides strong vortex pinning. This kind of pinning is achieved when an external magnetic field is applied parallel to the *ab*-plane, which prevents the motion of the vortices driven by Lorentz force either toward the film thickness or toward the film-substrate interface depending on the direction of the flow of current. Considering orthorhombic crystal structure ($a \neq b \neq c$, axes are perpendicular to each other) in the *ab*-plane (a<b), the superconducting CuO_2 planes separated by an insulating block of a distance 0.828 nm thickness along *c*-axis greater than ξ_c, makes it weakly superconducting compared to the *ab*-plane.

Intrinsic pinning is more effective at lower temperatures T< 77 K, because ξ_c becomes much smaller than insulating block a distance of 0.828 nm [16, 17]. For H//*ab*-plane (F_L along *c*-

axis), strong intrinsic vortex pinning produces the peak in J_c. Figure 4 right shows a measurement at the angular dependence of J_c for an undoped YBCO film. The decreasing J_c peak for increasing magnetic field (H) indicates the decrement of J_c due to increasing vortex motion.

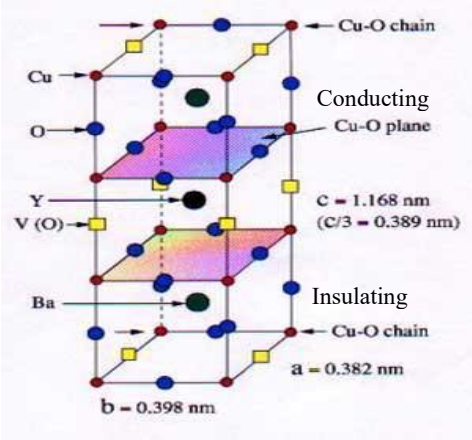

YBCO crystal structure

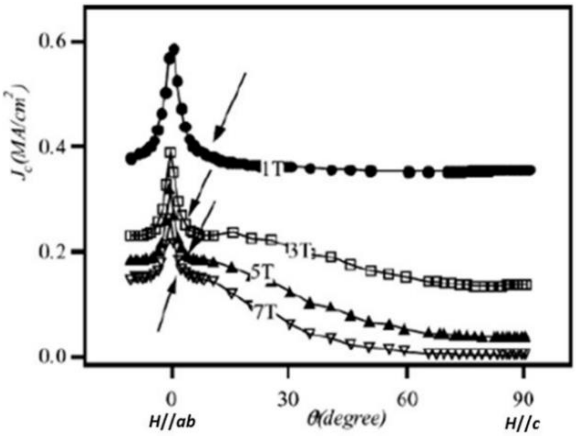

Figure 4: Left: The Structure of YBCO unit cells showing an insulating layer separated from conducting pathways and *c*-axis lattice. Right: Angular dependence of J_c of YBCO film as a function of magnetic field 1, 3, 5, and 7 T as labeled. θ=0 indicates field applied parallel to the *ab*-plane These Figures are adapted from Baca F., KU, 2009 [17].

In Figure 4 right (J_c vs. θ), there is no or a very small J_c peak observed when H//c-axis (defined as θ=90^o). This means that naturally present growth defects like voids, vacancies, stacking faults, and dislocations are not effective against high applied magnetic field when field is parallel to *c*-axis. These growth defects are low in number density (10^9-10^{10} cm^{-2}) and can provide strong vortex pinning for a small value of the applied magnetic field up to 1-2 T. Therefore these kinds of defects are considered weak pinning centers [18]. The J_c at zero magnetic field ($J_{c,\,self}$) of YBCO is typically a few MA/cm^2. It drops by a factor of 10 when H ~1 T, and further drops as H increases. This limits the high-field applications of YBCO. Researchers are motivated to generate strong APCs to provide strong vortex pinning against the high applied magnetic field (H). The $J_{c,\,self}$ decreases due to the addition of APCs by reducing the cross-sectional area of the superconductors.

At the same time, the vortex pinning by APCs increases the current density at the high applied field *H* [19].

1.4 Review of progress on vortex pinning in YBCO nanocomposite films via generation of Artificial Pinning Centers (APCs)

1.4.1 Design parameters of APCs

For the maximum efficiency, the dimensions of APCs should be as small as possible, typically comparable to the size of the vortices with a radius equivalent to ξ~0.2 nm at T=0 K for YBCO $\left(\xi \propto \left(1-\frac{T}{T_c}\right)^{-1}\right)$ [20]. Thus, the size of APCs should be approximately 1-2 nm at 4.2 K and 2-4 nm at 77 K [21]. In addition, the morphology and the orientation of APCs are crucial for strong pinning efficiency. Figure 5 shows a schematic of the needs of the industrial application of YBCO coated conductor device in terms of operating temperature (K) and magnetic field range (T) [21]. This encourages exploring the proper design of APCs that fit for different operating conditions. In low and moderate H ~ 2-3 T, the performance of HTS devices and systems has illustrated clear benefits over their conventional counterparts. For example, the mass of copper-based electronic design wind turbine can be reduced by 35%, increasing power from 5 MW to 8 MW. On the other hand, YBCO coated conductor transmission cables operating at 77 K reduce the energy loss by electric resistance of conventional conductors by one third and increase power density by 2 to 8 times in existing conditions.

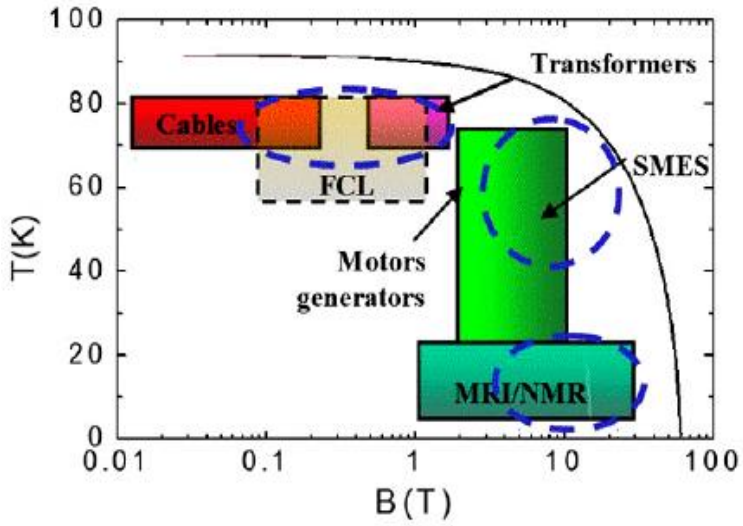

Figure 5: Schematic of the operating magnetic field and temperature of the YBCO coated conductor, FCL (fault current limiter), SMES (superconducting magnetic energy storage). This Figure is adapted from Obradors et.al, SuST, 2014 [21].

A 850 MVA superconductor transformer has benefits of both reduced physical size and weight by a factor of 7 and 5, respectively [5]. Other applications like generators and motors typically require H~3-5 T at different orientations. Superconducting magnetic energy storage (SMES) device requires even higher H~10-12 T at a high T >50 K. Research and development of HTS, especially in the form of wires and cables that can have high J_c at elevated temperatures, moderate to high H fields and orientations, has been a world-wide effort in applied superconductivity in the last few decades.

1.4.2 Morphology of APCs

Figure 6 shows the different types of APCs with possible pinning of vortices. As of now J_c (H) for 1D APCs (diameter (5-7 nm) separated at 10-15 nm) are seen to be effective at 77 K for H ~ 2 T when H//c-axis, with $F_{p,max}$ ~28.3 GN/m^3 & J_c =1.4 MA/cm^2 $BaSnO_3$ (BSO) and $F_{p,max}$~16 GN/m^3 & J_c ~ 1 MA/cm^2 $BaZrO_3$ (BZO) nanorods (NRs) [22]. Nanorods are cylindrically shaped,

one-dimensional nanostructure in the YBCO film matrix. Despite the high $J_c(H)$, isotropic pinning is not effective due to the small pinning portion of vortices by NRs and the small splaying angle (tilting angle of NRs from the *c*-axis of YBCO) ~10 degrees in the APC/YBCO nanocomposite. $BaHfO_3$ (BHO) 1D APCs (~4.5 nm) are seen to be effective for a slightly wide angular range (16^o), with $F_{p,max}$=24 GN/m^3 and J_c=2 MA/cm^2 (77 K, H//c-axis at 1.4 T) as reported in ref. [22].

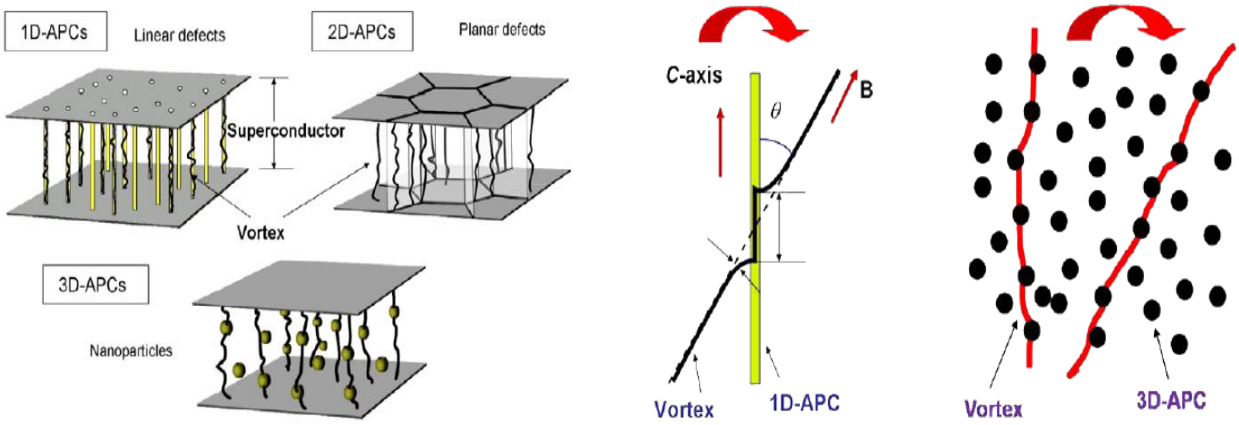

Figure 6: Left: Schematic of the different types of Artificial Pinning Centers (APCs), right: comparison of the vortex pinning by 1D and 3D APCs when magnetic field is tilted form the axial direction. This Figure is adapted from Obradors et.al, SuST, 2014 [21]

In terms of number density, in recent publications [8-10, 23], low temperature growth methods (<760^0 C) have been utilized to increase the number density of 1D APCs (claimed as 2.3×10^3 μm^2) for BHO doped (Sm, Gd) $Ba_2Cu_3O_7$ to enhance the J_c.

Figure 7 depicts the enhancement of J_c peak about 3.5 times when BZO or BHO APCs are added parallel to the *c*-axis of YBCO film measured at 77 K and 40 K respectively. However, drop of $J_c(\theta)$ in an angular range of 20-70 degrees (0.7 MA/cm^2 at H//c axis to ~0.4 MA/cm^2 when H is at 70 degrees) shows the limitations of BZO 1D APCs. A similar effect is observed in BHO doped

film as well. The J_c peak at H//ab-plane is due to intrinsic pinning as explained earlier. Increasing the angular range of $J_c(\theta)$, requires different dimensions of APCs other than NRs that provide isotropic pinning. Three dimensional (3D) APCs of 3-10 nm of Y_2O_3 (areal density ~$2x10^{11}$ cm^{-2} depending on doping concentration and growth conditions) at a distance 15-20 nm is shown to be effective for enhancing $J_c(\theta)$ with F_p ~14 GN/m^3 at 77 K for ~1 T. But J_c drops by a factor of 2 of the BZO/YBCO nanocomposite film for the same H at 77 K, when θ is changed [24, 25]. This indicates nanoparticles (NPs) alone don't seem to be effective for increasing $J_c(H, T, \theta)$. However, pinning

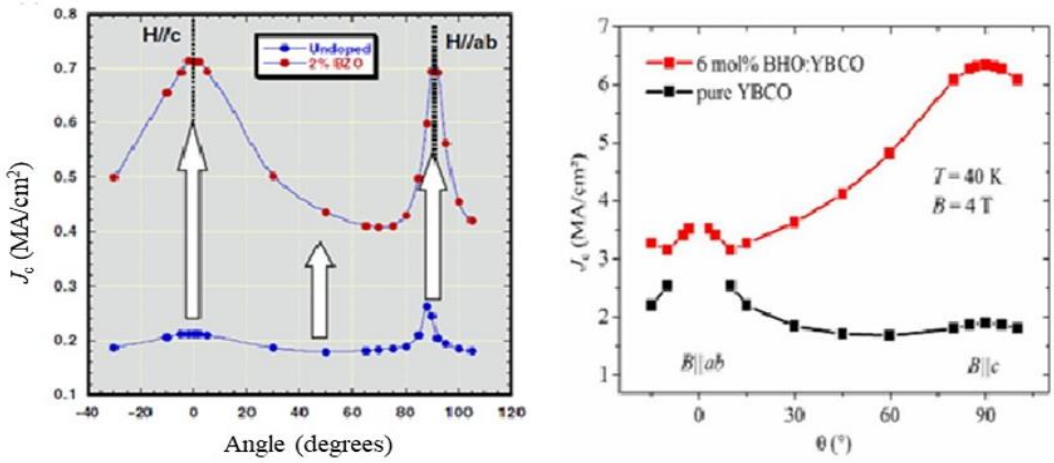

Figure 7 **:** Left: angular dependence of J_c at 77 K, 1 T for an undoped YBCO film compared to 2 vol.% BZO and right: 6 mol% BHO doped YBCO film. These Figures are adapted from Goyal et.al, SuST, 2005 and Pahlke et.al, IEEE TAS, 2016 [24, 25].

performance of 3D APCs increases with decreasing T, as do 1D APCs, but they overcome the pinning efficiency of 1D APCs at T < 40 K [15, 18, 26-28] due to the small size of 3D APCs. For higher T, they are not as effective as 1D APCs because of thermal fluctuations.

A mixed morphology of artificial pinning centers (1D+2D+3D APCs) enhances $J_c(H, \theta)$ for a wide range of H via isotropic pinning that is not present for 1D APCs alone. The effective number

density of APCs corresponds to the $H_{max} = n\Phi_o$ if each vortex is pinned by an individual APC. As explained earlier, increasing the BZO volume concentration increases the number density of effective APCs. It ultimately increases $J_c(H)$ at a higher applied magnetic field. Baca et al., shows that increasing the BZO content from 2 to 6 vol.% increases the number density of particles by a factor of approximately 1.8 on a flat STO substrate while the average size of individual particles is decreased by a factor of 1.4 [29]. 3D APCs with short segmented 1D APCs increases the number density and hence increases H_{max}. Therefore, for strong isotropic pinning, many mixed morphologies of APCs need to be created as reported in several publications [30-32]. In recent reports, the combination of BZO/BSO with Y_2O_3 (DD) has been shown to be effective, improving $J_c(H, \theta)$ (J_c ~1 MA/cm^2 at 77 K for 2 T) [33-35] in APC/YBCO nanocomposite film. On the other hand, mixed APCs morphologies have been created in varying BZO/YBCO nanocomposite growth conditions (5.2-5.9 nm NRs aligned along the *c*-axis and irregular shaped nanopatches 6-28 nm along *ab*-plane) on 5^o vicinal substrate. It shows a high J_c ~4 MA/cm^2 at 1.0 T for *H*//*c*-axis at 77 K [30]. The increased pinning efficiency of APCs in the films is due to the controlled lattice strain from the step structure of vicinal substrates in which the degradation of T_c of YBCO is minimal. However, the volume density (ρ_{film}~24%) of nanostructures is still low in those films compared to the nanocomposite films fabricated on flat substrates (~ 45 vol.% of nanostructures in total film surface for a perfect epitaxial film as in Ref. [36].

1.5 Remaining issues and challenges

Despite the exciting progress that has been made in enhancing J_c (*H*, T) in APC/ (RE=Y, Gd, Sm) $Ba_2Cu_3O_7$ (RE-123) nanocomposite thin films, challenges remain in controllable self-assembly of APCs with optimally designed dimension, morphology, areal density, and APC/RE-

123 interface. Little is known about the controlling parameters that determine the pinning efficiency of the 1D APCs quantitatively. The lack of sufficient study on parameters that control the optimum conditions of the APCs is another key challenge whose completion is necessary to further study of vortex pinning design parameters. The objective of this dissertation is, therefore, to elucidate the critical current density [$J_c(H)$], pinning forces density [$F_p(H)$], and matching field [(H_{max})], which is proportional to the effective number density of APCs. In addition, qualitative and quantitative evaluation of the interface effect on pinning efficiency of 1D APCs will be explored by comparing the matching field (the applied magnetic field at which maximum pinning force density is observed) and accommodation field (optimum limit of the field if each vortex is pinned by an individual APC and is calculated from the interspace between 1D APCs). This is achieved through the measurements of the transport critical current density at various temperatures, magnetic field strengths, and orientations. Furthermore, this dissertation covers the significance of the transport properties and nanostructures morphology.

The selection of APC materials is primarily empirical on designing APC morphology, and few researchers have reported *c*-axis aligned 1D APCs experimentally [37]. A question arises: what are the relevant parameters that determine the APC morphology, dimension, orientation, and density? Can we ever predict the APC morphology in advance without performing a tedious trial and error experimental method? The challenge is to generate optimally designed mixed (1D+ 2D + 3D) APCs morphologies required for the *H*-orientation independent J_c. It is one of the criteria for the application of HTS materials in different devices such as motors and generators at a moderate magnetic field of 3-5 T. This may be achieved by controlling the strain at microscopic scales using multiple APC doping materials to J_c anisotropy.

Little is known regarding the control of the APC/YBCO interface and its effect on pinning efficiency of 1D APCs in nanocomposite thin films. Thus, studying the effect of 1D APC/YBCO interface is important to understand optimal pinning efficiency. Fundamentally, a sharp APC/rare earth (RE=Y, Gd, Sm)$Ba_2Cu_3O_7$ (RE-123) interface at an atomic scale is desired for optimal pinning efficiency, which is in contrast to the often defective 1D APC/RE-123 interfaces reported in nanocomposites using high-resolution transmission electron microscopy (HRTEM) [25, 38, 39]. A qualitative interpretation of the correlation between the pinning efficiency and APC/YBCO interface, and quantitative evaluation of pinning efficiency is critical to engineering (or repairing) an interface for optimal pinning efficiency.

An intriguing difference between the BZO (and BHO) APC/YBCO interface has been revealed in the different doping materials due to a subtle difference of the lattice mismatch of these materials to the YBCO matrix. A defective interface with oxygen deficiencies at the APC/YBCO matrix (semicoherent interface) results in a substantial decrement of pinning efficiency compared to less defective APC/YBCO interface (coherent interface). The immediate question is how can a defective interface be repaired? A diffusion of Calcium (Ca) at the BZO/YBCO interface in the nanocomposite multilayer films may reduce the condition of oxygen deficiency. This may enhance the pinning efficiency of the BZO 1D APCs in a similar way to Calcium doping assisted repairing of the large-angle grain boundaries (GBs) in YBCO film.

Chapter 2 Experiments

2.1 Sample preparation and measurement

As discussed in the introduction, nanodefects which are inherent in nanocomposite films help to improve the vortex pinning properties compared to single crystals. This implies that an effective deposition technique is necessary to grow externally induced nanostructures in HTS thin films with strong pinning centers. The Pulsed Laser Deposition (PLD) technique is an effective means to fabricate the oxide nanocomposite films such as YBCO at moderate oxygen background pressure delivering the controlled stoichiometry. Thus, all the YBCO nanocomposite films in this study were deposited using PLD technique.

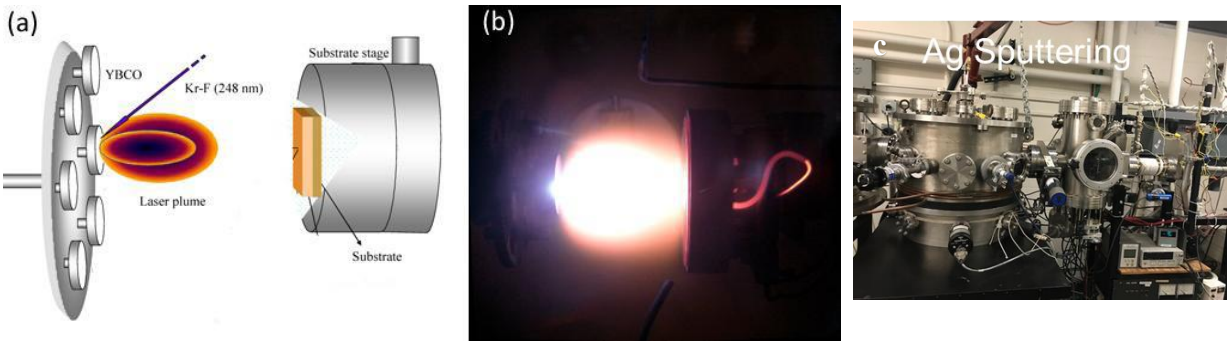

Figure 8: Illustration of Pulsed Laser Deposition of thin film on temperature-controlled substrate. This Figure is adapted from Baca F., KU, 2009 [17], (b) Photograph of a plume produced from a YBCO target, (c) A high vacuum DC sputtering chamber for Ag deposition.

The schematic of the PLD technique is shown in Figure 8a. A plasma plume and a high vacuum DC sputtering system is shown in Figures 8b and 8c respectively. A Lambda Physik LPX 300 KrF excimer laser of wavelength λ =248 nm with an energy density of approximately 2.6 J/cm^2, was

utilized for the deposition of nanocomposite thin films. Laser deposition parameters were laser energy of 400 mJ and a repetition rate of 4-8 Hz.

All the single doped nanocomposite thin films were fabricated using targets with nominal $BaZrO_3$ or $BaHfO_3$ varying concentrations of 2 vol.%, 4 vol.% and 6 vol.%, each plus 98, 96, and 94 vol.% of YBCO respectively. For double doped targets, additional 3 vol.% of Y_2O_3 was added on each respective volume of BZO or BHO to make mixed targets and volume of YBCO was then varied accordingly. Commercial powders of YBCO (Nexans), Y_2O_3, $BaZrO_3$, and $BaHfO_3$ (SCI Eng. Mtls.) were dried in a heating furnace for about 10 hours at 450 ˚C. The dried powders were measured and mixed with an agate mortar and pestle to comprise a specific composition as stated earlier. The mixture was pressed utilizing a 25 mm and 6 mm die at a pressure of 1000 psi. All the targets were then sintered at 850 ˚C for 60 hours and 950 ˚C for 156 hours.

Nanocomposite thin films were deposited on (100) $SrTiO_3$ (STO) single crystal substrates, having dimensions of 5.0 mm x 5.0 mm x 5.0 mm. These substrates were cleaned via an ultrasonic cleaner for approximately five minutes with acetone, followed by five minutes with isopropyl alcohol. The substrates were mounted to a coated heater block with colloidal silver paint. The targets were rotated to ensure uniform ablation over the target surface. All depositions of films were done in a high vacuum system. The substrate to target distance was about 4.5 cm. These depositions were conducted at heater block temperatures of 810-825 ˚C for 8-10 minutes. After deposition, the films were annealed for about 30 minutes dwell time at 500 ˚C and one atmosphere oxygen environment. Film thicknesses were determined by etching corners of the films with the

substrate and the thickness of the step-edge was measured using a KL-16 Tincor profilometer. All the films had an average thickness of 140 nm.

Depositions of 130 nm silver contact electrodes were conducted utilizing a high vacuum DC sputtering system. It is carried out at the argon gas background pressure of 30 mTorr for about 30 minutes at the deposition rate of approximately 0.07 nm/second. Figure 8c shows the high vacuum DC sputtering system for silver electrodes deposition. For an electrical transport measurement, samples were patterned using standard photolithography to obtain microbridges of width ~20 μm and length ~500 μm. The films were first spin-coated with the photoresist on the surface with a thickness of approximately 1.3 μm for 4000 revolutions per minute for 60 seconds. Nanocomposite thin films were exposed at 500 W UV for 70 s with Karl-Suss Mask Aligner. Then films were developed in 1:3 solution of Microposit 351 developer and deionized water for the optimized time of approximately 60 seconds and etched for approximately 90 seconds with

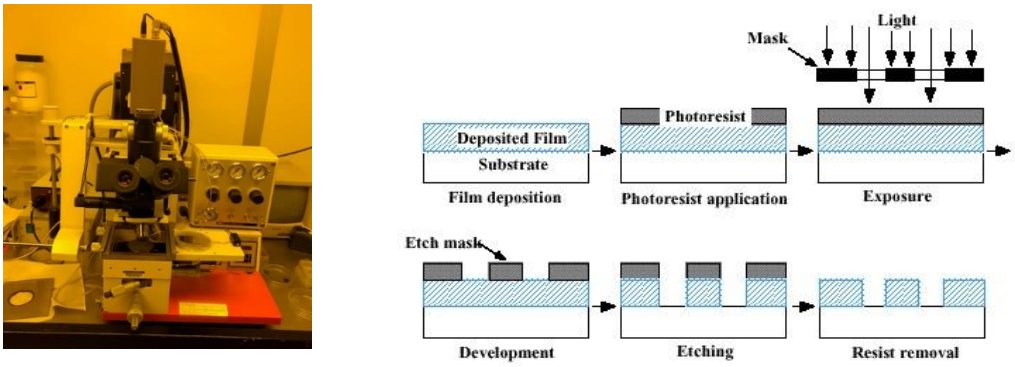

Figure 9: Left: Ultra Violet light source equipment. Right: Illustration of the standard photolithography in HTS thin films.

0.05% HNO_3. The remaining photoresist was removed with acetone followed by a rinse off using isopropyl alcohol (IPA) solution. The electrical connection to the microbridges was completed via

indium attachment of platinum wires of 25 μm in diameter before taking T_c and resistivity measurements of these films. Ultra Violet (UV) light source equipment and the general procedure of the standard photolithography process in a clean room environment is shown in Figure 9.

Current-voltage (I-V) characteristics were measured using a Keithley 2430 1 KW pulsed current source meter and HP 34420A nanovoltmeter. Critical current I_c was measured using standard 1 μV/cm criteria. Critical current density J_c was then calculated dividing I_c by the cross-sectional area of microbridges. LabView was used to send the input current pulse of increasing amplitude and synchronizing the detection of the voltage across the nanocomposite films. The short pulse width of 50 ms and the long-time interval between pulses in the range of 3-4 seconds were selected to minimize the sample heating issues.

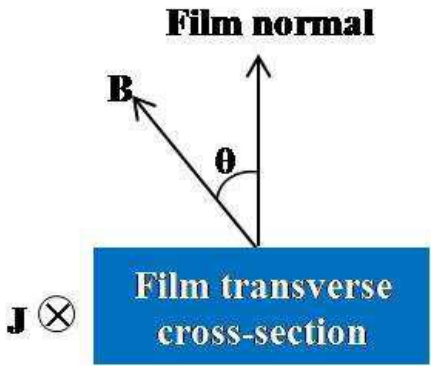

Figure 10: Schematic diagram of the J_c (H, θ) measurement of the thin film *ab*-plane. This Figure is adapted from Baca F., KU, 2009 [17].

A Quantum Design Evercool II Physical Property Measurement System (PPMS) was used to measure the electrical transport J_c (T, H, θ) as function of temperature T, magnetic field H (up to 9 T) and the orientation angle θ between H and the c-axis while H was maintained in the plane

perpendicular to the current. Figure 10 illustrates the angular dependence measurement of the electrical transport properties of the nanocomposite thin film.

2.2 APC nanostructures characterisation

APCs nanostructures of the nanocomposite thin films in this work were studied using high resolution images of crystal structure utilizing transmission electron microscopy (TEM) tool. This work is done with the collaboration of the Air Force Research laboratory (AFRL) and the School of Material Engineering at Purdue University. Cross-sections of the films were prepared using a FEI Nova 600 NanoLab, DB235 focused ion beam systems, and FEI TALOS 200X in respective laboratories. The samples were thinned down to ~60 μm and dimpled to ~30 μm and then ion milled before taking images.

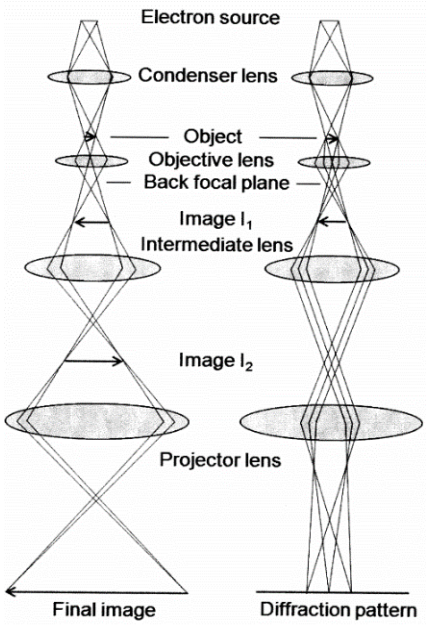

Figure 11: Ray diagrams for the imaging and diffraction mode in a transmission electron microscope. This Figure is adapted from McLaren A., CUP, 1991 [40].

The nanostructures of the films were studied using a Philips CM200 and FEI Titan TEM operating at 200 kV and 300 kV, respectively [Baca F., dissertation, 2009 and Sebastian M.A., dissertation, 2017].

In TEM, the electrons from the electron gun are accelerated by a high voltage and focused onto a thin specimen by magnetic lenses. The transmitted electrons are then focused. The high-resolution TEM (HR-TEM) images are obtained using the phase contrast arising from the phase differences after the electrons get scattered from the sample. The objective aperture is placed in the back focal plane to increase the scattered from the sample and to increase the diffraction contrast. Along with TEM, other techniques such as high-angle annular dark field (HAADF) scanning transmission electron microscope (STEM) and energy dispersive X-ray spectroscopy (EDS) is also used for microstructural characterization. The STEM imaging under HAADF condition is also called Z-contrast where the image contrast is roughly proportional to Z^2 where Z is the atomic number of the element. Such composition-based imaging in STEM is ideal for microstructural analysis of different phases.

2.3 Crystallinity of the films

A Bruker D8 X-ray diffraction (XRD) system was used to study the *c*-axis growth of epitaxial films and crystalline structure of the nanocomposite films. Epitaxy is the growth of the film that follows the same crystalline structure of the substrate. Even though the lattice mismatch between the $SrTiO_3$ (STO) substrate and the YBCO film is about 1.5%, it still forms the crystal structure of the thin films. All the nanocomposite films in this study were grown *c*-axis along the thickness of the films which

was confirmed by XRD analysis. Diffraction occurs when the incident X-rays upon a sample are scattered by the crystal plane of the sample and undergo constructive interference in accordance to Bragg's law ($2d\sin\theta = n\lambda$).

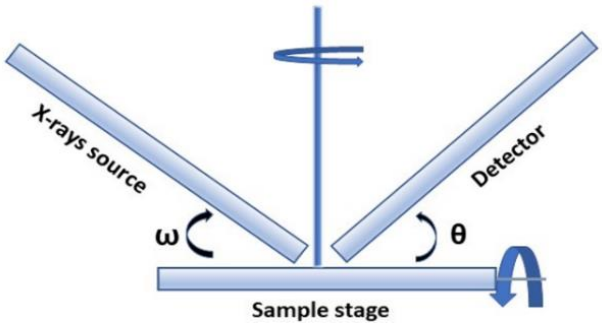

Figure 12: Illustration of the schematic of XRD system.

The Copper K_α line of wavelength (λ) of 1.54 Å is utilized in this study where *d* represents the lattice spacing of the crystal plane. A diffraction pattern is observed through the intensity of scattered waves as a function of scattering angle (θ). Figure 12 illustrates the schematic of the XRD system. The XRD system is composed of the X-rays source, detector, and a rotating sample stage. The crystallinity orientation of the films is determined by a ω -2θ scan. All the intensity peaks of the films are normalized to YBCO (005) which excludes the overlap of STO (200) peak. Through qualitative analysis of the phase identification via the peaks, evidence of the epitaxial growth of the nanocomposite films is confirmed. Quantitatively, *c*-axis lattice constants of the nanocomposite films are calculated. The full-width-at-half-maximum (FWHM) of the YBCO (005) peak is measured through an omega (ω)- theta (θ) scan. This is achieved by setting the x-ray source to ω, which corresponds to a d-spacing of the YBCO (005) peak and allowing the detector to move at different θ angles.

Chapter 3 Microscopic Dynamics and Adaptation of APCs Nanostructures for Isotropic Pinning

Many HTS applications require that the critical current density be independent of a magnetic field of few Teslas through strong artificial pinning centers (APCs) [34, 41, 42]. Exciting progress has been made via strain-mediated self-assembled APCs nanostructure phases in $YBa_2Cu_3O_{7-x}$ (YBCO) thin films and conductors [32, 33, 43-45]. Among others, *c*-axis aligned one-dimensional APCs (1D APCs) have exhibited strong correlated pinning to magnetic vortices at magnetic field *H*//*c*-axis, resolving the issue of weak pinning along the *c*-axis originated from the layered structure of the YBCO. Several materials have been reported to form *c*-axis aligned 1D APCs in APC/YBCO nanocomposite films including $BaZrO_3$ (BZO), $BaSnO_3$ (BSO), and $BaHfO_3$ (BHO) [46-48]. However, the perfectly aligned or small-angle splayed (~10^o for BZO and ~13^o for BHO at their optimal growth temperature of 810 ^{o}C - 825 ^{o}C) 1D APCs may not benefit vortex pinning when *H* is oriented considerably away from the *c*-axis [18, 24]. To achieve a more isotropic J_c, several APC structural control approaches have been explored including double-doping. A combination of 1D APCs (BZO or BSO or BHO, Ba_2 (Y/Gd) (Nb/Ta) O_6) and 0 D APCs (Y_2O_3, or $(Y/Gd)_2O_3$) [31, 35, 41, 49, 50], and length and splay control of 1D APCs through alternate/segmented layer deposition [51]. Earlier studies have reported that these approaches have reduced the J_c anisotropy compared to single doped YBCO thin films either due to the presence of shorter and segmented 1D APCs or additional 3D APCs [34, 41, 52]. This study utilizes an elastic strain model proposed by Shi et.al [53] to evaluate the rigidity of the *c*-axis aligned 1D APCs in a

$YBa_2Cu_3O_{7-x}$ matrix of nanocomposite films. This model illustrates the alignment of the BZO and BHO 1D APCs, based on their rigidity. Although having comparable diameters of ~5-7 nm [53], the elastic properties (rigidity and flexibility) of these materials can be tuned differently by the addition of secondary APCs of Y_2O_3 (3D APCs), leading to a different pinning landscape and J_c (H, θ) behaviors especially reduced J_c anisotropy. The concentration effect of less rigid materials in strong and isotropic pinning will be discussed later in this chapter. Specifically, we will report the threshold volume of the doping materials for mixed APCs morphology. In addition, above the threshold limit of BHO doping, the switching effect of *c*-axis alignment to *ab*-plane alignment of BHO 1D APCs has been explained due to the presence of the secondary doping Y_2O_3.

3.1 Strain mediated self-assembled APCs in APC/RE-123 nanocomposite thin films

Epitaxial growth of the nanocomposite films using Pulsed Laser Deposition (PLD) follows the layer by layer growth mode. At the initial growth stage of the self-assembled APC materials, the phase segregation of these materials with rare earth (RE=Y, Gd, Sm) $Ba_2Cu_3O_7$ (RE-123) matrix initiates the coherent or semicoherent APC/RE-123 interface, film/substrate interface, and APC/substrate interface. Figure 13 represents a schematic of such interfaces. The lattice mismatch between each interface create strain at the lattice and is complex due to elastic properties of APC materials, RE-123 films and substrate. The contribution of the substrate elastic property can be neglected due to the large thickness of the substrate. It is assumed that only RE-123 and APCs accommodate to the strain field generation. The resultant strain field serves as the driving force in

the strain-mediated self-assembly of the APCs in the APC/RE-123 nanocomposites. The strain extends away from an interface into the epitaxial APC/RE-123 nanocomposite films due to the ceramic nature of the doping materials and the film itself. This suggests that the strain field may be considerably non-uniform in the APC/RE-123 nanocomposite films.

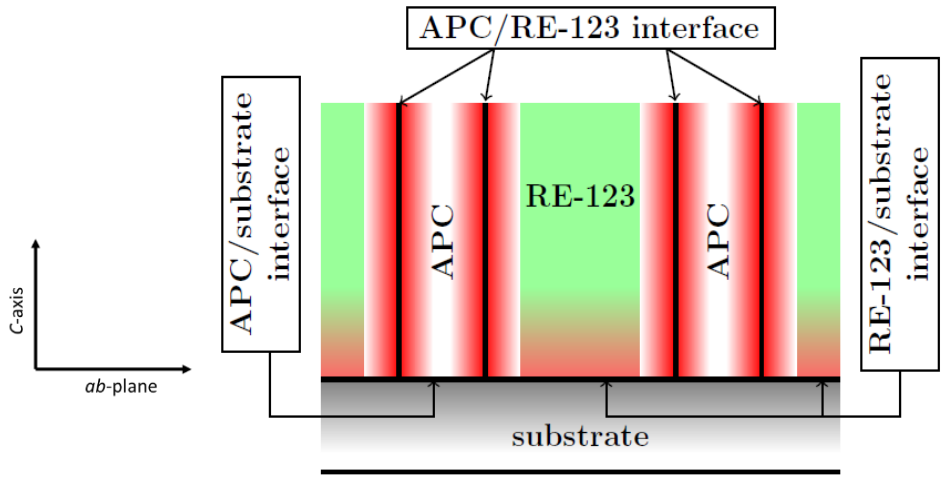

Figure 13: Self-organization of 1D APCs driven by the combined strains originated from the strained interfaces. Three strained interfaces of 1D-APC/RE-123 matrix, APC/substrate and RE-123/substrate are illustrated schematically. The index represents the *c*-axis and *ab*-plane direction. This Figure is adapted from Wu et.al, SuST, 2017 [54].

It is thus important to understand and illustrate the effect of the strain and elastic properties of the materials on nanostructure alignment, morphology, and dimensions to form the mixed morphology of APCs. An elastic strain model proposed and published by Shi et. al [53] explains the effect of the lattice mismatch along *ab*-plane and *c*-axis at the APC/RE-123 interface and elastic properties of APC and RE-123 nanocomposite (c_{ij}) on the APC landscape. Figure 14 shows the lattice mismatch $|f_1/f_3|$ vs. elastic constant phase diagram for several APC materials in a YBCO matrix. The results presented in Figure 14 is done by Shi et. al [53] and is reproduced from Gautam

et. al [13]. The f_1 and f_3 represent pub lattice mismatch between the YBCO and APC dopant along [100] and [001] directions respectively. C_{11} and C_{12} are the elastic constants of the dopants. It should be noted that BZO and BHO have subtle differences both in their lattice mismatches with the YBCO matrix and in their elastic properties. The lattice mismatch of the former is 7.1% compared to 6.7 % on the latter. This section shows the alignment of the BZO and BHO 1D APCs, although having comparable diameters of ~5-7 nm [53], can be tuned differently by the addition of Y_2O_3 3D APCs, leading to a different pinning landscape of APCs and hence different $J_c(H, \theta)$ behaviors.

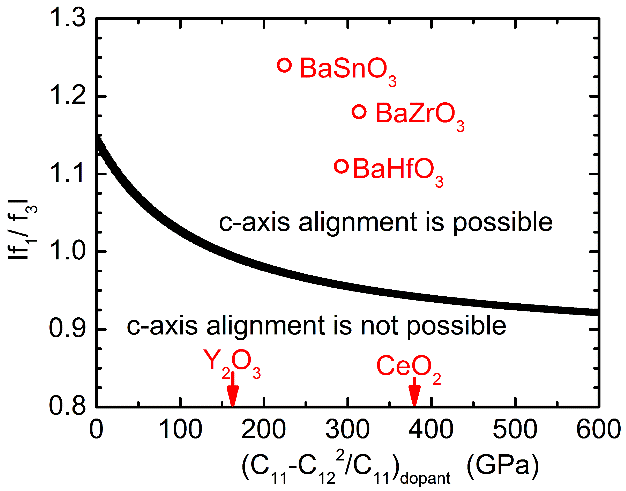

Figure 14: Shi et. al [53] calculated (f_1/f_3) vs. $(C_{11}-C_{12}^2/C_{11})_{dopant}$ phase boundary (solid line) above which the dopant materials energetically prefer to form c-axis aligned 1D-APCs in YBCO thin films. f_1 and f_3 are the lattice mismatch of film and dopants along *a* and *c*-axes respectively. C_{11} and C_{12} are the elastic constants of the dopant. The points for Y_2O_3 and CeO_2 are below the limit of the y-axis. This Figure is adapted from Gautam et.al, AIP Advances, 20117 [13].

The lattice mismatch between APC and YBCO along with the elastic properties of both are found to affect the morphology of the APCs formed in the APC/YBCO nanocomposite films. By

minimizing the elastic energy of the APC/YBCO nanocomposite film, a lattice mismatch versus elastic constant phase boundary has been obtained between materials that can form *c*-axis aligned 1D APCs and those that cannot [53]. Quantitatively, the rigidity of the *c*-axis aligned 1D APCs should be proportional to their distance from the phase boundary.

As illustrated in Figure 14, doping materials such as BZO and BHO (above the solid line) energetically prefer to form the *c*-axis aligned 1D APCs in YBCO. While other materials such as Y_2O_3 and CeO_2 (below the phase boundary) prefer to form other than *c*-axis aligned 1D APCs. The solid line represents the coexistence of the different APC morphology across the phase boundary. Materials closer to the phase boundary are more flexible to the formation of the mixed APCs. BHO is closer to the phase boundary than of BZO (or BSO) and so the BHO 1D APCs are less rigid than that of the BZO (and BSO) counterparts. This means that the formation of the *c*-axis aligned BHO 1D APCs could be more interrupted by the presence of the secondary doping material of Y_2O_3 that forms 3D APCs [13]. Hypothetically, shorter and misaligned BHO 1D APCs in the BHO DD films could lead to a more mixed pinning landscape as compared to the BZO DD case. A study of 3 vol.% Y_2O_3 + 2-6 vol.% $BaHfO_3$ double doped $YBa_2Cu_3O_{7-x}$ (BHO DD) epitaxial thin films is further carried out to explore the morphology adaption of the *c*-axis aligned BHO 1D APCs to the secondary Y_2O_3 nanoparticles (3D APCs). With the support of the elastic energy model [53] and experiments, the microscopic adaptation mechanism of the APCs may illustrate the effect of the strain on dimension, morphology, and orientation of APCs in the RE-123 nanocomposite films. These results are certainly the key to the controllable generation of mixed APC morphology for strong and isotropic pinning of vortices. This may result in reduced

J_c anisotropy for the entire angular range from H//c-axis ($\theta=0^o$) to H//ab-plane ($\theta=90^o$) of the applied magnetic field H to obtain the desired APC landscape.

3.2 Crystallinity of the double doped nanocomposite thin films

After completion of nanocomposite thin film deposition, it is essential to ensure that the films are well *c*-axis aligned and epitaxial. *C*-axis alignment and qualitative interpretation of epitaxial growth of the nanocomposite thin films are confirmed utilizing θ-2θ scan from X-ray diffraction technique. All the nanocomposite films of 2-6 vol.% BHO DD and 2-6 vol.% BZO DD in this study are well *c*-axis aligned with growth parallel to the thickness of the film. Figure 15 compares the X-ray diffraction (XRD) θ-2θ spectra for the 2 vol.%-6 vol.% BHO DD and 2 vol.%-6 vol.% BZO DD nanocomposite thin films.

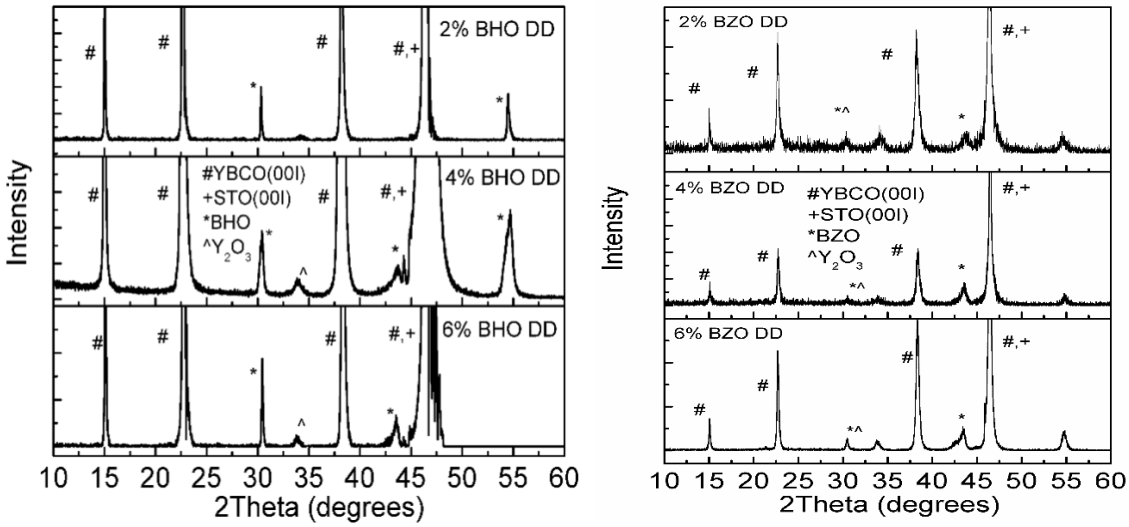

Figure 15: XRD θ-2θ spectra for the 2%-6 vol.% BHO DD nanocomposite films (left) and 2- 6 vol.% % BZO DD nanocomposite films (right) on STO substrates.

All samples show high quality crystallinity with *c*-axis orientation as illustrated in the appearance of the YBCO (00l) peaks. The minor peaks at around 2θ ~30° and ~43° are indexed as the BHO or BZO, and the minor peak at around 2θ ~34° is indexed to the Y_2O_3 phases. The *c*-axis lattice constants of YBCO films are calculated from these spectra and the results are listed in Table I. Highly strained and coherent APC/YBCO interface is maintained at low BHO doping of 2 vol.% in these samples as expected, which is confirmed by an elongated *c*-axis of 11.77 Å. With a further increase of BHO doping, the *c*-axis lattice is reduced systematically towards 11.68 Å for an undoped YBCO thin film. The BHO single doped YBCO thin film [55], in which *c*-axis lattice constant increases from ~11.69 Å to ~11.72 Å when BHO concentration increases from 2 mol% to 6 mol% (corresponding to ~1 to 3 vol.%), in contrast to BHO DD nanocomposite films.

Samples	*c*-axis lattice constant (Å)	$T_{c,onset}$ (K)	FWHM of the YBCO (005) rocking curve	J_c anisotropy		
				77 K	65 K	
				1T	5 T	9 T
2% BHO DD	11.77	87.08	0.35	0.41	0.47	0.18
4% BHO DD	11.75	86.60	0.76	1.04	0.42	0.56
6% BHO DD	11.73	85.80	0.57	4.21	1.11	1.73
2% BZO DD	11.75	85.71	0.73	1.60	1.33	0.99
4% BZO DD	11.72	87.69	0.49	0.79	0.43	0.56
6% BZO DD	11.74	87.80	0.54	2.41	0.60	0.92

Table 1: *C*-axis lattice constant, critical temperature (T_c), FWHM of the YBCO (005) rocking curve, and J_c anisotropy of 2, 4, and 6% BHO DD and BZO DD nanocomposite thin films.

On the other hand, for BZO DD nanocomposite films, the *c*-lattice constant is first decreased and then increased as the doping concentration is increased from 2 vol.% to 4 vol.% and then 6 vol.%. This indicates that the compressive strain might be decreased as the BZO doping concentration is increased from 4 vol.% to 6 vol.%. However, increasing trend of T_c in BZO DD films contrasts with BHO DD film in which T_c is decreased with increasing doping concentration indicates that the effect of strain field overlap is decreased in the former compared to the latter. Moreover, the comparably higher T_c in 6 vol.% BZO DD compared to 4 vol.% BZO DD film further indicates that with increasing BZO concentration doesn't add strain to the YBCO lattice. However, these T_c values are considerably higher than that of single BZO doped YBCO nanocomposite film (~86 K for 4 vol.% and 84 K for 6 vol%) [30].

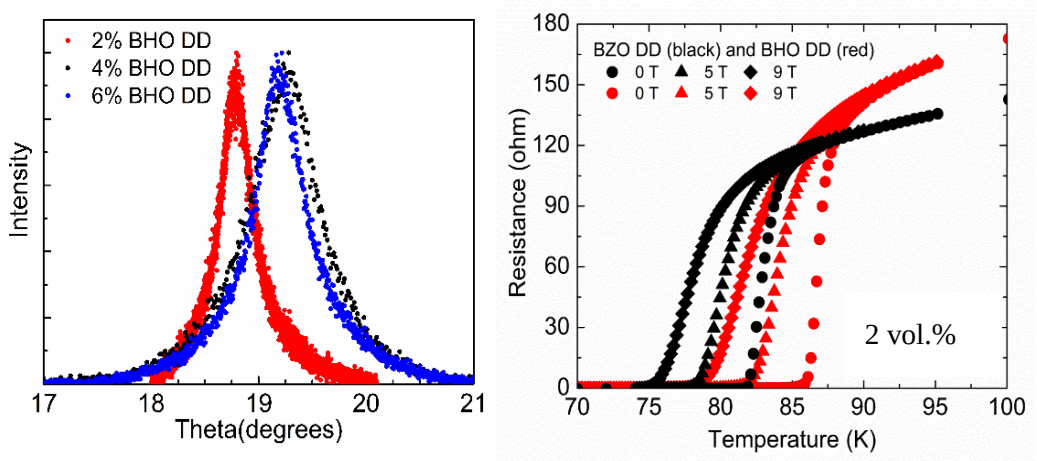

Figure 16: Left: rocking curve of YBCO (005) peak of the 2-6 vol.% BHO DD nanocomposite films. Color codes 2 vol.% (red), 4 vol.% (black) and 6 vol.% (blue). Right: resistance vs. temperature curves for 2 vol.% BZO DD (black) and BHO DD (red) thin films measures at 0 T (circle), 5 T (triangle), and 9 T (diamond).

Figure 16 left depicts the X-ray diffraction YBCO (005) rocking curves of 2 vol.%-6 vol.% BHO DD nanocomposite thin films. The rocking curves are the ω-θ scan of the XRD spectra that

provide qualitative and quantitative information of the crystalline size and strain in the crystal plane through peak shift and/or peak broadening. A shift of the peak position towards the right (larger θ) is an indication of the decrease of the *c*-axis lattice constant with BHO concentration, and an indication of uniform strain in the film lattice. Within the crystalline structure, uniform strain causes the unit cells to contract or expand isotropically [Sebastian M.A., dissertation, 2017]. An initial increase of the YBCO (005) full width at half maximum (FWHM) with increasing BHO concentration in the lower BHO doping range of 2-4 vol.% (0.35 at 2 vol.% and 0.76 at 4 vol.%) is an indication of an *ab*-plane disturbance and increase of lattice strain. It further indicates that a coherent or a semi-coherent BHO/YBCO interface is maintained in this doping range. At the higher BHO concentration of 6 vol.%, the reversed trend of a reduced YBCO (005) FWHM of 0.57 could be due to the interfacial defects and dislocations at the BHO/YBCO matrix. This is consistent with the reduced *c*-axis elongation in 6 vol% BZO DD thin film as compared to that of the 4 vol.% BHO DD film (Table 1). These results are consistent with the less elongated *c*-axis and increased FWHW of the (005) YBCO peak for similar doping of films as reported in earlier studies [36, 38, 55]. The published results are based on the argument of the formation of defects such as dislocations, especially at the APC/YBCO interfaces, leads to relaxation of the interfacial strain results in reduced *c*-axis lattice. Qualitatively, a peak broadening implies that the non-uniform strain at which a systematic shift of atoms from their ideal positions occurs resulting in point defects, plastic deformation or poor crystallinity. Additionally, T_c decreases monotonically (Table I) with the BHO doping from ~90 K for the undoped YBCO films to 87.1 K, 86.6 K, and 85.8 K for 2, 4, and 6% BHO DD nanocomposite thin films respectively. In comparison with the

BHO SD samples [55, 56] in which the T_c values also decrease monotonically with the BHO doping, from 88.1 K to 87.7 K when BHO concentration increases from 2 mol% to 6 mol% (corresponding to ~1 to 3 vol.%), a comparable but slightly higher T_c degradation occurs in the BHO DD nanocomposite films. Interestingly, increasing trend FWHM of YBCO (005) is not followed in BZO DD thin film (Table 1). The highly strained lattice at 2 vol.% BZO DD film is relaxed with increased BZO concentration. Substantially decreased FWHM of YBCO (005) peak at 4 vol.% and 6 vol.% BZO DD film indicates strain is released through the significantly defective BZO/YBCO interface with increasing BZO concentration. The smaller T_c and *c*-axis lattice constant variations with increasing BZO doping in the 4 vol.% and 6 vol.% BZO DD thin films are not consistent with the decrement of T_c and *c*-axis lattice constant at BZO single doped YBCO nanocomposite thin films [36, 57].

Considering a similar concentration of different doping materials, a higher FWHM of 6 vol.% BHO DD film indicates a higher disturbance of YBCO lattice along *ab*-plane (such as *ab*-plane buckling) in contrast to BZO DD film. While at moderate doping of 4 vol.% the reversed effect is observed in which latter has a less disturbance of YBCO lattice at *ab*-plane. Most interestingly, a considerably larger full-width-at a half maximum (FWHM) of the 2 vol.% BZO DD (~0.73), than that of the 2 vol.% BHO DD film (0.35) indicates the YBCO lattice is considerably more disturbed in the BZO DD nanocomposite film. This may explain its more severe T_c degradation to 85.71 K as compared to 87.08 K of the BHO DD film. Figure 16 right shows the resistance vs. temperature (R-T) curves of 2 vol.% BZO and BHO DD films at different *H* fields

of 0, 5.0 T, and 9.0 T. It shows the transition temperature (T_c) with increasing field is different for both films. With the increasing field of 5.0 and 9.0 T, the higher slope of R-T curves for BHO DD film is an indication of higher T_c values and may hold better superconducting properties than that of BZO DD nanocomposite thin films. Further, the slow drop of T_c with the fields is an indication of strong pinning potential (U_p) in the former against the high magnetic field. As $J_c \sim U_p/k_BT$, k_B is the Boltzmann constant and T is the temperature, with strong pinning potential, it is expected to have a higher J_c (H) value for BHO DD film at low temperature.

3.3 Nanostructures morphology

Figure 17 illustrates the cross-sectional transmission electron microscopy (TEM) images of the 2 and 6 vol.% BZO DD and 2 and 6 vol.% BHO DD nanocomposite thin films. In 2 vol.% BZO and BHO thin films (Figures 17a-b), massive large nanoparticles of several nanometers (5-15 nm) in diameter can be clearly visible. However, these images are not so clear to see the many extended BZO and BHO 1D APCs aligned in the *c*-axis of YBCO films. Some of them appear as 1D APCs that indicates the mixed APCs landscape in 2 vol.% BHO DD films, which is in contrast to the typically only *c*-axis aligned BHO 1D APCs in the BHO SD films [27]. Low resolution TEM images can also be found for mixed APCs [58] in BHO DD nanocomposite film. This confirms the mixed APC morphologies in the BZO DD samples reported earlier by Maiorov *et al* and a similar APC landscape in the BHO DD samples [34, 41]. In the 6 vol.% BZO DD films (Figure 17c) the *c*-axis aligned BZO 1D APCs (dashed lines), plus many shorter 1D APCs not

going through the film thickness are clearly visible. Some of the BZO APCs are splayed with respect to the *c*-axis, which may evolve to large splay angles at a larger film thickness.

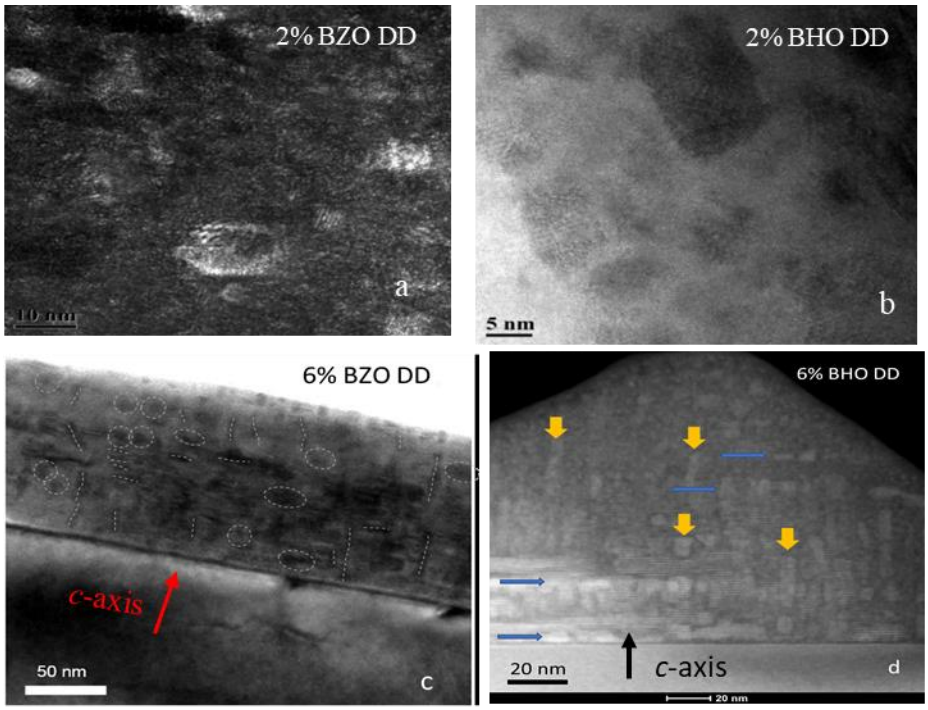

Figure 17: TEM images of the (a)-(c) 2 and 6 vol.% BZO+3 vol.% Y_2O_3 (BZO DD), and (b)-(d) 2 and 6 vol.% BHO+3 vol.% Y_2O_3 (BHO DD) doped YBCO nanocomposite thin film deposited on 100 STO substrate.

This is quite different from the single doped (SD) case in which the BZO 1D APCs diameter remains almost a constant and the areal density of the *c*-axis aligned BZO 1D APCs (mostly through the film thickness) increases linearly with the BZO doping concentration from 2 vol.% to 6.0 vol.%. conditions [34]. In the BZO DD case, the length of the BZO 1D APCs varies over a wide range from ~20 nm to 140 nm and the proportion of the BZO 1D APCs of different lengths depends on the BZO doping levels. In addition, *ab*-plane aligned 2D APCs and some 3D

APCs (marked with circles) are seen in 6 vol.% BZO DD films. The 2D APCs are of 5-10 nm in thickness and about 20 nm in lateral diameters. Similarly, at 6 vol.% BHO DD nanocomposite film higher concentration and more continuous 2D APCs in the *ab*-plane are clearly seen (Figure 17d) including the shorter BHO 1D APCs along *c*-axis together with 3D APCs. The orientation of the many *c*-axis aligned 1D APCs are switched to *ab*-plane alignment at 6 vol.% BHO DD films compared to splayed *c*-axis aligned 1D APCs in 2 vol.% BHO DD film. Based on the TEM observation, it can be concluded that in BZO and BHO DD films, mixed morphologies of 1D, 2D, and 3D APCs are formed.

3.4 Electrical transport characteristics of BZO or BHO double doped YBCO nanocomposite thin films

3.4.1 Critical current density $J_c(H, T, \theta)$

Figure 18 compares the $J_c(H)$ curves of the 2 vol.% BZO or BHO + 3 vol.% Y_2O_3 (BZO DD and BHO DD nanocomposite thin films at 77 K and 65 K, respectively, at different orientations of the applied magnetic field. At *H*//c-axis (Figure 18a), the *c*-axis aligned 1D APCs are anticipated to provide strong correlated pinning at up to the so-called matching fields H_{max}. The H_{max} is determined by the areal density of the 1D APCs. The enhanced correlated pinning is typically is expressed quantitatively in the low α values calculated from the relation $J_c(H) \sim H^{-\alpha}$ [14, 35] as compared to an alpha value (α) ~0.5 for the undoped YBCO [26]. At 77 K, the α value is ~0.49 for BZO DD and ~0.27 for the BHO DD film, indicating more enhanced pinning in the latter.

The α value of the BHO DD nanocomposite film is ~0.27, which is considerably lower than that (~0.32) of the BHO SD film [24]. It indicates the improved pinning in the former compared to the latter ones. One possible explanation of the negligible lower pinning efficiency of the BZO 1D APCs may be the lower T_c too close to 77 K at which $J_c(H)$ is measured.

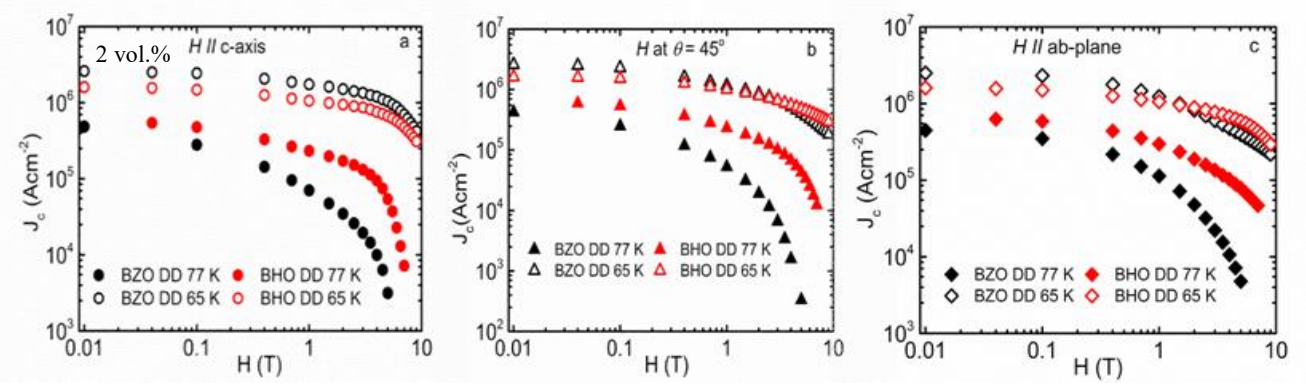

Figure 18: J_c vs. H curves measured on 2 vol.% BZO DD (black) and BHO DD (red) samples at (a) θ =0° (*H*//c-axis); (b) θ = 45°; and (c) θ = 90° (*H*//*ab*-plane) at 77 K (solid) and 65 K (open), respectively.

This same T_c effect may explain the lower $J_c(H)$ observed on the BZO DD film at θ =45° (Figure 18b) and θ=90° (Figure 18c) at 77 K. At 77 K and 1.0 T, J_c (*H*//*c*-axis) for the BHO DD (~0.24 MA/cm^2) is lower than ~ 7.0 mol % BZO + 7.0 mol%Y_2O_3 DD sample (0.45 MA/cm^2) [59] and 3 wt.% BZO+2 wt.% Y_2O_3 DD sample (0.4 MA/cm^2) [52]. Although the J_c value in BHO DD sample is not superior to BZO DD, the lower α value for BHO DD (0.27) compared to BZO DD (0.31) [52] indicates the slightly stronger vortex pinning in the former. In addition, the higher H_{max} of ~3.5 T for BHO DD film as compared to BZO DD film's 3.0 T [52] indicates a higher concentration of strong APCs in the former.

At 65 K, the T_c effect becomes insignificant at which comparison between $J_c(H)$ curves are more significant. When H is parallel to c-axis, although the $J_c(H)$ for the BZO DD film is higher than that of BHO DD film (Figure 18a), comparable α values of 0.17 and 0.16 respectively for these films are calculated. This suggests the most probable explanation for the lower $J_c(H)$ in the BHO DD sample is the greater disturbance of the BHO 1D APC alignment in the c-axis. The overall higher $J_c(H)$ in BZO DD films could be due to effectively longer length of 1D APCs that provide more effective pinning at $H//c$-axis at 65 K. The poorer c-axis alignment of BHO 1D APCs indeed shows a higher pinning efficiency at $H \geq 2.0$ T at 65 K at both $\theta=45^o$ (Figure 18b) and $\theta=90^o$ (Figure 18c) which is observed as a crossover of the $J_c(H)$ curves for these samples at ~2.0 T. The trends in the $\theta=45^o$ and $\theta=90^o$ cases indicate the BHO APCs enhance the pinning at wider angles in between the c-axis and ab-plane which is probably not associated to the small angle splay of the BHO 1DAPCs around the c-axis. Rather, it is argued that the presence of the secondary Y_2O_3 3D APCs affects the kinetic diffusion process during the BHO 1D APCs formation along the c-axis, resulting in many shorter, misaligned segments of the BHO 1D APCs. In one of the earlier studies on BZO single and doubled doped YBCO films, it was found that the BZO 1D APC length can be reduced by a factor of 2-3 from the former to the latter case at the same growth conditions [34]. In addition, the shorter 1D APCs tend to misalign away from the c-axis. A similar effect of misalignment of BHO 1D APCs is expected to happen in the BHO DD thin films. Considering the lower rigidity of the BHO 1D APCs than that of the BZO 1D APCs as shown in Figure 14, the level of the misalignment could be more significant in this case.

The benefits from the short and misaligned 1D APCs away from *c*-axis can be explained by a few indicators. First, it may result in reduced strain on the YBCO lattice, which seems consistent with the 1.3 K higher T_c observed on BHO DD nanocomposite film compared to that of BZO DD film. This leads to significantly higher J_c (*H*) in the former at higher temperatures, such as 77 K as shown in Figure 18. Second, it provides isotropic pinning at other *H* orientations away from *H*//c-axis. Indeed, at 65 K, significantly lower α values of 0.25 (θ = 45°) and 0.19 (θ = 90°) are calculated for the BHO DD film compared to that of 0.36 and 0.39 for the BZO DD counterpart. This results in smaller anisotropy of the α value at different *H* orientations.

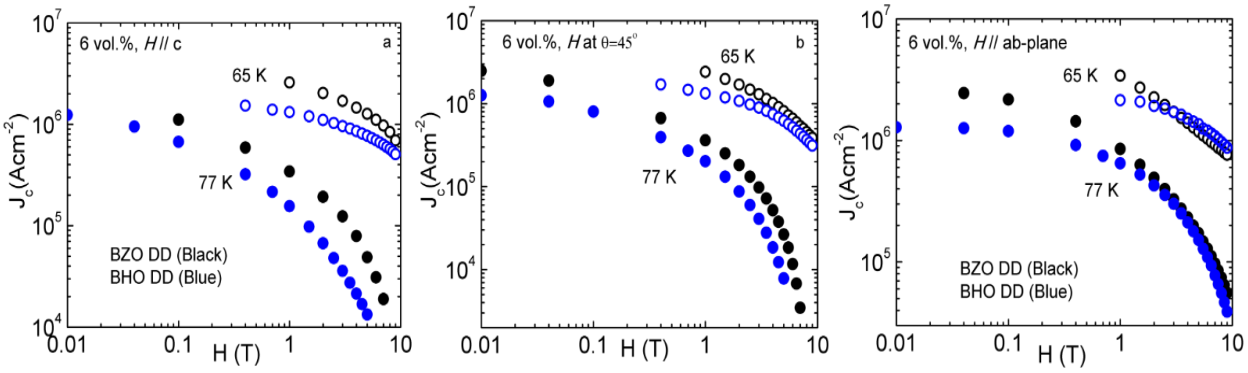

Figure 19: J_c vs. *H* curves measured on 3 vol.% Y_2O_3+6 vol.% BZO or BHO doped YBCO (BZO or BHO DD) nanocomposite films at (a) *H*//c-axis, (b) θ = 45°; and (c) *H*//*ab*-plane nanocomposite films at 77 K (solid) and 65 K (open) respectively.

In parallel, the J_c (*H*) curves of the 6 vol.% BZO DD (black) and BHO DD (blue) measured at the same temperature of 77 K (solid) and 65 K (open) are compared in Figure 19. With the increasing BZO and BHO concentration to 6 vol.%, the overall J_c (*H*) at *H*//*c*-axis is higher for BZO DD nanocomposite film for the entire field up to 9.0 T, and at both temperatures 77 K and 65 K. Interestingly, the T_c values for 6 vol.% BHO DD film reduces to 85.8 K in contrast to T_c ~

87.8 K for 6 vol.% BZO DD films (Table 1) probably influence the J_c (H) values at 77 K instead at 65 K. Despite the similar PLD thin film deposition process is used to these films, 3 vol.% Y_2O_3 3 D APCs may influence differently to the pinning landscape of different doping materials. The similar trend of increasing T_c for 6 vol.% BZO DD film is also observed in 6 vol.% BZO single doped YBCO film on the vicinal substrate [17]. This could be due to the reduction of strain field overlap due to the presence of 3D APCs. Since J_c (H) is proportional to the effective length of APCs, the higher J_c (H) at H//c-axis at 65 K for 6 vol.% BZO DD possibly due to longer effective *c*-axis aligned BZO 1D APCs. The similar trend with comparable J_c (H) for the magnetic field (H) at θ=45^o for both 6 vol.% BZO and BHO DD nanocomposite films observed at 65 K, where T_c effect is negligible, implies comparable pinning strength of 1D APCs (Figure 19b).

At 65 K, J_c (H) at H//*ab*-plane overcomes for 6 vol.% BHO DD film at the higher field (>2.0 T) same as the 2 vol.% BHO DD film. The slow decrease of J_c at a high field when H//*ab*-plane or about 1.7 times higher J_c (H) at H//*ab*-plane in average for the entire field up to 9.0 T compared to J_c (H) at H//c-axis at 65 K for 6 vol.% BHO DD indicates the strong pinning possibly due to *ab*-aligned BHO 1D APCs. However, the reverse results are observed in 6 vol.% BZO DD film in which higher J_c (H) along *c*-axis compared to *ab*-plane. The higher J_c (H) at H//*ab*-plane may be due to strong intrinsic pinning of layered structure or intrinsic pinning plus 1D APCs aligned along *ab*-plane. Intrinsic pinning may cause sharp J_c (θ) at θ=90^o while pinning including 1D APCs may cause wider peak at around θ=90^o. The latter is more convincing in this case as the wider J_c (θ=90^o) has been witnessed. This result is consistent with the APCs morphology shown in the TEM image Figure 17d.

3.4.2 Pinning force density $F_p(H)$

Figures 20a-c compare the pinning force density (F_p) calculated from $F_p=J_c$ x H at 77 K and 65 K as a function of H at different magnetic field (H) orientations of θ=0°, 45°, and 90° for 2 vol.% BZO and BHO DD films respectively. All $F_p(H)$ curves exhibit a typical inverted bell shape. The H_{max} at the peak of the F_p ($F_{p,max}$) corresponds to the matching field associated to the areal density of the APCs. At θ=0° (Figure 20a), the comparable H_{max} values for both films suggest that the concentrations of *c*-axis aligned 1D APCs are reasonably close to each other. However, the $F_{p,max}$ ~52.48 GN/m^3 for BZO DD nanocomposite film is about 1.5 times higher than that of the BHO DD counterpart at 65 K, at which point the T_c effect is negligible. The comparable H_{max} and higher $F_{p,max}$ values in the former is consistent with our earlier argument of the effectively longer *c*-axis aligned BZO 1D APCs.

This trend is certainly altered at θ=45° and 90° as shown in Figures 20b and 20c in which, higher H_{max} and $F_{p,max}$ values were observed on BHO DD films at both 77 K and 65 K. At 65 K and at θ=45°, the H_{max} ~8.5 T in the BHO DD film is more than twice of the ~4.0 T for the BZO DD film (Figure 20b). In addition, the $F_{p,max}$ ~26.71 GN/m^3 for the former is 1.14 times higher than that of 22.43 GN/m^3 for the latter. A similar trend is also seen at H//*ab*-plane (Figure 20c),

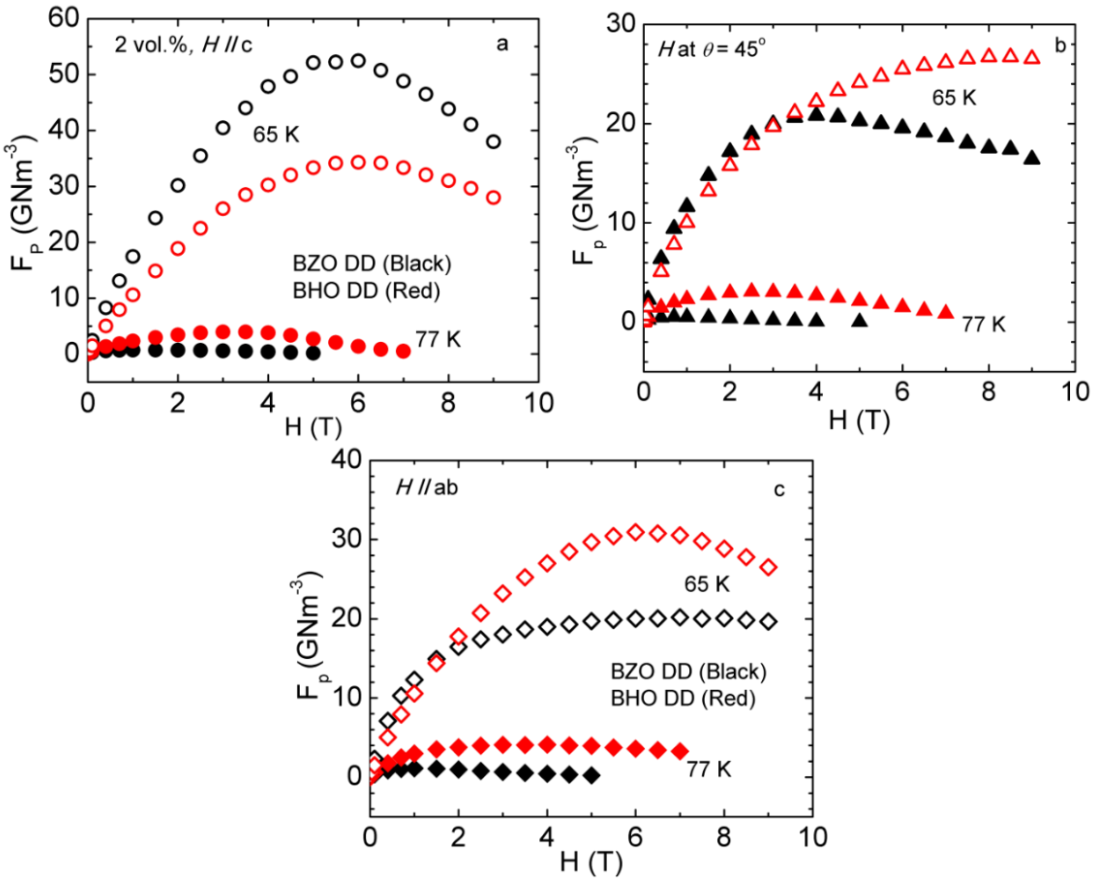

Figure 20: F_p vs. H curves for 2 vol.% BZO DD (black) and BHO DD (red) films at (a) H//c-axis ($\theta = 0^o$) (b) H at $\theta = 45^o$, and (c) H//*ab*-plane ($\theta = 90^o$) at 77 K (solid) and 65 K (open), respectively.

which indicates that the strong pinning in the BHO DD film case may be attributed the most probably to the shorter and misaligned BHO 1D APCs.

Figure 21 shows the temperature dependence of $F_{p,max}$ and H_{max} as a function of temperature. The $F_{p,max}$ and H_{max} both decrease monotonically with the increasing temperatures for BHO DD sample at $\theta = 0^o$ and $\theta = 45^o$. The comparable $F_{p,max}$ values (black) at these two angles in the temperature range of 50-77K, suggests BHO 1D APCs, instead of the Y_2O_3 3D APCs, are

probably the dominant at different H orientations. Much larger H_{max} values at lower temperatures and at θ=45° as compared to the θ=0°, indicates a larger number of smaller BHO APCs are also effectively involved in the BHO DD nanocomposite film. Remarkably, the H_{max} saturates at 8.5 T at 50 K in both orientations of θ=0° (H//c) and θ =45°. It suggests the same number density of BZO and BHO 1D APCs by the presence of the Y_2O_3 3D APCs are effective in vortex pinning.

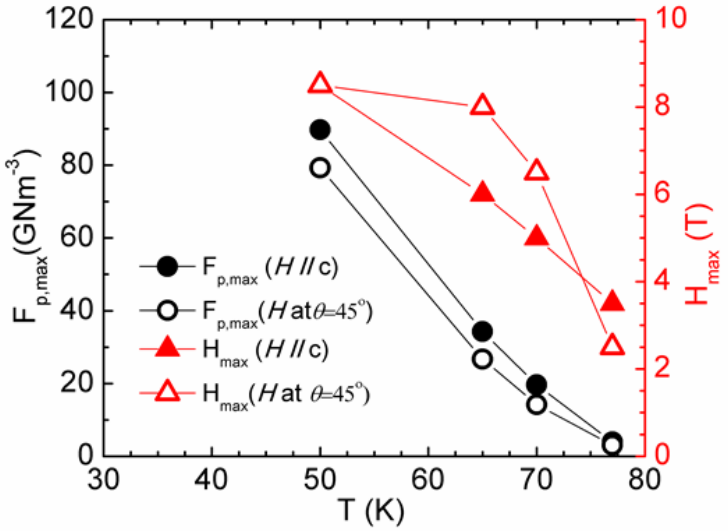

Figure 21: Temperature dependence of $F_{p,max}$ (circle) and H_{max} (triangle) measured at H//c-axis (solid), and H at θ =45° (open). The connecting lines are for eye catching purpose. Y-axis: left for $F_{p,max}$ and right for H_{max}.

Figures 22a-c compare the F_p (H) curves measured at the same conditions for 6 vol.% BZO or BHO DD nanocomposite thin films respectively. The higher $F_{p,\,max}$ for BHO DD film at H//ab-plane is observed compared to $F_{p,\,max}$ for BZO DD film at the same orientation of the field (H). At 65 K, when H//c-axis, about 1.5 times higher $F_{p,\,max}$ ~ 68.0 GN/m^3 for BZO DD film compared to $F_{p,\,max}$ ~45.78 GN/m^3 for BHO DD film. The lower H_{max}~7.0 T for BZO DD film compared to H_{max}~8.5 T for BHO DD film implies that the weaker pinning strength (measured through H_{max})

of BZO APCs compared to BHO APCs along *c*-axis. While, $F_{p,max}$ gap decreases when *H* is at θ=45° (Figure 22b) with $F_{p,max}$ ~40.65 GN/m^3 for BZO DD film. It is only about 1.3 times higher than BHO DD film due to the less effective BZO APCs at this angle.

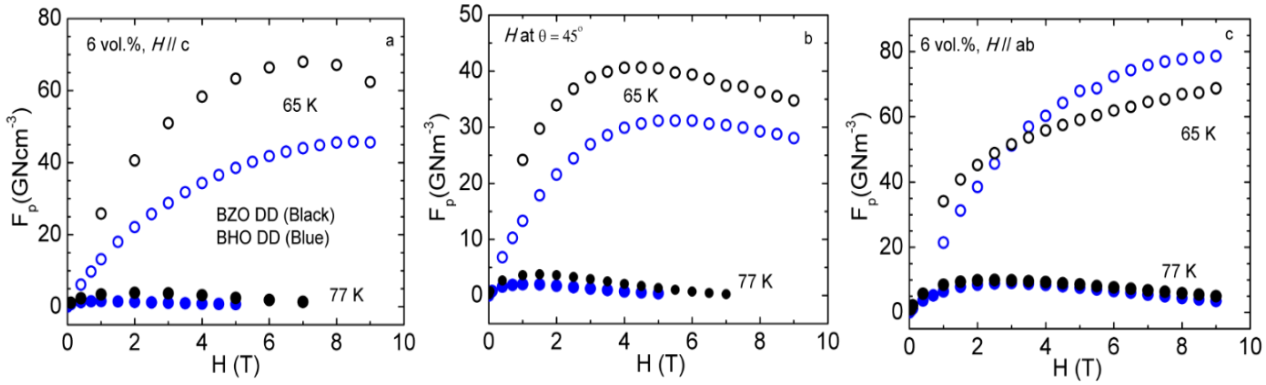

Figure 22: F_p vs. *H* curves measured on 3 vol.% Y_2O_3+6 vol.% BZO or BHO doped YBCO (BZO (black) or BHO (blue) DD) nanocomposite films at (d) θ =0° (*H*//c-axis), (e) θ = 45°, and (f) θ = 90° at 77 K (solid) and 65 K (open) respectively.

The higher H_{max} ~6.0 T for BHO DD film compared to H_{max} ~4.5 T for its counterpart suggests the higher pinning strength in BHO DD film. It further indicates the high effective areal density of segmented and misaligned BHO APCs. However, the same trend is not followed for the field *H*//*ab*-plane (Figure 22c) at which $F_{p,max}$ >78.63 GN/m^{3}for BHO DD is due to the strong pinning by BHO APCs in contrast to BZO APCs ($F_{p,max}$ ~68.72 GN/m^3). More interestingly, the constant gap of $F_{p,max}$ beyond 6.0 T, at *H*//*ab*-plane explores the fact that the almost an equal number of effective 1D APCs are involved in vortex pinning in both cases. The constantly increasing $F_{p,max}$ at *H* >6.0 T for 6 vol.% BHO DD also suggests that BHO APCs has more tunability in the presence of Y_2O_3 in contrast to BZO APCs. It further suggests that the orientation of 1D APCs more likely changes from *c*-axis alignment to *ab*-plane alignment with increasing

BHO concentration to 6 vol.% compared to similarly doped BZO film (Figures 22b and c). This result is different from BZO DD case in which 6 vol.% BZO DD film shows more isotropic at low temperature (≤ 65 K) in compared to lower BZO concentration [60]. The weaker rigidity in the BHO DD film enables a greater disturbance of the 1D APCs alignment to allow the BHO APCs to form in a more isotropic pinning landscape at low doping concentration, while at high doping of 6 vol.% BZO DD, the reversed results are obtained.

3.4.3 Angular dependent critical current density $J_c(\theta)$

To further explore the isotropic pinning, the $J_c(\theta)$ curves were measured at different magnetic fields for the entire angular range from *H*//*c*-axis to *H*//*ab*-plane, and at 77 K and 65 K as shown in Figure 23. The argument of the isotropic pinning is supported by the less variation i.e. more isotropic $J_c(\theta)$ curves observed on 2 vol.% BHO DD nanocomposite film as compared to the 2 vol.% BZO DD ones at both 77 K (Figure 23a) and 65 K (Figure 23b). One of the major differences in $J_c(\theta)$ curves of these thin films is that the absence of the J_c valley as θ is in between *H*//*c*-axis (θ=0º) and *H*//*ab*-plane (θ=90º) for the BHO DD nanocomposite film. The appearance of the J_c valley is the consequence of weaker pinning at this angular range as compared to the stronger pinning at *H*//*c*-axis (θ=0) due to very well aligned with the c-axis 1D APCs, and at *H*//*ab*-plane (θ=90º) due to the intrinsic pinning by the crystalline structure of YBCO nanocomposite film.

The appearance of such a J_c valley leads to the J_c anisotropy with respect to magnetic field (*H*) orientations. This J_c anisotropy with respect to the *H* orientations is quantitatively expressed

using the normalized J_c variation between the highest J_c ($J_{c,\ max}$) at the larger of the J_c peaks and the lowest at the J_c valley by ($J_{c,\ max}$ - $J_{c,\ min}$) /$J_{c,\ min}$. The larger the difference between the J_c peaks and J_c trough ($J_{c,\ min}$) for the entire angular range as in the most 1D APC/YBCO nanocomposite thin film, the larger the J_c anisotropy is observed [24, 25]. For example, the J_c anisotropy is about

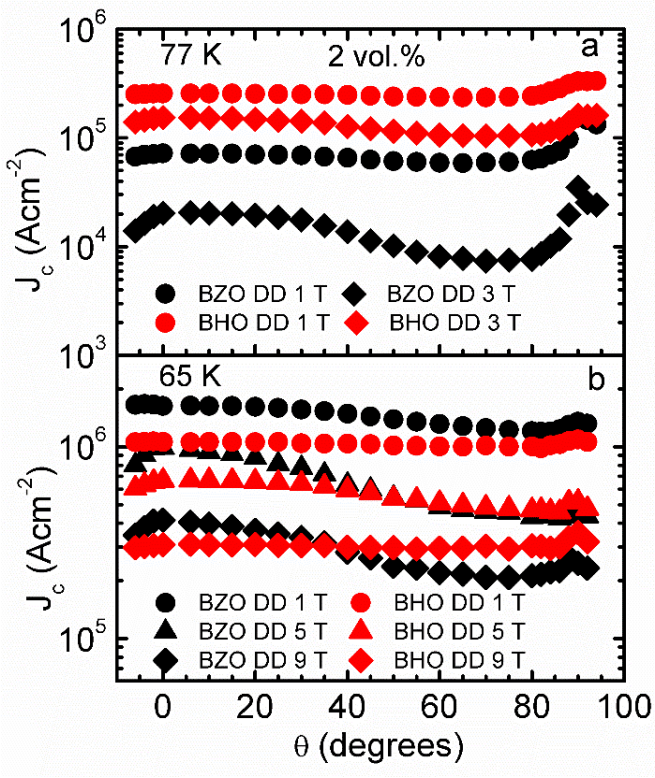

Figure 23: Angular dependence of J_c measured on 2 vol.% BZDD (black) and BHO DD (red) nanocomposite thin films (a) at 1 T (circle) and 3 T (diamond) at 77 K (b) 1 T (circle), 5 T (triangle), and 9 T (diamond) at 65 K respectively.

100% for 2.0 vol.% BZO SD films at 77 K and 1.0 T [34], which is similar to the 3.0 vol.% BSO SD films [33]. However, higher J_c anisotropy of 160.0% for BZO DD nanocomposite film (Table 1) with $J_{c,\ min}$ =0.59×10^5 A/cm^2 in this study suggests that most BZO 1D APCs are remained aligned to *c*-axis improving correlated pinning. At 77 K, and at *H*=1.0 T, the overall J_c (θ) values for the entire angular range from *H*//*c*-axis (θ=0^o) to *H*//*ab*-plane (θ=90^o) are higher in the BHO DD film in this study than in the BHO SD films reported previously [24]. In addition, the J_c anisotropy is about 41% for the BHO DD film, which is about a half of ~80% for the BHO SD film reported in ref. [57]. This result seems consistent with the higher orientation tunability of the BHO 1D APCs in the double doped (DD) nanocomposite thin films as predicted in Figure 14.

The J_c anisotropy is calculated as about 40% for the 2 vol.% BHO DD film measured at 77 K at 1.0 T. Interestingly, J_c anisotropy is almost the same ~42-43% on both 2 vol.% BZO and BHO DD nanocomposite films at the moderate field of 5.0 T and at 65 K. This value is further reduced to about 18% for the 2 vol.% BHO DD films at 65 K and 9.0 T (red diamonds), in contrast to about 100% for the BZO DD counterpart (black diamonds) as shown in Figure 23b. This result illustrates the importance of engineering the APC morphology and orientation.

Figure 24 compares the J_c (θ) curve of 6 vol.% BZO and BHO DD nanocomposite thin films at the magnetic field of 5.0 T and 9.0 T for the entire angular range from *H*//*c*-axis to *H*//*ab*-plane, and at 65 K. Interestingly, these curves do not follow the same trend as 2 vol.% DD films and at 65 K (Figure 23b). The overall higher and increased value of J_c (θ) for a wide angular range of 6 vol.% BZO DD film is indication of strong and effective pinning by mixed APCs morphology

compared to 6 vol.% BHO DD film. There is an absence of J_c peaks at H//c-axis in 2 vol.% BHO DD film (Figure 23b) appears at 6 vol.% BHO DD films (Figure 24). These J_c peaks are more clearly observed at H//c-axis and H//ab-plane for both 6 vol.% DD films.

The J_c anisotropy of 6 vol.% BZO DD at 5.0 T is about 60% compared to 111% for BHO DD film. In addition, at 9.0 T, J_c anisotropy is about 92% for the BZO DD film which is almost half of the BHO DD film (173%). The increasing J_c anisotropy in BHO DD film may be due to increasing J_c peak towards the ab-plane instead J_c peak at c-axis. This is different from 6 vol.% BZO DD film at which J_c peaks appear at around c-axis (Figure 24).

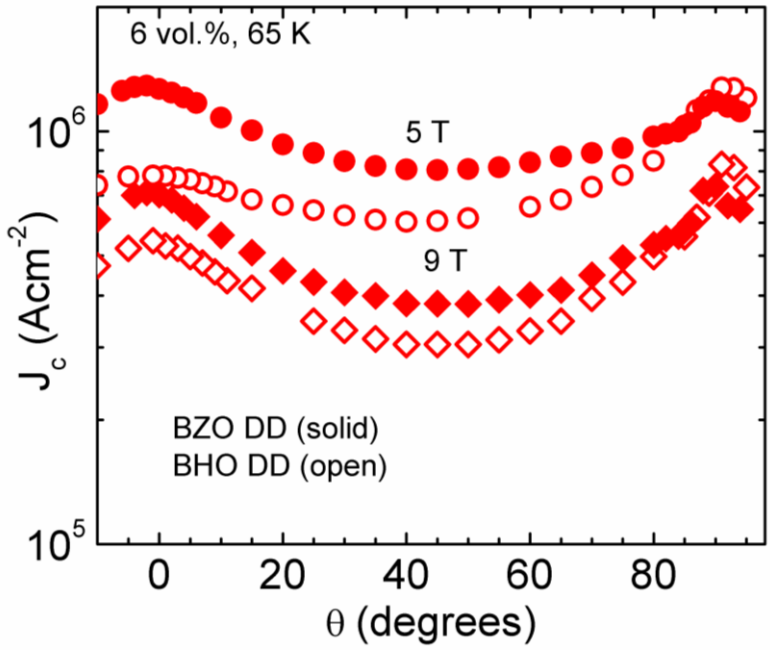

Figure 24: Angular dependence of J_c measured on 3% Y_2O_3+6 vol% BZO or BHO doped YBCO (BZO or BHO DD) nanocomposite films measured at 5.0 T (circle), and 9.0 T (diamond) at 65 K respectively.

It means at 6 vol.% BZO DD film, the overall more isotropic pinning is observed in contrast to 6 vol.% BHO DD film which is not the same as in low 2 vol.% BHO doping case (Figure 23). This illustrates that the influence of Y_2O_3 in BZO and BHO 1D APCs is different, more in the latter compared to the former. In one of our separate studies, 6 vol.% BZO DD film shows the reduced J_c anisotropy of ~44% at 77 K and at 1.0 T which is considerably less than the J_c anisotropy~57% of 6 vol.% BZO SD film, both fabricated at 5^o STO vicinal substrate [61]. This further illustrates that the combination of double doping and vicinal substrate would be a promising technique to enhance strong and isotropic pinning. However, the study of the BHO double doped YBCO nanocomposite film on the vicinal substrate has not been done till date. This would pose valuable to understand the strained mediated self-assembly of the APCs morphology for strong and isotropic pinning.

3.5 Microscopic adaptation of APCs in BHO double doped nanocomposite thin films

Previously explored in this paper, the low doping (2.0 vol.%) of BHO in double doped YBCO nanocomposite films provides strong and isotopic pinning reducing J_c anisotropy to about 20% at high field of 9.0 T and at 65 K. While increasing BHO doping to 6 vol.% J_c anisotropy is increased due to strong pinning along *ab*-plane instead along *c*-axis. Moreover, the theoretical model [20, 53] and experimental results verify that the BHO 1D APCs are more flexible to "tuned" away from the *c*-axis alignment in APC/YBCO nanocomposite films. Such results encourage to explore the APCs morphological adaption of BHO 1D APCs to Y_2O_3 3D APCs at a moderate

doping concentration of BHO in double doped YBCO nanocomposite film. This will provide an opportunity to explore and generate strong and isotropic pinning landscape through mixed morphology of APCs.

Thus, in this section, it is explained that the systematic study of the electrical transport properties J_c (H, T, θ) of 2.0-6.0 vol.% BHO plus 3 vol.% Y_2O_3 doped YBCO (BHO DD) nanocomposite thin films and APC nanostructures of these films in TEM images. With a moderate BHO concentration in the DD films, we aim to understand the reasonable doping concentration on the mixed 1D+2D+3D APCs morphology to generate strong and isotropic pinning landscape.

Figure 25 shows the low and high magnification cross-sectional TEM images of the 4 vol.% BHO DD films, respectively. As this BHO concentration of BHO doping, the APC morphology becomes more mixed with many 1D, 2D, and 3D APCs visible clearly which is different from the 2 vol.% and 6 vol.% BHO DD films as given in Figure 17. At 2 vol.% only few 3D APCs with more *c*-axis aligned APCs are observed while at 6 vol.% many 2D APCs along with *ab*-plane aligned 1D APCs are also visible. However, at 4 vol.% BHO DD film many through-thicknesses 1D APCs are truncated by 2D APCs in the *ab*-plane into shorter segments along the *c*-axis. Some of these 1D and 2D APCs are not connected, with 3D APCs located in between the nearest neighbors.

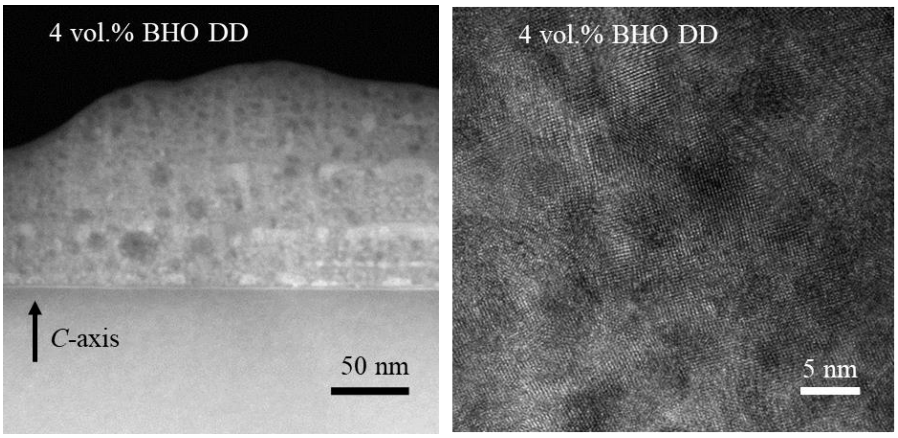

Figure 25: TEM images of 4 vol. % BHO DD nanocomposite films left: at Low magnification and right: at high magnification. Scale bar 50 nm and 5 nm for low and high magnification respectively.

A zoom-in view of the microstructure of the 4 vol.% BHO DD film reveals the APCs typically have their smaller dimension on the order of 5-10 nm. Since the Y_2O_3 doping is the same in all BHO DD samples, the increased 2D and 3D APC concentrations in the 4 vol.% BHO DD nanocomposite film as compared to the 2 vol.% BHO DD film indicates the increased BHO doping increases the concentrations of 1D, 2D and 3D APCs proportionally. This trend of switching of 1D BHO APCs to other morphologies continues with increasing BHO concentrations. At 6 vol.% BHO higher concentration and more continuous 2D APCs in the *ab*-plane are clearly seen (Figure 17), in addition to shorter BHO 1D APCs along *c*-axis together with 3D APCs. Based on the TEM observation, it can be confirmed that in BHO DD films, mixed (1D+2D+ 3D) APCs morphology is formed as illustrated schematically in Figure 26.

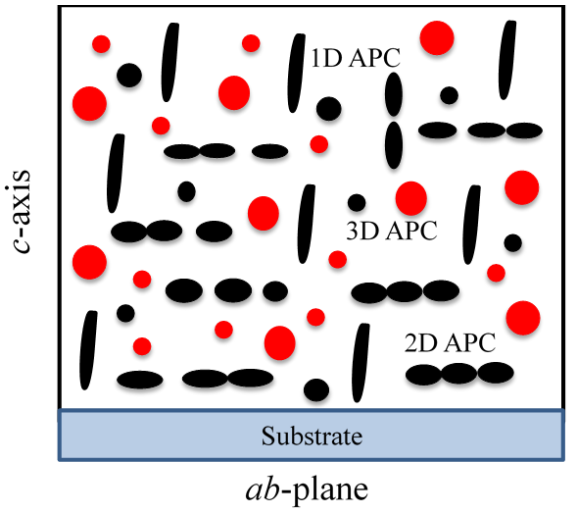

Figure 26: Schematic of the microstructure distribution in the *c*-oriented BHO double doped YBCO film matrix. Color codes: BHO 1D, 2D and 3D APCs (black), Y_2O_3 3D APCs (red).

Figures 27a-b and 27c-d compare the J_c (H) and F_p (H) curves measured on 2, 4, and 6 vol.% BHO DD films at the field orientations H//c-axis (θ=0°) and H at θ=45° at 77 K (solid) and at 65 K (open) respectively. At θ=0°, the 4 vol.% BHO DD film (black) has the highest J_c (H) at both 77 K and 65 K despite having a slightly lower T_c than that of the 2% BHO DD sample. The J_c (H) curves for the 2 and 4 vol.% BHO DD films have qualitatively similar trends at both temperatures. The different trend of the J_c (H) curve for the 6 vol.% BHO DD sample at 77 K may be attributed to the lower T_c (Table 1) because, at 65 K, J_c (H) curves show the similar trend. However, the lower J_c (H) values of the 6 vol.% BHO DD film may be partly due to the reduced areal density of the *c*-axis aligned BHO 1D APCs and reduced pinning efficiency of segmented short BHO 1D APC as observed in TEM image at Figure 17. The alpha (α) values for the 2 and 4 vol.% BHO DD films are 0.26 and 0.35 at 77 K, and 0.16 and 0.13 at 65 K respectively indicate an enhanced correlated pinning by the *c*-axis aligned BHO 1D APCs and is increased at lower

temperatures. In contrast, a significantly higher α ~0.64 value at 77 K and much lower α ~0.2 at 65 K for the 6 vol.% BHO DD film supports our earlier argument of the combined effect of the lower T_c and lower pinning efficiency of the short *c*-axis aligned BHO 1D APCs at 77 K. This suggests a portion of *c*-axis aligned 1D APCs switches to the *ab*-plane aligned in this film which reflects on the high J_c (*H*) *at H*//*ab*-plane (Figure 27a).

The highest J_c (*H*) of the 4 vol.% BHO DD film at both 77 K and 65 K lead to the highest overall F_p (*H*) values as well. All F_p (*H*) curves in Figures 27c-d have inverted bell shape with the peak value defined as $F_{p,\,max}$ at H_{max}. At *H*//*c*-axis and neglecting T_c effect at 65 K, the $F_{p,\,max}$ ~68.0 GN/m^3 at H_{max} ~7.0 T can be observed for the 4% BHO DD film, which is higher than the 60.4 G N/m^3 and 4.0 T of the BHO SD films with the comparable doping [27], illustrating the benefit of the DD in terms of both enhanced APC concentration. In addition, increasing BHO concentration beyond ~4 vol.% adds on additional APCs as reflected in the further enhanced H_{max}~8.5 T for 6% BHO DD at 65 K (Figure 27c). Although the additional BHO doping adds more APCs the $F_{p,\,max}$ ~46.0 GN/m^3 for the 6 vol.% BHO DD film indicates the additional 2 vol.% BHO doping may not form 1D APCs through thickness as expected in 6 vol.% BHO DD film and confirmed in TEM. The mixed APC morphologies shown in the TEM analysis (Figures 17 and 25) of the BHO DD samples are expected to change the anisotropy of J_c considerably.

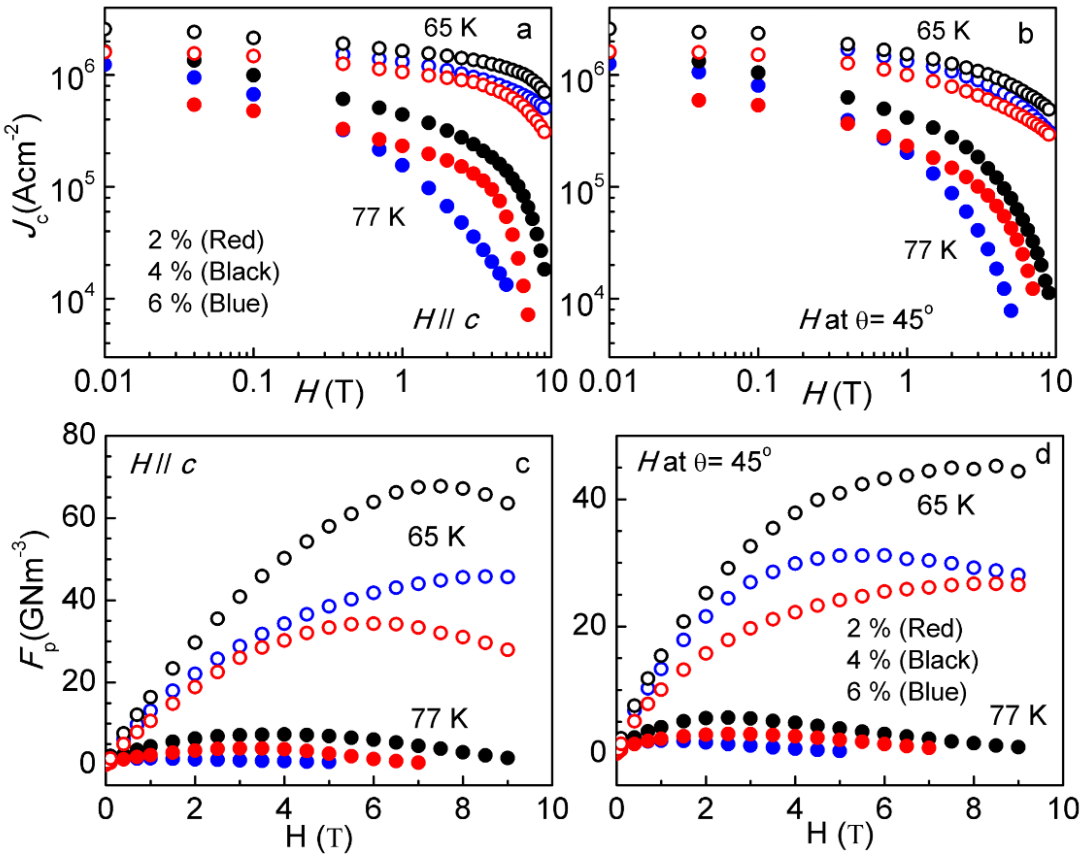

Figure 27: J_c vs. H and F_p vs. H curves measured on 2,4 and 6% BHO DD nanocomposite films at (a) and (c) $H//c$-axis ($\theta=0^o$), (b) and (d) H at $\theta = 45^o$ at 77 K (solid) and 65 K (open), respectively. Color codes follow the same for all figures. These Figures are adapted from Gautam et.al, SuST, 2018 [58].

In contrast to the BHO SD samples in which BHO 1D APCs are long and well aligned at the *c*-axis only, the BHO APCs in the DD films have mixed APCs morphologies. A combination of 1D short segments of BHO along the *c*-axis for strong correlated pinning and irregular shaped APCs of BHO and Y_2O_3 that can provide pinning in other directions. The concentration of the *c*-axis aligned 1D BHO APCs increases with BHO doping in the range of 2-6 vol%.

The similar increase of the concentration of the irregular shaped 3D APCs can be explained as a strong pinning at θ=45° in 4 vol.% BHO DD nanocomposite thin film, while leads to their merge into planar APCs along the *ab*-plane in the 6% BHO DD thin film. This results in decrease (increase) of the 3D (2D) APCs as the BHO doping is increased from 4 vol.% to 6 vol.% (Figures 17 and 25).

Samples	alpha (α) values					
	77 K			65 K		
	H // *c*	*H* at θ=45°	*H* // *ab*	*H* // *c*	*H* at θ=45°	*H* // *ab*
2.0 % BHO DD	0.26	0.29	0.23	0.16	0.25	0.20
4.0 % BHO DD	0.35	0.40	0.40	0.13	0.23	0.24
6.0 % BHO DD	0.64	0.59	0.27	0.20	0.24	NA

Table 2: Alpha (α) values of 2, 4, and 6 vol.% BHO DD films at different field orientations and temperatures.

At *H* at θ=45° (Figure 27b), the J_c (*H*) curves for the 2, 4, and 6 vol.% BHO DD nanocomposite films have similar trends at 77 K and 65 K to the case of *H*//*c*-axis, except less *H* susceptibility of J_c (*H*) for the 6 vol.% BHO DD film. In addition, the three J_c (*H*) curves almost overlap at the lower temperature of 65 K, indicative of similar pinning mechanism at these BHO concentrations. This argument is consistent to the comparable α values of 0.25, 0.23, and 0.24 (Table 2) for the 2, 4, and 6% BHO DD films respectively at 65 K. However, the F_p (*H*) at θ= 45° (Figure 27d) reveals different H_{max} values for these three samples. The highest $F_{p,max}$ of 45.0 GN/m^3 is still for 4 vol.% BHO DD film indicates the effective pinning by mixed APCs morphology. A comparable $F_{p,max}$ of ~ 28 GN/m^3 and 31 GN/m^3 respectively for 2 vol.% and 6

vol.% BHO DD films, the comparable H_{max} ~8.0 and 8.05 T at 65 K suggests a comparable pinning efficiency of 3D APCs (Figure 27b). However, the drop to the lowest H_{max} ~6.0 T for the 6 vol.% BHO DD film indicates the reduced areal density of effective APCs, which could be either Y_2O_3 3D APCs or short/misaligned segment of 1D APCs. Assuming the Y_2O_3 3D APCs concentration is not changed in entire films, the decrease in the concentration of 3D APCs may be attributed to the complete switch of *c*-axis aligned BHO 1D APCs to *ab*-aligned 2D APCs in the 6 vol.% BHO via connection of those segmented *ab*-aligned APCs in 4% BHO DD nanocomposite film. This argument is consistent with the TEM observation discussions in Figures 17 and 25.

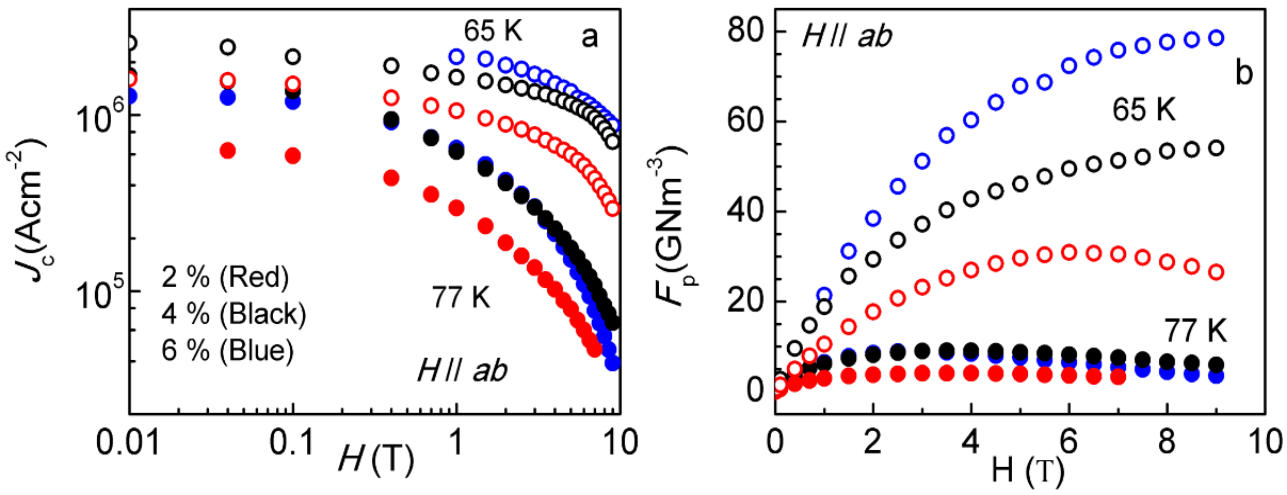

Figure 28: J_c vs. H (a) and F_p vs. H (b) curves measured on 2,4 and 6% BHO DD nanocomposite films at *H//ab*-plane (θ=90°) at 77 K (solid) and 65 K (open), respectively. Color codes follow the same for all figures.

This argument of switching of *c*-axis aligned 1D APCs to *ab*-plane aligned APCs is also supported by the much improved $J_c(H)$ and $F_p(H)$ curves of the 6 vol.% BHO DD nanocomposite film at *H*//*ab*-plane (Figures 28a and 28b). The increasing trends of the *ab*-aligned APCs pinning efficiency are expressed in H_{max} and $F_{p,max}$ with increasing BHO doping can also be found in Figures 29a-b. At 65 K, the H_{max} >9.0 T (instrument limit) for the 4.0 vol.% and 6 vol.% BHO DD thin films is higher than H_{max} ~6.5 T for 2 vol.% BHO DD film at *H*//*ab*-plane (θ= 90°).

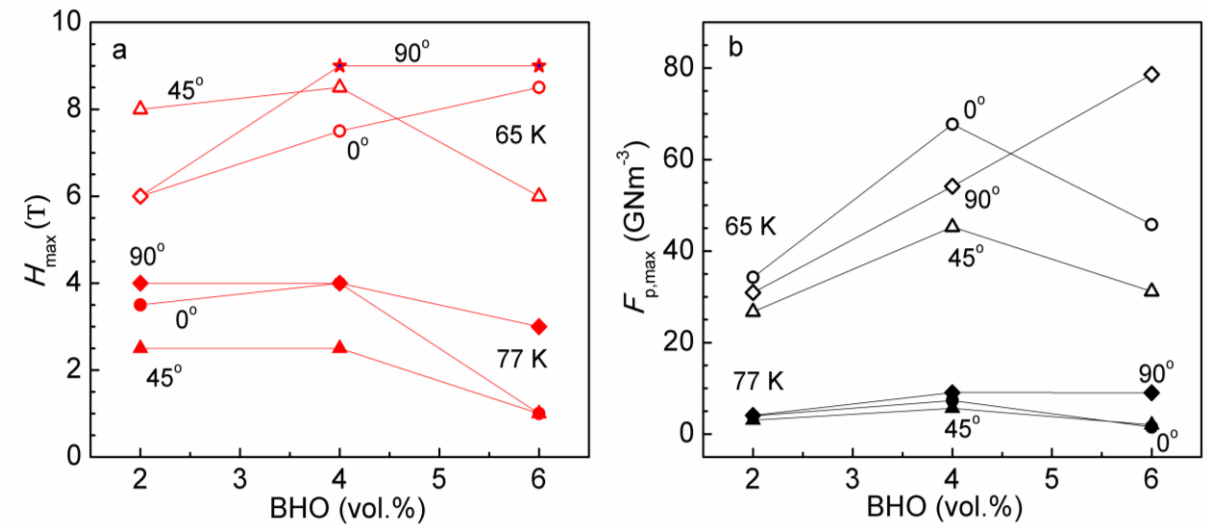

Figure 29: BHO doping concentration dependence of (a) H_{max} and (b) $F_{p,max}$ measured at 77 K (solid) and at 65 K (open), on *H*//*c*-axis (circle), *H* at θ =45 degrees (triangle) and *H*//*ab*-plane (diamond) of 2, 4 and 6 vol.% BHO DD nanocomposite films. ★ indicates the value from the instrument limit. Connecting lines are for eye catching purpose.

In addition, the $F_{p,max}$ at *H*//*ab*-plane is increased by 1.5 times for each additional 2.0 vol.% BHO doping concentration ($F_{p,max}$ ~31.0 GN/m^3, 54.0 GN/m^3, and 79.0 GN/m^3 for 2, 4, and 6 vol.% BHO DD films respectively) as shown in Figure 29. The significantly higher $F_{p,max}$ ~79.0 GN/m^3 at *H*//*ab*-plane compared to $F_{p,max}$ ~45.78 GN/m^3 at *H*//*c*-axis for the 6 vol.% BHO DD film (Figure 29) is consistent with the TEM images, and support the argument of switching of 1D APCs from

c-axis to *ab*-plane alignment. This could be possible by decreasing compressive strain along *c*-axis added by Y_2O_3 and increasing tangential strain along *ab*-plane with BHO concentration correlates with the APCs morphology observed in Figure 17 for 6 vol.% BHO DD film. This trend is contrasting to the similar doping of BZO in 6 vol.% BZO DD film at which J_c (*H*//*c*-axis) is enhanced [60].

Figures 30a-b illustrate the $J_c(\theta)$ curves at the 1.0 and 3.0 T at 77 K, and 1.0, 5.0, and 9.0 T at 65 K, respectively. With increasing doping concentration of BHO, the appearance of J_c valley in these $J_c(\theta)$ curves for the entire angular range from *H*//*c*-axis to *H*//*ab*-plane is an indication of decreasing isotropic pinning with increasing BHO doping at given field and temperature. The much reduced J_c anisotropy~40% for 2% BHO DD than J_c anisotropy~104% for 4 vol.% BHO DD at 77 K, 1.0 T, and J_c anisotropy ~18% which is 3.0 and 9.0 times less compared to J_c anisotropy~56% and 173% for 4 and 6% BHO DD film respectively at 65 K and 9.0 T (Table 1) indicates the strong isotropic pinning in the former compared to the latter two films. The overall uplifted $J_c(\theta)$ curve with two comparable distinct peaks at *H*//*c*-axis and *H*//*ab*-plane at *H*~ 5.0 and 9.0 T for 4 vol.% BHO DD film show enhanced strong pinning and can be attributed to the mixed APCs morphology observed in TEM images of 4 vol.% BHO DD film (Figure 25). At 65 K, the highest J_c anisotropy ~111% and 173% at 5.0 and 9.0 T respectively for 6% BHO DD film could be due to lack of 3D APCs or the higher J_c peaks at *H*//*ab*-plane due to strong pinning by *ab*-aligned 2D APCs. However, equivalent $J_{c,min}$ with comparable J_c (θ=30-60^o) for 2 vol.% and 6 vol.% BHO at 65 K and 9.0 T explores; the increased BHO doping concentration beyond the

threshold value (4 vol.% in this study) doesn't improve the isotropic pinning. This is in contrast to 6 vol.% BZO concentration in BZO DD films [60] at their optimal growth temperature. It further suggests that possibly Y_2O_3 3D APCs or BHO 3D APCs are more effective than misaligned BHO

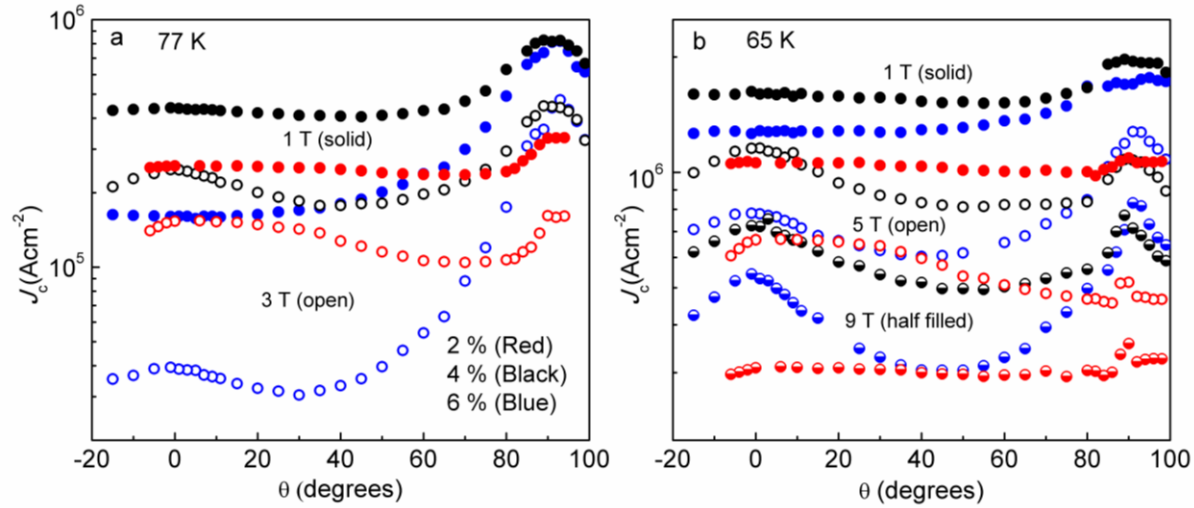

Figure 30: Angular dependence of J_c measured on 2, 4 and 6 vol.% BHO DD nanocomposite films at (a) 77 K, and 1.0 T (solid) and 3.0 T (open), (b) 65 K, and 1.0 T (solid), 5.0 T (open), and 9.0 T (half filled) circles. Color codes follow the same for both figures. These Figures are adapted from Gautam et.al, SuST, 2018 [58].

1D APCs at the given angular range. The wider J_c peak at *H*//*ab*-plane observed in 4 vol.% and 6 vol.% BHO films attribute to the possible switch of 1D APCs from *c*-axis alignment to *ab*-plane alignment. A sharp peak is expected in case of intrinsic pinning by YBCO structure [62, 63]. It is consistent and comparable to the switching of BZO 1D APCs from *c*-axis to *ab*-plane in the vicinal substrate as the vicinal angle increased to 15^o [62, 63] Comparing the J_c (θ) at 77 K and at 1.0 T [62, 63], the similar trend of increasing J_c (θ) curve towards the θ=90^o (*H*//*ab*-plane) especially away from θ=30^o attributes the distribution of BZO 1D APCs and their morphology should be similar to 1D APCs in 6 vol.% BHO DD with additional Y_2O_3 3D APCs in the film.

3.6 Conclusions

In this study, we probe the tunability of the 1D APCs alignment along the *c*-axis by a secondary Y_2O_3 3D APCs and explore the strong and isotropic pinning in BZO (or BHO)/YBCO nanocomposite films. The tunability agrees with the nanostructures of the APCs, which in turn affects the J_c anisotropy with respect to the magnetic field (*H*) orientations. Electrical transport J_c (*H, T*, θ) is measured for varying doping concentration 2 vol.%-6 vol.% in the temperature range of 50-77 K at the magnetic field up to 9.0 T, and *H* at different orientations. The conclusions are summarised as follows:

The higher tunability of the BHO 1D APCs by the Y_2O_3 3D APCs are found experimentally and agree well the theoretical prediction compared to the higher rigidity the BZO 1D APC counterparts. Hence, a significantly reduced J_c anisotropy is calculated in 2-4 vol.% BHO DD films due to the formation of short, misaligned and mixed APCs morphology enhancing isotropic pinning. Specifically, at the 2.0 vol.% BHO doping concentration J_c anisotropy is reduced to ~18% which is about 3.0 to 5.0 times lower than that of higher 4 vol.% and 6 vol.% BHO doping concentration respectively.

At 6.0 vol.%, doping concentration the overall higher J_c (θ) values are observed in BZO DD samples for wide angular range from *H*//*c*-axis at 65 K except around *H*//*ab*-plane. The higher J_c peak at *H*//*ab*-plane (θ=90^o) is attributed to the effective BHO APCs to *ab*-plane alignment at the higher strain field overlap as compared to the BZO counterparts.

A systematic change in the proportion of each kind of APCs has been observed with an increasing BHO doping concentration from 2 to 6 vol.%. This is primarily due to the switch of the longer (mostly through film thickness) BHO 1D APCs (in *c*-axis) at lower BHO concentrations to the shorter and more misaligned segments at higher BHO concentrations. Such a switch is a consequence of the higher adaptability of the BHO APCs to the presence of the Y_2O_3 3D APCs. It is expected to impede the diffusion of BHO during the nucleation and growth of the films introducing local strains on the APC/YBCO nanocomposites to prevent the formation of perfectly *c*-axis aligned BHO 1D APCs. The overall best J_c (H, θ) has been observed for 4 vol.% BHO DD nanocomposite films at 65-77 K. This suggests double doping as an effective approach for the generation of mixed APCs morphology and engineering the strong and isotropic pinning landscape.

Chapter 4 Pinning Efficiency of BZO and BHO 1D APCs and the Interface Effect

A key to the high J_c (H) for practical application of HTS materials is due to the strong correlated pinning by *c*-axis aligned 1D APCs in rare earth RE (=Y, Sm, Gd) $Ba_2Cu_3O_7$ (REBCO) nanocomposite thin films. Several materials such as $BaZrO_3$ (BZO) [15, 27, 28, 59, 64], $BaSnO_3$ (BSO) [27, 65, 66], $BaHfO_3$ (BHO) [8, 67, 68], and $YBa_2(Nb/Ta)O_6$ [69] have been studied for the self-assembled 1D APCs along the *c*-axis of the films during nucleation and growth process. They provide strong pinning of the vortices when the applied magnetic field H is along the axial direction of the 1D APCs. Chapter three discussed qualitatively how elastic properties of the material such as rigidity, elastic constant, lattice mismatch, and doping concentration play a deterministic role on APCs morphology. In particular, the comparable diameter of about 5-6 nm for the BHO and BZO 1D APCs in REBCO matrices, the BHO APCs [30] shows the more adaptive behaviors to the local strain generated by a secondary Y_2O_3 3D APCs doping and hence form mixed APCs morphology for isotropic pinning landscape [13]. However, the pinning efficiency of the 1D APCs has not been studied systematically that could be affected by the interface of 1D APCs with the REBCO matrix. The higher adaptivity, smaller lattice mismatch of BHO with YBCO together as compared to that of the BZO/YBCO smaller interface energy is anticipated. This raises a fundamental question on what determines the pinning efficiency of different 1D APCs and to what extent the interfaces would affect the pinning efficiency of the individual BHO and BZO 1D APCs.

Controlling the interface effect on pinning efficiency of 1D APCs is challenging for optimal pinning efficiency.

This chapter explores the answers to these questions and investigates the relation between 1D APC/YBCO interface and the pinning efficiency of 1D APCs of BHO and BZO doping materials. The work in this chapter presents a study of the transport J_c measurement at 65-77 K and magnetic field (H) up to 9.0 T for 2-6 vol.% BHO/YBCO and BZO/YBCO nanocomposite films. For nanostructure APCs morphology and interface with YBCO, high-resolution transmission electron microscopy (HRTEM) images will be discussed. The pinning efficiency is evaluated from the maximum value ($F_{p,\,max}$) of the force density $F_p=J_c\times H$ and its location at H_{max}. Intriguingly, a highly coherent BHO 1D APC/YBCO interface is revealed even at high BHO doping concentration of 6 vol.%, in contrast to a semi-coherent BZO 1D APC/YBCO interface with many interfacial dislocations. This leads to a significant effect on the pinning efficiency of the 1D APCs in YBCO matrix.

4.1 The effect of APC/REBCO interface on pinning efficiency of 1D APCs: a qualitative interpretation

Theoretically, the pinning potential energy is proportional to the sharpness of the APC, (insulator)/REBCO (superconductor) interface and hence the interface is a key to determining the high pinning efficiency. For an atomically sharp interface, an optimal pinning efficiency is anticipated. The interface between the 1D APC and REBCO matrix is generally strained and defective. Figure 31 illustrates a schematic of the magnitude of the superconducting order

parameter $|\phi|$ as a function of the distance from the 1D APC added to the HRTEM image of a strained interface at BZO 1D APC/REBCO reported by Cantoni *et al* [38]. In addition, theoretically calculated strain distribution based on a coherent APC/REBCO interface (blue curve in Figure 31b), and the experimentally measured one (red curve in Figure 31b) is compared to illustrate the two T_c regions in the column surrounding a 1D APC. The larger column of T_{c1}< $T_{c,YBCO}$ (the T_c of the original YBCO) is primarily due to the strain originated from the BZO/YBCO lattice mismatch along the *c*-axis. The even lower T_{c2} in the smaller column immediately outside the BZO 1D APC is attributed to the defects especially oxygen deficiencies nearby the interface as marked by white arrows in Figure 31a. This is the main cause of the deviation of the strain distribution in this column from the theoretical curve for a coherent BZO/REBCO interface.This means the pinning potential well height (red) and hence the pinning efficiency of the BZO 1D APCs would be much reduced since $T_{c2} < T_{c1}$ as suggested in [38]. The oxygen deficient column of few nm in thickness leads to a lower T_{c2} ~60-70 K [38] than the T_{c1} (5-6 K lower than $T_{c,YBCO}$) in the larger strained column [25, 38, 39]. The detrimental impact of the semi-coherent BZO 1D APC/YBCO interface may be attributed quantitatively to the large lattice mismatch along the *c*-axis of YBCO and BZO and higher rigidity of the BZO APCs. On the other hand, the coherent interface with strained YBCO/APC lattice attributed to the smaller lattice mismatch along *c*-axis as well as less rigidity of APCs which may enhance pinning potential well height, hence pinning efficiency [39].

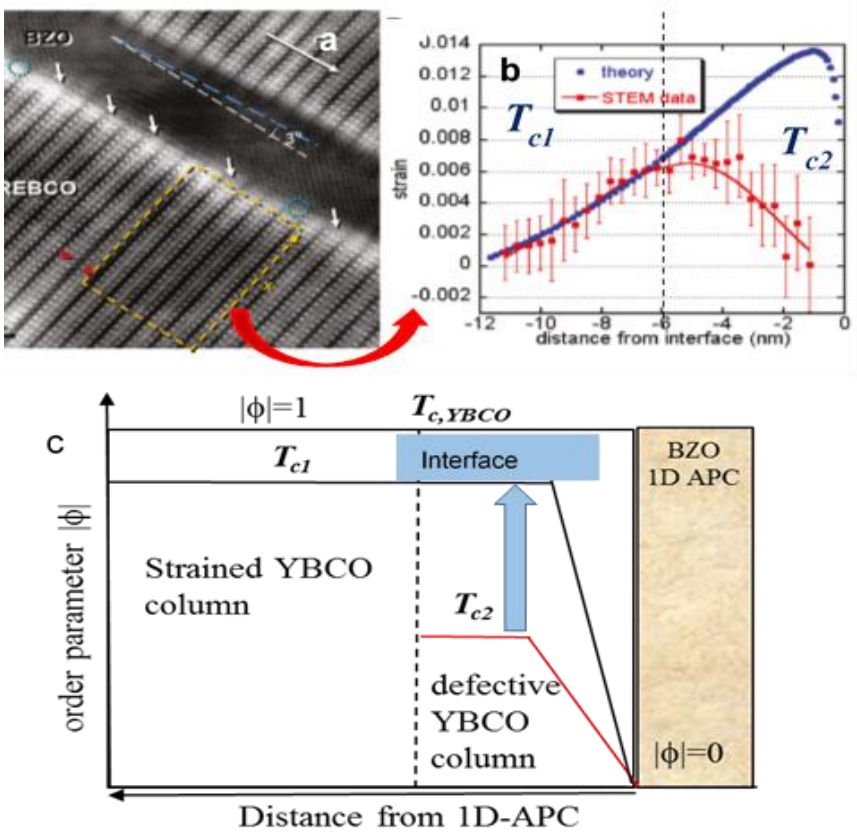

Figure 31: (a) HRTEM of BZO/YBCO interface (b) calculated strain (blue) and HRTEM measured strain distributions in YBCO around the 1D BZO/YBCO (red). This Figure is adapted from Cantoni et.al, NM, 2013 [38], (c) schematic of the cross-sectional view of the superconducting parameter $|\phi|$ as function of the distance from the BZO 1D APC. Two concentric YBCO columns are depicted in the figure surrounding the 1D APC with the larger one representing the strained YBCO of T_{c1} and the smaller one of lower T_{c2} due to defective semi-coherent BZO 1D APC/YBCO interface. The blue arrow illustrates the effect of BZO/YBCO interface may repair inducing cations to reduce the oxygen disorder and hence raise the T_{c2}.

4.2 Nanostructure analysis and accommodation field (H^*)

Figures 32a-f illustrate the cross-sectional HRTEM images of the 2-6 vol.% BZO and BHO APC/YBCO nanocomposite films with the 1D APCs extended through the film thickness. The average diameter and spacing between 1D APCs are quantified analyzing 80-100 cross-sectional

TEM images at different areas of each sample [34]. The details are summarized in Table 3. Although the diameter of BZO 1D APCs increases from 5.2 nm to 5.9 nm [36], the decreasing average spacing (measured from center to center of the nearest-neighbors 1D APCs) monotonically from about 20 nm to 12 nm [62, 63] indicates a monotonic increase of BZO 1D APC areal concentration n^*_{BZO} with the BZO doping concentration from 2.0 vol.% to 6.0 vol.%. Assuming square lattice, the H^* is estimated to be 5.2 T, 9.2 T, and 14.3 T at 2.0 to 4.0, and to 6.0 vol.% BZO doping levels, respectively (Table 3).

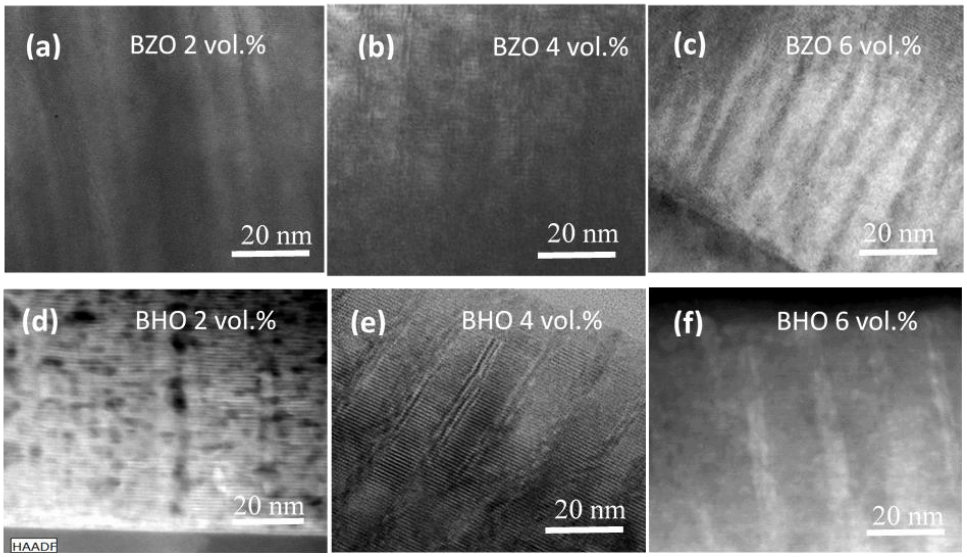

Figure 32: Cross sectional TEM images of YBCO nanocomposite films doped with: (a) and (d) 2 vol.%, (b) and (e) 4 vol.%, and (c) and (f) 6 vol.% BZO and BHO respectively. Scale bars are 20 nm.

The linearly increasing n^*_{BZO} with the BZO doping is a manifestation of defective BZO 1D APC/YBCO interface column of 1-2 nm in thickness surrounding the BZO 1D APC. This effect not only releases the strain to almost zero at the interface but also reduces the strain on YBCO significantly [38]. As discussed in previous sections, severe oxygen deficiency 1-2 nm next to

BZO/YBCO is the main reason of poor pinning efficiency of 1D APCs than that further away due to the defect formation at the highly strain BZO 1D APC/YBCO interface [38, 58, 70]. T_c is expected to decrease sharply to around 60-65 K [71] due to the oxygen deficiency condition that reduces the pinning potential height, hence pinning efficiency of the BZO 1D APC (a schematic diagram is shown in Figure 31).

` The spacing between BHO 1D APCs is found to first decrease from ~30 nm to ~13 nm and then increase to ~16 nm when BHO concertation increases from 2.0 to 4.0, and to 6.0 vol.%. The accommodation field (H^*) that relates inversely to the spacing between the 1D APCs is estimated to be 2.3 T, 12.2 T, and 8.0 T, respectively (Table 3). H^* is correlated with an areal density of APCs, and high H^* is desired for high field application. It is assumed to be an optimal vortex pinning when H_{max} would be closed to the H^*. The H^* has been found to be proportional linearly to the impurity doping concentration [17, 63, 72], the H^* indeed increases linearly with the BZO doping in the range 2.0-6.0 vol.% as shown in Table 3.

Sample ID	T_c (K)	*C*-axis lattice constant (Å)	FWHM of YBCO (005) peak	D (nm)	d (nm)±1 (nm)	H^* (T)	Lattice mismatch with *c*-axis of YBCO
2 vol.% BZO/YBCO	89.27	11.82	0.35	5.2±0.5	20	5.0	
4 vol.% BZO/YBCO	87.48	11.71	0.34	5.8±0.6	15	9.2	7.1%
6 vol.% BZO/YBCO	86.90	11.67	0.27	5.9±0.9	12	14.3	
2 vol.% BHO/YBCO	88.85	11.77	0.42	4.6±0.5	30	2.3	
4 vol.% BHO/YBCO	85.84	11.77	0.51	4.8±0.4	13	12.2	6.7%
6 vol.% BHO/YBCO	78.50	11.78	0.49	5.1±0.7	16	8.0	

Table 3: A summary of the T_c, YBCO *c*-axis lattice constant, 1D APC diameters (D), 1D APC average spacing d (center-to-center) with uncertainty of 1 nm, accommodation field $H^*=\Phi_o/d^2$ for the 2.0-6.0 vol.% BZO 1D APC/YBCO and BHO 1D APC/YBCO nanocomposite films measured in this work. The reference YBCO *c*-axis lattice is 11.68 Å and its T_c is 90 K (not included in the table).

A peak of BHO 1D APC areal concentration n^*_{BHO} (and hence H^*) at 4.0 vol.% BHO doping indicates the threshold of the BHO doping concentration (4.0 vol.% in this study). The H^* of 12.2 T of the 4.0% BHO/YBCO in this study is much higher than the H^*~5.0 T reported for a 4.7 vol.% BHO/YBCO film [27]. Considering a higher doping range up to ~10 vol.% in the BZO/YBCO case [72], as compared to the 4.0 vol.% BHO/YBCO counterpart, the threshold value depends on the type of APCs materials and is the most probably due to the strain field distribution around the different types of APCs. It is explained in the elastic strain energy calculations [20] in which lattice mismatch, elastic constant, and interface strain are taken as the input parameters. The smaller linear n* vs. APC doping concentration range in the BHO/YBCO case implies a larger scale of strain field around an individual 1D APC, which prevents the formation of additional 1D APCs at above 4-5 vol.% based on this work and previous reports [24, 27, 58, 67]. Figure 33 depicts the HRTEM and fast Fourier filtered images (FFT) on 4.0 vol.% BZO/YBCO (Figures 33a, d), 4.0 vol.% BHO/YBCO (Figures 33b, e) and 6.0 vol.% BHO/YBCO (Figures 33c, f) nanocomposites respectively. To generate the FFT images, the area of interests is first selected in the TEM image and a fast Fourier transform (FFT) process of the area is conducted. By selecting and masking the specific diffraction dots in the FFT, the masked FFT is inverted to the fast Fourier filtered images as shown in Figures 33d-f. A major difference between the two cases is in the higher concentration of dislocations (white marks) at the BZO 1D APC/YBCO interface [17], which may be explained by the larger lattice mismatch (Table 3) and higher rigidity of BZO [13, 53]. A direct consequence of the high interfacial defect concentration is the strain

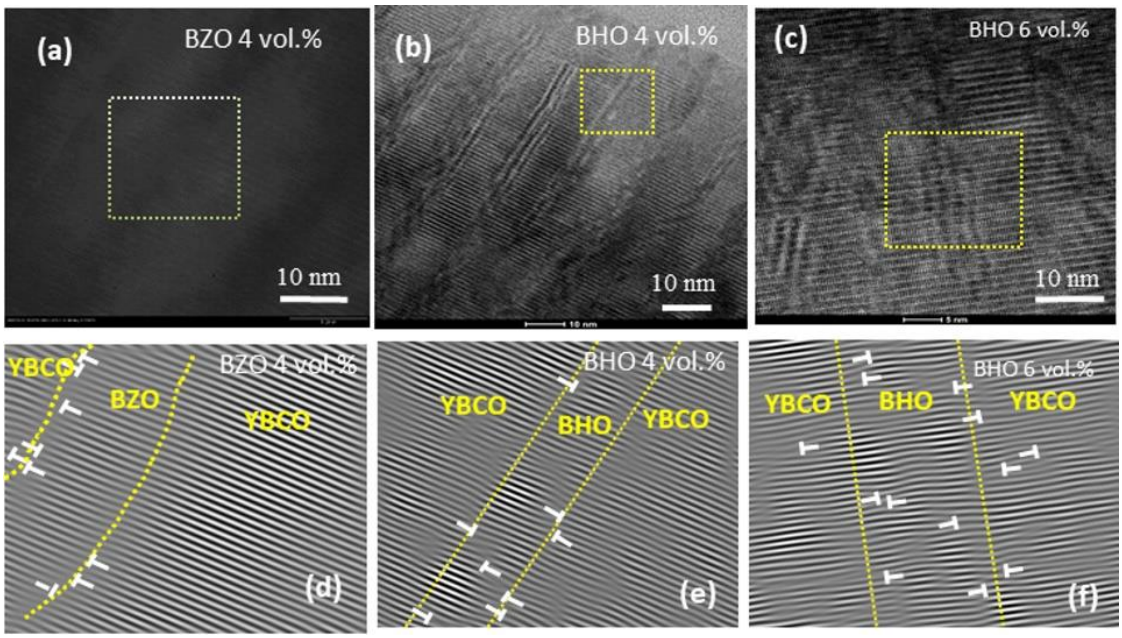

Figure 33: Cross sectional HRTEM images of YBCO nanocomposite thin films doped with (a) 4 vol.% BZO (b) 4 vol.% BHO (c) 6 vol.% BHO (top row), and (d), (e) and (f) are fast Fourier filtered images of marked area (rectangles) in (a), (b) and (c) respectively. Figures are adapted from Gautam et.al, APL, 2018 [39].

release in a short range of 1-2 nm from the interface [38]. The comparable *c*-axis lattice constant to that of undoped YBCO indicates much smaller *ab*-plane buckling in the YBCO matrix away from the interface (Figure 33 and Table 3). In contrast, the BHO/YBCO interface has a few randomly distributed dislocations otherwise coherent, and significant *ab*-plane buckling can be observed. This suggests that the strained BHO and YBCO lattices are adapting to each other and is maintained *c*-axis lattice constant ~11.77 Å-11.78 Å comparable for all BHO/YBCO films shown in Figure 33 and Table 3. Such high-density plane-buckling is confirmed by the stripped diffraction dots in the BHO/YBCO nanocomposite film. Interestingly, the similar microstructure in 6 vol.% BHO/YBCO nanocomposite film (Figure 33f) supports the argument of higher elastic adaptability and smaller lattice mismatch of BHO 1D APCs with YBCO. The coherent BHO 1D

APC/YBCO interface is due to the compromise of the strained lattices. Therefore, the difference in the BZO 1D APC/YBCO and BHO 1D APC/YBCO interface has a profound effect on the strain field distribution in the nanocomposite films, resulting in the different n* versus APC doping trends. Further investigation is required to understand the microscopic mechanism underlying the difficulties in doping higher concentration of BHO. It can be argued that Hf incorporation to YBCO lattice, especially when YBCO is under a higher lattice strain at a higher BHO doping that may prevent the formation of the BHO 1D APCs to the higher BHO doping concentration. This argument seems consistent with the significantly reduced T_c of the 6.0 vol.% BHO/YBCO nanocomposite films as compared to their counterparts of lower BHO doping and therefore J_c measured at temperatures close to T_c [27].

4.3 Crystallinity characterisation of nanocomposite films

Figures 34a-f show the XRD θ-2θ scan of 2.0-6.0 vol.% BZO (or BHO)/YBCO nanocomposite films. This illustrates the high-quality crystallinity with *c*-axis orientation along the normal direction of the film by the presence of the YBCO (00l) peaks. The presence of the BZO (00l) peaks are indexed as an asterisk (*). The background hump around 20-25 degrees and 40-45 degrees could be from the amorphous glass slide used as the sample holder. Some other peaks ~20 and 40 degrees is indexed as Y_2O_3 and YBa_2ZrO_6 (YBZO) because Zr can be induced to YBCO lattice [73]. The lattice mismatch of 6.7% between BHO and YBCO is considerably smaller than 7.1% between BZO and YBCO, and more adaptive behavior of BHO with YBCO [13, 53], lead to the different trends of the *c*-axis lattice constants at different APC doping. The decreasing

lattice constant of BZO from 11.82 Å at 2 vol.% BZO to 11.67 Å at 6 vol.% BZO (Table 3) is due to the defective BZO/YBCO interface. This results in the strain relief and the *c*-axis lattice constant

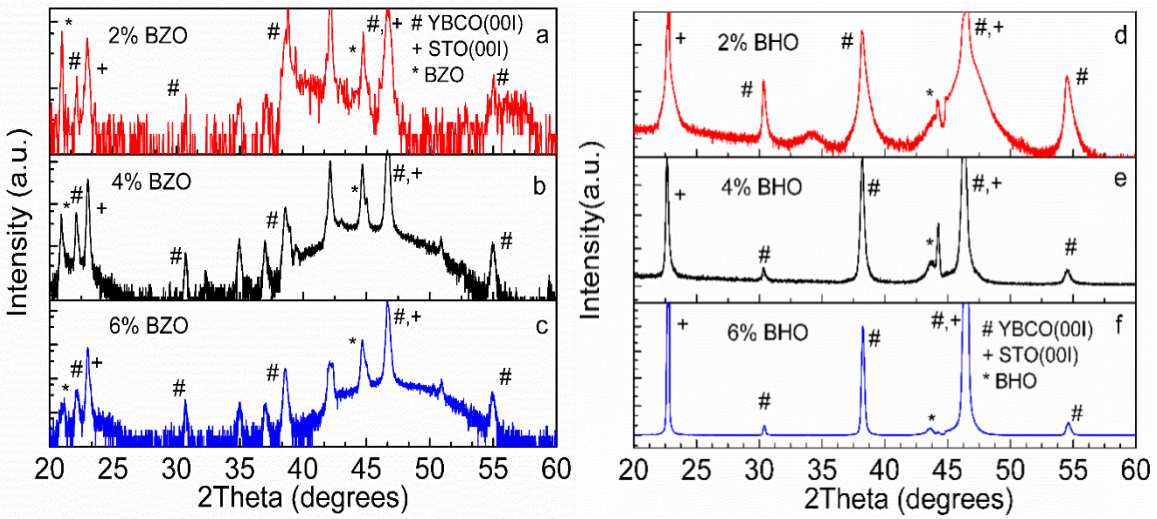

Figure 34: Left: (a)-(c) XRD θ-2θ spectra for the 2 vol.%, 4 vol.% and 6 vol.% BZO/YBCO nanocomposite thin films, and right: (d)-(f) 2 vol.%, 4 vol.% and 6 vol.% BHO/YBCO nanocomposite thin films on STO substrates.

approaches to the undoped YBCO at ~11.68 Å [15, 38, 70]. This argument is consistent with the decreasing trend of full width at half maximum (FWHM) of the YBCO (005) peak with the increasing BZO concentration. The FWHM values are summarized in Table 3. This means at BZO 1D APC/YBCO interface strain doesn't extend to the long range as the strain is released through the interfacial dislocations.

The *c*-axis lattice constant of the YBCO in the BHO/YBCO nanocomposite films remains almost a constant of 11.77 Å to11.78 Å as the BHO doping is varied from 2 vol.% to 6 vol.%. It suggests that a coherent BHO 1D APC/YBCO interface is maintained in the entire BHO doping range through a mutual accommodation of the BHO/ YBCO lattices [39]. The smaller elongation of the YBCO *c*-axis lattice constant to 11.77-11.78 Å as compared to the 11.82 Å in the 2 vol.%

BZO/YBCO nanocomposite could be the difference of lattice mismatch of two doping materials. The unchanged expanded *c*-axis, together with comparatively similar YBCO (005) FWHM of 0.42, 0.51, and 0.49 for the 2%, 4% and 6 vol.% BHO/YBCO nanocomposite films, respectively, is an indication of maintained APC/YBCO interface coherency at different BHO doping levels. This observation is important and reveals a fundamental difference between the BHO 1D APC/YBCO and BZO 1D APC/YBCO interfaces, which affects the pinning efficiency of 1D APCs.

4.4 Critical current density $J_c(H)$ and pinning force density $F_p(H)$ and angular dependence $J_c(\theta)$

One could set the hypothesis that with comparable morphology and dimension of BZO (or BHO)1D APCs are expected to have a comparable pinning efficiency, the transport $J_c(H)$ measurement confirms this is certainly not the case. The difference in pinning efficiency could be because of the difference in 1D APC/YBCO interface. Figure 35 compares the $J_c(H)$ and $F_p(H)$ curves measured on 2.0-6.0 vol.% BZO/YBCO (black) and 2.0- 4.0 vol.% BHO/YBCO (red) films at $H//c$-axis ($\theta=0^o$) at 77 K (Figures 35a and 35c) and 65 K (Figures 35b and 35d) respectively. The $J_c(H)$ curve for undoped YBCO film (blue) is also included as a reference. The smaller susceptibility of $J_c(H)$ of BZO (BHO)/YBCO nanocomposite films to the applied magnetic field (H) especially in the higher field range compared to reference YBCO film is anticipated from the improved pinning by the 1D APCs in doped YBCO nanocomposite films. At 77 K, considerably

the lower α-values in the range of 0.23-0.30 for almost all nanocomposite films than that of typical α~0.5 for undoped YBCO film (Figure 35a), confirms the strong correlated pinning by BZO and

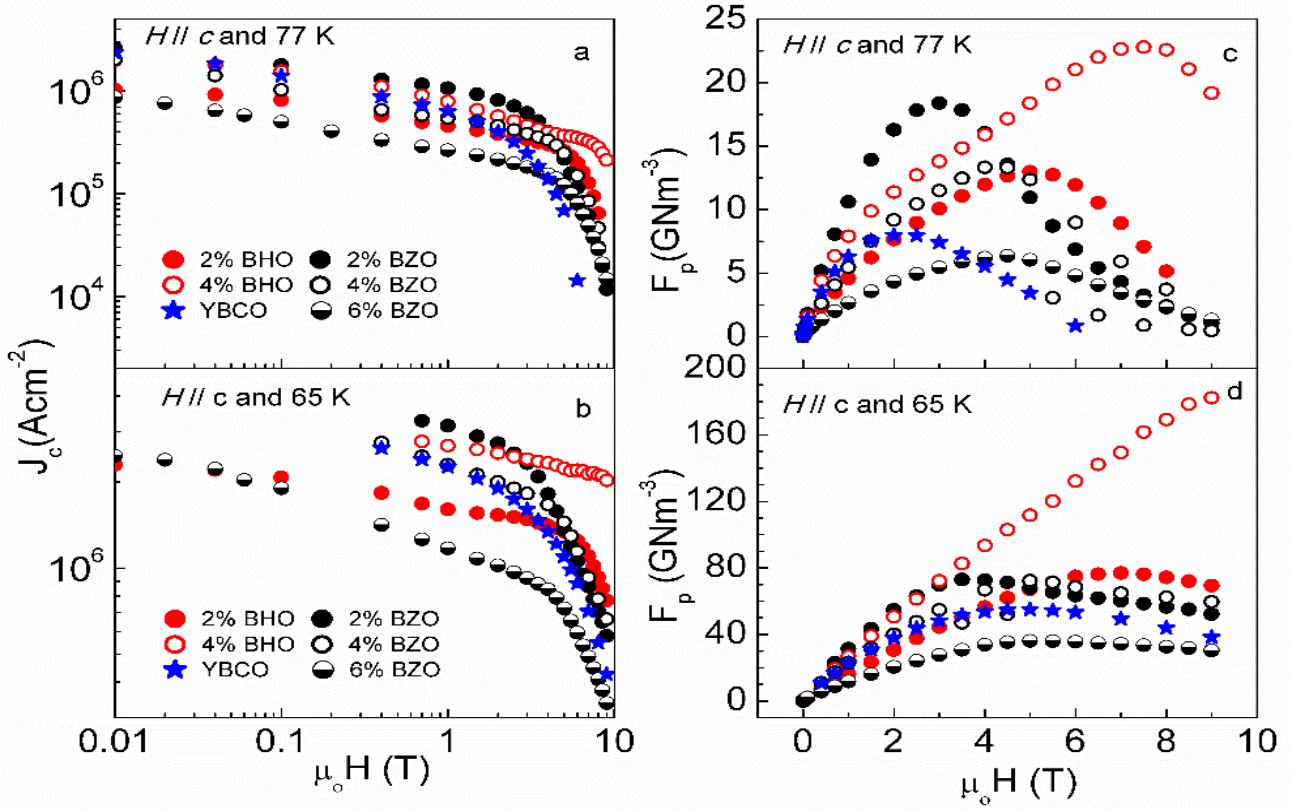

Figure 35: $J_c(H)$ and F_p(H) curves measured on reference YBCO (blue), and BZO 1D APC/YBCO (black) and BHO 1D-APC/YBCO (red) nanocomposite films at θ ~0^o (*H//c*-axis) at 77 K (a) and (c); and (b) and (d) at 65 K respectively. Symbols are 2 vol. % (solid), 4 vol.% (open), 6 vol.% (half-filled) in all figures. These Figures are adapted from Gautam et.al, APL, 2018 [39].

BHO 1D APCs. At 65 K, (neglecting T_c effect), α values are significantly lower ~0.10-0.11 for 2-4% BHO/YBCO films as compared to α values of 0.17-0.21 for 2.0-6.0% BZO/YBCO films and ~ 0.25 for reference YBCO film (Table 4) suggest a higher pinning efficiency of the BHO 1D APCs than their BZO counterparts and undoped YBCO films.

The J_c (H) curve decreases monotonically with the BZO doping in the most field range is opposite to the J_c (H) curves of BHO doping at which the J_c (H) curves peaks at 4 vol.% BHO doping at both 77 K and 65 K (Figures 35a and 35b). The J_c (H) curves for 6 vol.% BHO/YBCO nanocomposite film are not included because of the significantly low J_c values including two orders of magnitude lower J_c value ~6×10^4 MA/cm^2 at self-field and at 65 K in this study. Overall higher performance is observed in the lower BZO doped films except for a crossover of J_c (H) curves for the 2.0 and 4.0 vol.% BZO/YBCO films occur at 4.5 T at 77 K. This reflects on the highest F_p (H) curve for the 2.0 vol.% BZO/YBCO film at both 77 K and 65 K (Figures 35c and 35d). A similar decreasing trend of the F_p (H) curves with increasing the BZO doping, which is consistent with the previous report [72]. A significantly higher F_p (H) for 2.0 and 4.0 vol.% BZO/YBCO films with the maximum F_p ($F_{p,max}$) in 2.0 vol.% BZO/YBCO film is 18.4 and 73.1 GN/m^3 at 77 K and 65 K respectively, higher than $F_{p,max}$ ~8.0 GN/m^3 and 55.0 GN/m^3 of undoped YBCO at the same temperature is a consequence of the presence of the 1D APCs in the former. While the $F_{p,max}$ for the 6.0 vol.% BZO/YBCO film is comparable or lower than that of the reference YBCO (Table 4). The $F_{p,max}$ ~13.3 GN/m^3 and 72.4 GN/m^3, for 4 % BZO/YBCO is also consistent with the reported result for the comparable BZO doping [27]. As shown in Figure 31, lower T_{c2} the smaller column is primarily attributed to the defects/disorders, especially oxygen deficiencies, result in the smaller pinning well height (red) and hence the pinning efficiency of the BZO 1D APC would be much reduced. On the other hand, this inner column will not be present

around the BHO 1D APC with a coherent interface with YBCO, resulting in higher pinning well height (black) and therefore higher pinning efficiency by BHO 1D APCs.

Sample ID	$F_{p,max}$ (H//c-axis) (GN/m^3)		H_{max} (H//c-axis) (T)		H_{max} /H*		Alpha (α) values at H//c-axis	
	77 K	65 K	77 K	65 K	77 K	65 K	77 K	65 K
Un doped YBCO	08.0	54.8	2.0	5.0	NA	NA	0.49	0.24
2 vol.% BZO/YBCO	18.4	73.1	3.0	3.5	0.60	0.70	0.23	0.17
4 vol.% BZO/YBCO	13.3	72.4	4.0	5.0	0.43	0.54	0.27	0.20
6 vol.% BZO/YBCO	06.4	36.1	4.5	5.0	0.31	0.35	0.28	0.21
2 vol.% BHO/YBCO	11.8	76.9	5.0	7.0	2.50	3.50	0.25	0.11
4 vol.% BHO/YBCO	22.8	182.0	7.5	>9.0	0.61	0.74$^{\uparrow}$	0.29	0.10

Table 4: A summary of pinning properties extracted from the transport measurement including $F_{p,max}$, H_{max}, H_{max} /H*, and alpha (α) values at 77 K and 65 K, for the 2-6 vol.% BZO/YBCO and 2-4 vol.% BHO/YBCO nanocomposite films, in comparison with the reference YBCO film. Symbol ($^{\uparrow}$) intdicates the value could go up but the instrument limitation applies to this value.

Interestingly increasing J_c (H) and F_p (H) for BHO/YBCO nanocomposite to moderate BHO doping of 4 vol.%, followed with a dramatic decrease in both at 6 vol.% (Figure 35) is also reported in [10, 27] except a significantly lower J_c (H) for 6 vol.% BHO/YBCO nanocomposite in this study. It is possibly due to the severe deformation of the YBCO lattice as evidenced in the significant T_c decreases to 78.5 K by maintaining the coherent BHO 1DAPC/YBCO interface to 6 vol.% BHO/YBCO, or simply in 6 vol.% BHO/REBCO thin films [28]. The $F_{p,max}$ of ~22.8 and > 182 GN/m^3 for the 4 vol.% BHO/YBCO film at 77 K and 65 K respectively are considerably higher than the best reported on BZO/YBCO nanocomposite films and the reference YBCO film as well. At 65 K, the $F_{p,max}$ of >182 GN/m^3 for the 4 vol.% BHO/YBCO film is about 2.5 times higher than the best $F_{p,max}$ of 73-74 GN/m^3 for the BZO/YBCO nanocomposite films reported in

this work and by others [72]. This is the best $F_{p,max}$ reported so far at 65 K, and is about 1.5 times, 1.8 times and 1.5 times higher, respectively, than the highest claimed $F_{p,max}$ ~120 GN/m^3 for BHO/REBCO, $F_{p,max}$~103 GN/m^3 for BSO/YBCO [65, 74], and $F_{p,max}$ ~122 GN/m^3 for double perovskites (5.0 mol.% BaNbOy plus 5.0 mol% Y_2O_3)/YBCO nanocomposite films [75].

To gain further insights on the difference in the F_p (H) behaviors of the two sets of the films, H_{max} (at which the $F_{p,max}$ is observed) values are compared with H^* (Table 3). The H_{max} values of 3.0-3.5 T, 4.0-5.0 T and 4.5-5.0 T at 2.0, 4.0, and 6.0 vol.% BZO doping, are considerably lower than the H^* values of 5.0, 9.2, and 14.3 T. This suggests that a significant portion of the BZO 1D APCs are not efficient pins. The trend in the BHO/YBCO case seems opposite and these H_{max} values are considerably higher than their BZO/YBCO counterparts (Table 3). For the 2 vol.% BHO/YBCO film, the H_{max} of 5.0-7.0 T at 77-65 K is more than twice of the H^* ~2.3 T. At 4 vol.% BHO doping, the H_{max} >9.0 T (instrument limit) seems consistent to the projected H^* of 12.2 T. Quantitatively, the H_{max}/H^* value closer to one indicates the anticipated pinning efficiency assuming each APC pin a vortex. Specifically, the H_{max}/H^* value of BZO 1D APCs is about 0.6-0.7, 0.43-0.54 and 0.31-0.35, respectively, for 2 vol.%-6 vol.% BZO/YBCO films at T~ 65-77 K indicates H_{max} doesn't increase at the same rate as H^* which with increasing BZO APC doping. In contrast, the H_{max}/H^* values are significantly higher in the BHO/YBCO films. For example, at 2 vol.% BHO, it is 2.5-3.5 and at 4 vol.% BHO, it reduces to 0.61 - >0.74. The high H_{max}/H^* in exceeding 1 suggests a BHO 1D APC could pin multiple vortices on the vortex lattice on which

an elastic interaction is present between vortices [76]. These results support the higher pinning efficiency of BHO 1D APCs than their BZO counterparts.

Figures 36a-d compare the J_c (θ) curves measured on the undoped YBCO (blue), a reference film, 4.0 vol.% BZO/YBCO (black) and 4.0 vol.% BHO/YBCO (red) nanocomposite films at the 1.0 T (Figure 36a) and 3.0 T (Figure 36b) at 77 K, and 5.0 T (Figure 36c) 9.0 T (Figure 36d) at 65 K, respectively.

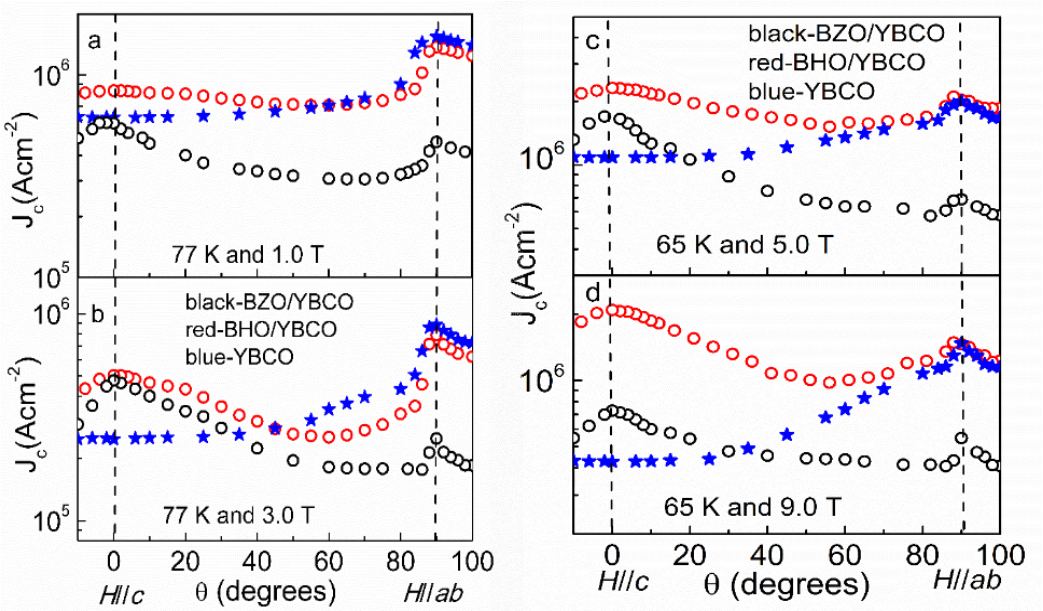

Figure 36: Angular dependence of J_c measured on 4.0 vol. % BZO (black open) and 4.0 vol.% BHO (red open) doped YBCO (BZO/YBCO, and BHO/YBCO) and undoped YBCO film (blue star) nanocomposite films (a)-(b) 1.0 T and 3.0 T at 77 K, (c)-(d) 5.0 T , and 9.0 T at 65 K respectively. Symbols follow the same for all figures. These Figures are adapted from Gautam et.el, APL, 2018 [39].

The large J_c peak at *H*//ab-plane (90°) for YBCO film is attributed to the strong intrinsic pinning by layered structure. Interestingly, almost the same J_c peak at *H*//*ab*-plane for BHO/YBCO is an indication of nearly unaffected intrinsic pinning, in contrast to the significantly suppressed of such

pinning in the BZO/YBCO one. This indicates the long-range buckling of the *ab*-planes in the BHO/YBCO nanocomposite due to the coherent BHO/YBCO interface maintains the effective pinning of vortices as in the undoped YBCO [39]. The J_c peaks at $H//c$-axis ($\theta=0^o$) for the nanocomposite films are attributed to correlated pinning by the *c*-axis aligned 1D APCs in nanocomposite film which is absent in undoped YBCO film. While these peaks are comparable at 77 K for the two films, they differ considerably at 65 K. A significantly higher J_c peaks values at $H//c$-axis are observed on the BHO/YBCO film at 65 K both at 5.0 T and 9.0 T. The higher J_c-peak at $H//c$-axis, in combination with the higher J_c-peak at $H//ab$-plane also lead to an overall higher J_c (θ) for the BHO/YBCO nanocomposite film as compared to the reference undoped YBCO and BZO/YBCO nanocomposite film at field of 5-9 T.

4.5 Conclusions

The work in this chapter investigates the nanostructure morphology and transport J_c in 2.0-6.0 vol.% BZO/YBCO and 2.0-4.0 vol.% BHO/YBCO nanocomposite thin films. It probes the correlation between the 1D APC/YBCO interface and the pinning efficiency of the 1D APCs. Several interesting insights have been listed as follows:

A highly coherent BHO 1DAPC/YBCO interface is a significance of the low rigidity of the BHO 1D APCs and their smaller lattice mismatch with YBCO. A semicoherent BZO 1D APC/YBCO is due to the less adaptive BZO lattice to YBCO and comparatively higher lattice mismatch with YBCO. This results in the interfacial defects and hence release the strain.

The 1D APC/YBCO interface directly affects the strain field distribution around the 1D APC in the nanocomposite films, which in turn affects the linear range of the areal density of n^*_{BHO} and n^*_{BZO} (and hence H^*) with APC concentration. A highly strained lattice prevents a linear increase of BHO 1D APCs with BHO concentration beyond the threshold concentration in contrast to short-range strained lattice due to the defective semicoherent interface that allows a linear increase of BZO 1D APCs with the BZO concentration greater than 6.0 vol.%.

The 1D APC/YBCO interface has a critical effect on their pinning efficiency as illustrated in the higher $F_{p,max}$ and H_{max}/H^* ratio. Even with the comparable diameter of 1D APCs, a coherent BHO 1D APC/YBCO interface have significantly higher pinning efficiency than that of semi-coherent BZO 1D APC/YBCO interface. A record high value of $F_{p,max}$ ~182 GN/m^3 is calculated in the BHO/YBCO interface compared to $F_{p,max}$ ~72 GN/m^3 in the BZO/YBCO interface. In addition, the low H_{max}/H^* ratio <1, for BZO/YBCO nanocomposite films indicate that a significant number of 1D APCs provides inefficient pinning. The significant degradation of the superconductivity in the defective BZO 1D APC/YBCO interface reveals the critical importance of a high quality 1D APC/REBCO interface maintaining coherent 1D APC/YBCO interface in achieving high pinning efficiency.

Chapter 5 Probing the Pinning Efficiency of 1D APCs in BZO+YBCO/$Ca_{0.3}Y_{0.7}Ba_2Cu_3O_{7-x}$ Multilayer Films

Chapter 4 discussed the pinning efficiency of the comparable diameter of BZO and BHO doping material that can generate *c*-axis aligned 1D APCs. The former has the semicoherent 1D APC/YBCO interface compared to the latter, which form the highly coherent 1D APC/YBCO interface. A microstructure analysis also revealed an oxygen-deficient center and hence highly defective YBCO cylindrical shell of 1-2 nm in thickness around the BZO 1D APCs. A significant reduction of pinning efficiency in BZO/YBCO film could be a defective interface due to the reduction T_c and thus the pinning potential height in the YBCO column [39]. Quantitatively, the pinning potential height is optimal if the T_c of the YBCO column around a 1D APC is not degraded. Schmehl, A. et al., reported that T_c could go as low as ~ 60 K [38, 77], at the defective interface of the thickness~1-2 nm cylindrical shell from 1D APC/YBCO matrix. An immediate solution to reinstate the pinning efficiency of the BZO 1D APC is to repair the oxygen deficiency disorders at the APC/YBCO interface.

This chapter explores the calcium (Ca) doping of the YBCO column around the BZO 1D APCs using insertion of $Ca_{0.3}Y_{0.7}Ba_2Cu_3O_{7-x}$ (CaY-123) spacer layers of 5-15 nm in thickness into BZO 1D APC/YBCO nanocomposite films in the multilayer form. The CaY-123 spacer layer facilitates the Ca-diffusion into the BZO 1D APC/YBCO interface to reduce the oxygen deficiency. Therefore, it enhances the pinning efficiency of the BZO 1D APCs in a similar way to

Ca-doping assisted repairing of the large-angle grain boundaries (GBs) in YBCO films [77-80]. Ca cation has valance of +2, and the Ca-replacement of Y cations of valance "+3" has shown to lead the hole over-doping of YBCO with a lower T_c [81]. While oxygen deficiency disorders at the BZO 1D APC/YBCO interface may differ from that at large-angle GBs, we hypothesize that atomic scale Ca-induced interface may effectively correct the detrimental effect of the disorders in a similar manner to the GB case and therefore enhance the pinning efficiency of BZO 1D APCs through correction of the built-in electric potential across the interfaces [77, 79, 81, 82].

To confirm this hypothesis, this work investigates 6 vol.% BZO/YBCO nanocomposite films of the total thickness of 160-170 nm with two CaY-123 spacer layers of thicknesses of 10 nm. In comparison with the reference 6 vol.% BZO/YBCO nanocomposite film without the spacer layers, remarkably enhanced J_c (H) at high magnetic fields in exceeding 1-3 T is obtained in samples with the CaY-123 spacer layers. At 9.0 T, a five-fold enhancement of the J_c is obtained, which can be attributed to the enhanced pinning efficiency of the BZO 1D APCs as illustrated in both enhanced F_p and H_{max}. In the following section, we present the experimental transport results together with nanostructure morphology.

5.1 Calcium diffusion and superconducting properties

Figure 37 illustrates the cross-sectional view of the 6 vol.% BZO/YBCO multilayer (ML) nanocomposite with two CaY-123 spacer layers. Calcium (Ca) can diffuse through the interface between BZO 1D APCs (vertical black lines) and YBCO matrix shown by the arrows as well as directly into YBCO. While the former is desired, the latter is not since it may reduce the T_c of the

YBCO matrix and hence the BZO/YBCO nanocomposite. Considering the T_c of the CaY-123 is 82 K [79, 83], extensive Ca-diffusion into YBCO matrix could limit the applications to temperatures much below 77 K. It is, therefore, important to identify the sample fabrication window for optimal interface modification with minimal degradation of the T_c of the YBCO matrix. In addition to exploring PLD repetition rates (RR) of 1, 2, and 4 Hz for the control of the effective Ca-diffusion time, the thickness of the $Ca_{0.3}Y_{0.7}Ba_2Cu_3O_{7-x}$ spacer layer (purple) was also varied in the range of 5-15 nm. When changing one parameter, the other is kept constant. Controlling the local gradient of the Ca content, Ca content maintains the amount of the Ca diffusion into BZO 1D APC/YBCO interface.

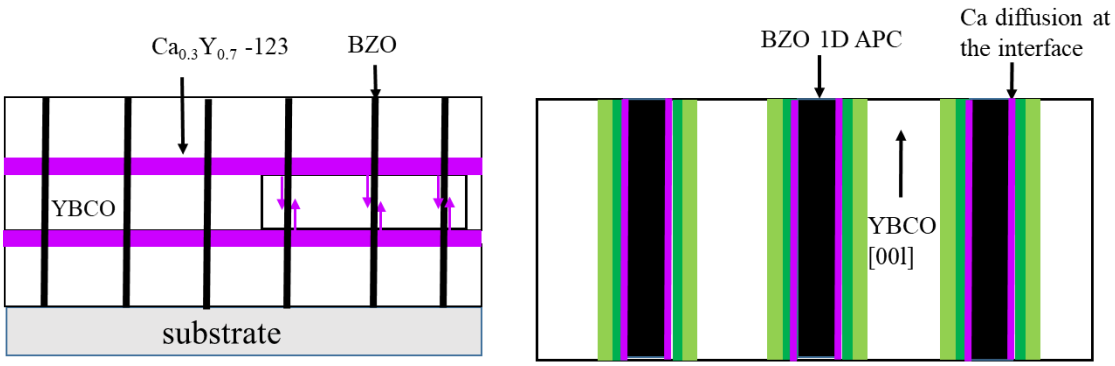

Figure 37: Schematic of the BZO + YBCO and $Ca_{0.3}Y_{0.7}Ba_2Cu_3O_{7-x}$ multilayers showing Ca diffusion zone (purple arrows) of the APC/YBCO interface at left, zoom in view from the rectangular part of the left figure of the BZO 1D-APC and YBCO interface showing Ca diffusion atomic layer (purple line) at right. Color codes from dark green at the interface of BZO 1D APCs to yellow toward the boundary of YBCO indicates the decreasing strain as it moves away from the BZO toward the YBCO interface.

To understand the intrinsic properties of the Ca-induced ML nanocomposite films, we have calculated the resistivity of the films and have determined the critical temperature T_c from measured resistance versus temperature (R-T) curves. Figure 38 illustrates the resistivity vs.

temperature curves of ML films at which T_c is increased from 83.5 K to 85 K with increasing laser repetition rate (RR). The T_c~85 K is found to be constant for the nanocomposite thin films varying CaY-123 spacer layer thickness of 5-15 nm but fixed RR of 4 Hz (Figure is not shown here). In those films, increasing RR maintains the high crystallinity of the film and hence T_c is increased.

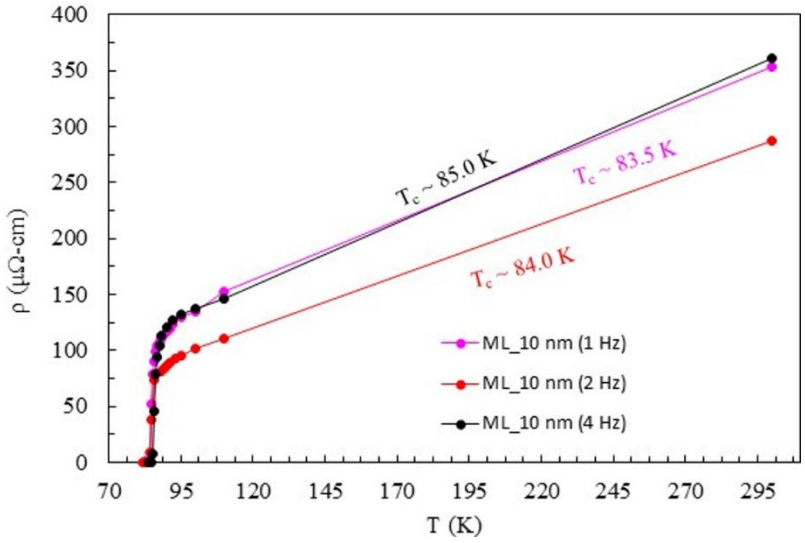

Figure 38: Resistivity vs. temperature graph of multilayer films of the fixed thickness approximately 10 nm of the CaY-123 spacer layer but varying laser repetition rate of 1, 2 and 4 Hz at parenthesis.

The resistivity of the undoped YBCO is about 150 μΩ-cm at 300 K and increases with increasing doping concentration, typically approximately 50 μΩ-cm per 2.0 vol.% of BZO concentration. The calculated resistivity of all ML films with fixed CaY-123 spacer layer varying laser RR ranges from 280-360 μΩ-cm, which suggests ML nanocomposites maintain the superconducting properties. Similarly, resistivity of other set of ML nanocomposite thin films with variable thickness of CaY-123 of 5-15 nm ranges from 260-340 μΩ-cm at 300 K. A slightly lower resistivity in 2 Hz RR nanocomposite thin film could be the well-maintained high crystallinity of

the films with a threshold of calcium diffusion at the interface with the given thickness of CaY-123 spacer layer.

Typically, the ratio of $\rho_{300\ K}/\rho_{100\ K}$ for a good nanocomposite film is expected to be 3, considering the proportionality relation of resistance vs. temperature. The ratio of the resistivity at 300 K and 100 K ($\rho_{300\ K}/\rho_{100\ K}$) of the ML nanocomposite of fixed CaY-123 thickness of 10 nm with variable RR samples ranges from 2.61-2.82. The best ratio is 2.82 for ML with CaY-123 layer of thickness of 10 nm and of RR~2 Hz, which is about 6.4% less than the typical value of 3. Similarly, the ratio ($\rho_{300\ K}/\rho_{100\ K}$) of the ML nanocomposite of fixed RR of 4 Hz and variable CaY-123 thickness of 5-15 nm ranges from 2.65-2.86, with a higher value for ML film with CaY-123 thickness of 5 nm. This value is just 4.9% less than the typical value. This information indicates that ML samples are of good quality and maintain desired intrinsic properties such as T_c and resistivity of superconductors.

5.2 Nanostructure morphology

Figures 39a-b compare the cross-sectional view of Transmission Electron Microscopy (TEM) images of the single layer (SL) and multilayer (ML) nanocomposite film with BZO/YBCO thickness of 50 nm and CaY-123 spacers layer thickness of 10 nm deposited at 2.0 Hz of repetition rate, while Figures 39c-d compare the elemental mapping of corresponding films. *C*-axis aligned 1D APCs along the thickness of the film can be observed in both films. The only difference is the appearance of the two small horizontal stripes in Figure 39b, which illustrates the presence of the CaY-123 spacer layer in ML film. It is further verified by the two purple horizontal lines, rich in

Ca, in Figure 39d, which are absent in SL film (Figure 39c). Interestingly, spreading of the Ca element near the 1D APCs in Figure 39d supports the hypothesis of diffusion of Ca at the APC/YBCO interface. However, the distribution of calcium is limited to the very narrow column, which is an indication of less Ca diffusion in the YBCO matrix. With the elemental mapping, it is clear that a significant amount of Ca remains in the spacer layer without diffusion at the interface.

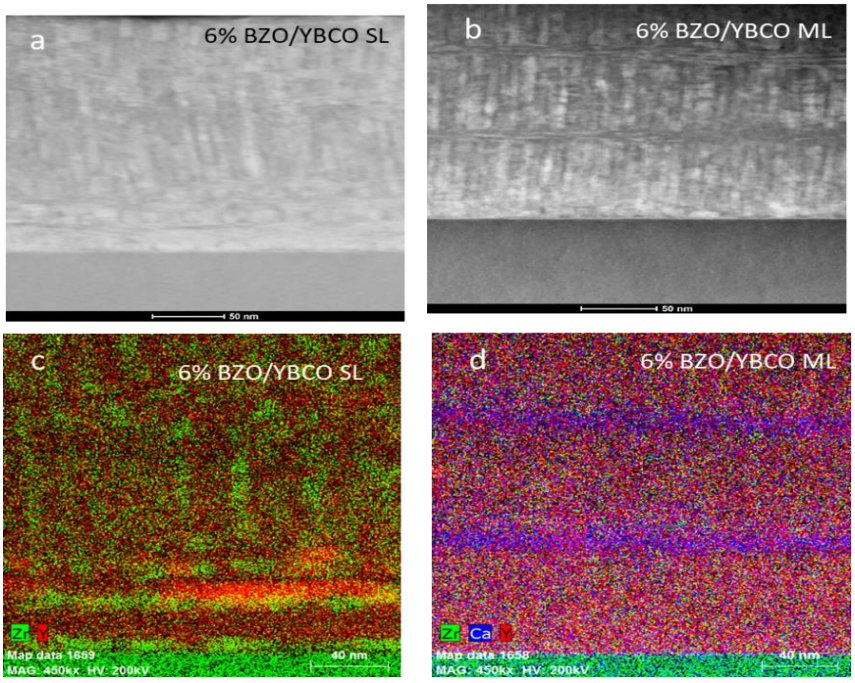

Figure 39: (a)-(b) TEM confirmation of the same or comparable BZO APC morphology, diameter, and concentration of 6% BZO/YBCO nanocomposite SL and ML 50 nm/10 nm-2 Hz films; (c)-(d) elemental mapping of Calcium and Oxygen across the BZO/YBCO interface in those films.

This indicates possibly smaller thickness (<10 nm) of the Ca-spacer layer would be good enough for a diffusion process. This is also reflected in the J_c and F_p value of the smaller Ca-spacer layer thickness nanocomposite film (details appear in the following discussion).

It is also important to note that due to CaY-123 layer, 1D APC appeared to be segmented in ML films. The segmented 1D APCs as reported in multilayer film deposited with BZO/YBCO and YBCO alternating layers pin the vortices through the kinking of vortices [51, 84]. The lateral dimension of 1D APCs is approximately ~5-6 nm in both films, while average inter 1D APCs distance measures about ~12 nm with the uncertainty of 1 nm. Typically, 60-80 images are taken in cross-sectional TEM in different areas of a nanocomposite film to determine the average spacing using professional software on TEM systems. The accommodation field $H^*(=\Phi_o/d^2)$ is thus calculated as 14.3 T. The Φ_o is the flux quantum (~2.07×10^{-15} Wb) and d is the inter 1D APC distance. The estimation of the n* assumes a square lattice (for convenience) for 1D APCs since the distribution of the 1D APCs is random.

5.3 Electrical transport properties $J_c(H)$ and $F_p(H)$ for ML nanocomposite films

Figures 40a and b compare the $J_c(H)$ curves of five thin films at 77 K and 65 K respectively. Three of them are ML nanocomposite films with fixed BZO/YBCO layer thickness of 50 nm and Ca-Y123 spacer layer thickness of 10 nm but varying laser repetition rate. They are named ML_10 nm (1 Hz) (purple), ML_10 nm (2 Hz) (red), and ML_10 nm (4 Hz) (light green), respectively. Two reference samples are also included, YBCO (blue) and 6 vol.% BZO 1D-APC/YBCO without any $Ca_{0.3}Y_{0.7}Ba_2Cu_3O_{7-x}$ spacer layers (black); they are considered SL in rest of the part of this chapter when fabricated at their optimal deposition parameters [49, 54, 85]. At 77 K, the four nanocomposites except the SL have their self-field J_c in exceeding 1.0 MA/cm^2, which is

consistent to the reported results for the high quality YBCO samples in literature [21, 86]. The slightly lower self-field J_c in SL (black) is also common due to the strain field at 6 vol.% BZO doping that typically reduces T_c of the BZO/YBCO nanocomposite film monotonically with increasing BZO concentration. For this specific sample, the T_c is 86.9 K (Table 5). Interestingly, this T_c value is at least 1.9 K higher than the T_c values of its counterparts with $Ca_{0.3}Y_{0.7}Ba_2Cu_3O_{7-x}$ spacer layers as shown in Table 5. This means the differences in the J_c (H) curves of BZO/YBCO nanocomposites shown in Figure 40 is unlikely a T_c effect.

All ML nanocomposites, despite lower T_c as expected from slight Ca-doping, have higher J_c (H) than their SL counterpart at both at 77 K and 65 K for the entire range of the field up to 9.0 T (Figures 40a and b). This means an enhanced pinning efficiency of BZO 1D APCs in the ML nanocomposite films compared to SL film. Such enhanced pinning efficiency could be due to the coherent interface of 1D APC/YBCO by lowering the oxygen deficient defective region through Ca diffusion as reported in BHO/YBCO nanocomposite films [39]. In addition, the J_c (H) enhancement with the applied magnetic field (H) in ML nanocomposite indicates the high areal density of efficient 1D APCs. It could be due to Ca mediated interface contribution to the pinning at higher magnetic fields. Remarkably, five times higher J_c at 9.0 T can be observed when comparing the ML_10 nm (2 Hz) (red, optimal among the three ML nanocomposites) and SL (black) nanocomposites at both 77 K and 65 K. Quantitatively, the lower α-values of SL and ML nanocomposites (Table 5) compared to undoped YBCO indicates the strong pinning in the SL and

ML films due to the presence of APCs. In addition, a comparatively lower alpha value for ML nanocomposites compared to SL film is indicative of strong pinning by BZO APCs in ML films.

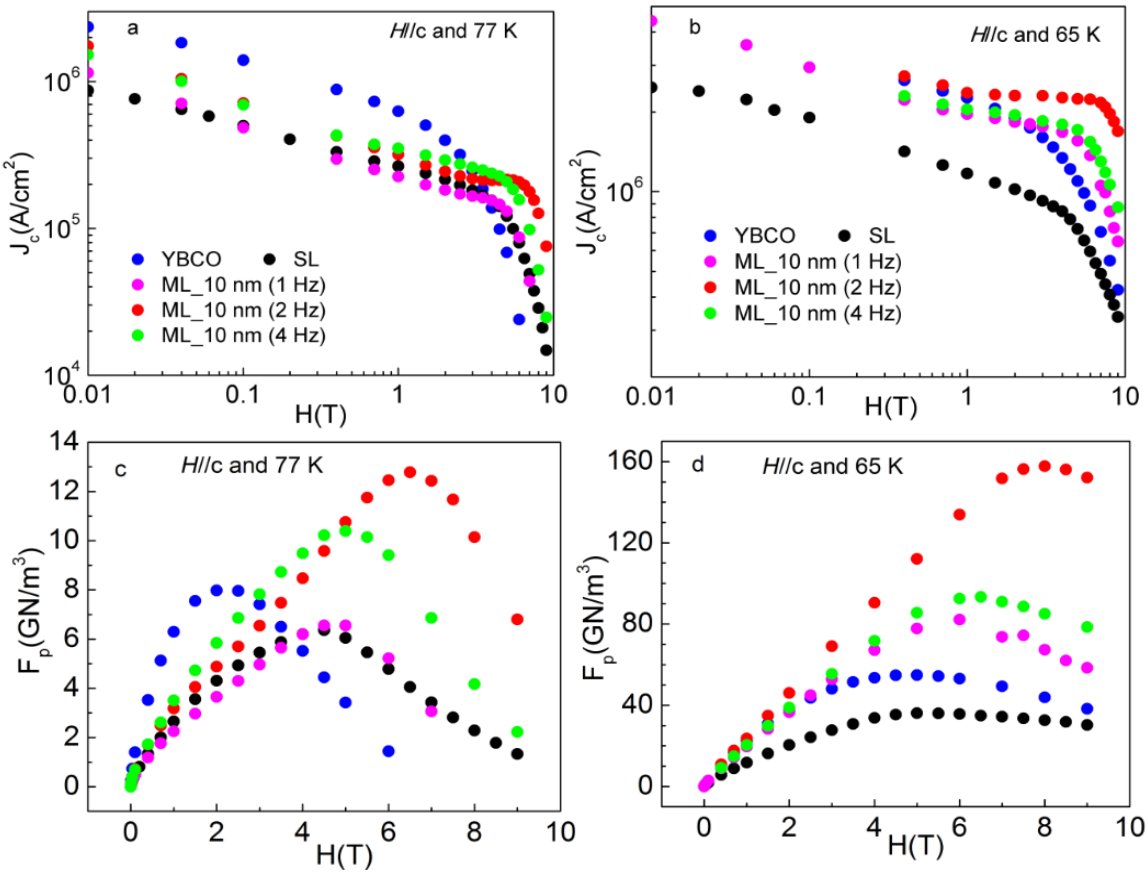

Figure 40: J_c vs. H and F_p vs. H curves measured on undoped YBCO (dark blue), 6 vol.% BZO/YBCO named as SL (black) and multilayer samples: ML_10 nm-1 Hz (purple), ML_10 nm-2 Hz (red) and ML_10 nm-4 Hz (light green) at H//c-axis ($\theta = 0^o$) and at 77 K and 65 K. Color codes follow the same for all figures.

The lower alpha value of ML films could be due to the improved 1D APC/YBCO interface by calcium diffusion; otherwise, the dimension and density are comparable.

The enhanced pinning efficiency of individual BZO 1D APCs and the concentration of the activated strong BZO 1D APCs are further illustrated in the F_p (H) curves (Figures 40c and d)

Sample ID	T_c (K)	$F_{p,max}$ (H//c-axis)		H_{max} (H//c-axis)		Alpha (α) values at H//c-axis	
		77 K	65 K	77 K	65 K	77 K	65 K
6% BZO/YBCO	86.9	6.36	36.14	4.5	5.0	0.28	0.21
6% BZO ML50 nm/10 nm-1 Hz	83.5	6.55	82.20	4.5	6.0	0.31	0.18
6% BZO ML50 nm/10 nm-2 Hz	84.0	12.77	157.70	6.5	8.0	0.34	0.14
6% BZO ML50 nm/10 nm-4 Hz	85.0	10.40	93.35	5.0	6.5	0.29	0.13
6% BZO ML50 nm/15 nm-4 Hz	85.0	10.15	100.39	5.0	6.0	0.27	0.24
6% BZO ML50 nm/5 nm-4 Hz	85.0	16.55	144.34	5.0	6.5	0.26	0.12

Table 5: Summary of the some of the important parameters such as critical temperature (T_c), $F_{p,max}$, H_{max}, and alpha values of 6 vol.% BZO/YBCO, and multilayer films of 10 nm the CaY-123 thicknesses and 1, 2, and 4 Hz the laser repetition rate (RR) of Pulse Laser Deposition (PLD) system. At 65 K, alpha values of ML films are calculated in the different field range of 0.4 T to few Teslas depending on the linear region.

through higher $F_{p,max}$ and H_{max} values in ML_10 nm (2 Hz) (red, optimal among the three ML nanocomposites) and SL (black) nanocomposites. At 77 K, the $F_{p,max}$ of the ML_10 nm (2 Hz) nanocomposite is twice of that of SL nanocomposite, while at 65 K, it is about 4.3 times higher. It should be noted that the $F_{p,\,max}$ of ~157 GN/m^3 represents the best reported so far on BZO 1D APC/YBCO nanocomposite, which is more than twice of the highest $F_{p,\,max}$ in the BZO doping range of 2-6 vol.% [72]. Furthermore, the H_{max} value of the ML_10 nm (2 Hz) nanocomposite is 44% higher than its SL counterpart at 77 K, and it increases to 60% at 65 K. This result illustrates the critical importance of the 1D-APC/YBCO interface on the pinning efficiency of the 1D APCs.

Figures 41a-d depict the J_c (H) and F_p (H) curves of three ML nanocomposites of 6 vol.% BZO/YBCO varying Ca spacer layer of 5 nm (green), 10 nm (red) and 15 nm (blue) thick $Ca_{0.3}Y_{0.7}Ba_2Cu_3O_{7-x}$ spacer layers, in comparison with SL nanocomposite (black) at 77 K and 65 K respectively. Again, the ML nanocomposites have overall higher J_c (H) in the entire magnetic field range up to 9.0 T than their SL counterparts, with the enhancement more pronounced at higher fields. This reflects on the F_p (H) curves as well, in which $F_{p,max}$ for all ML nanocomposites are

much higher than the undoped and SL counterparts. Again, the ML nanocomposites have overall higher J_c (H) in the entire magnetic field range up to 9.0 T than their SL counterparts with the enhancement more pronounced at higher fields.

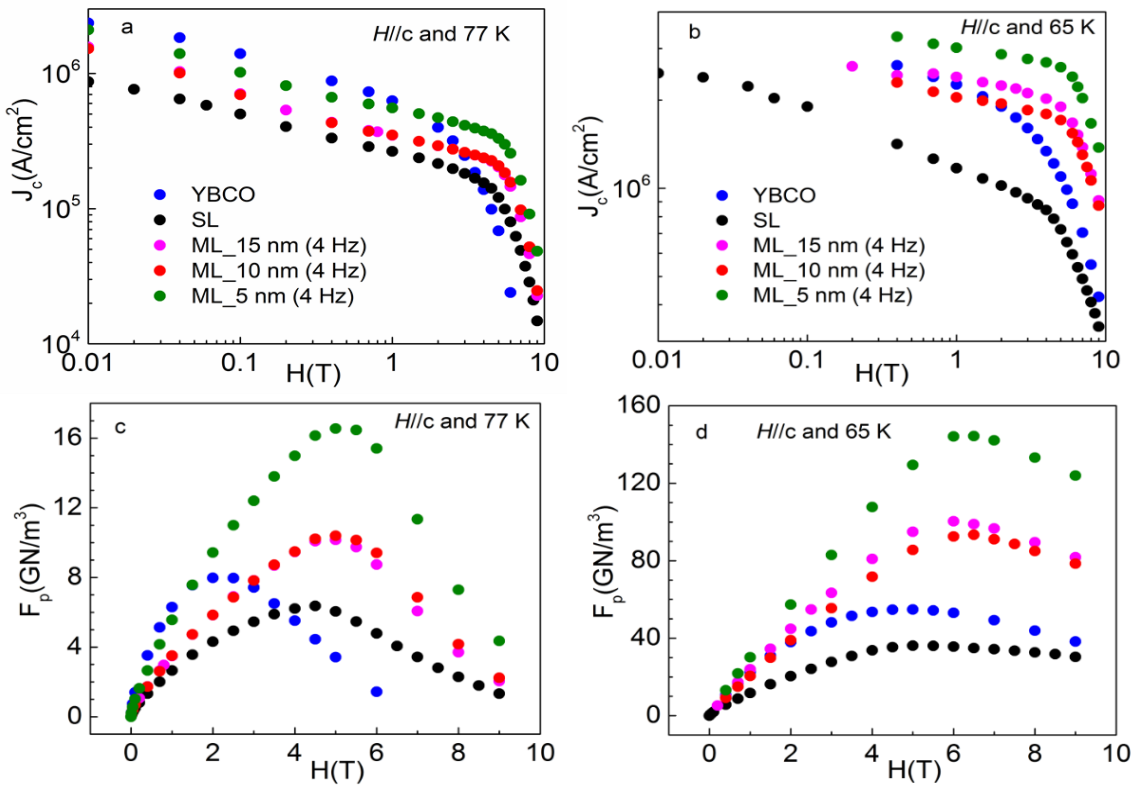

Figure 41: J_c vs. H and F_p vs. H curves measured on 6 vol.% BZO/YBCO named as SL (black) and multilayer films : ML_5 nm (4 Hz) (green), ML_10 nm (4 Hz) (red) and ML_15 nm (4 Hz) (blue) fabricated at same laser repetition rate (RR) of 4 Hz at θ=0° (H//c-axis) (a) and (c) at 77 K, and (b) and (d) at 65 K, respectively. Color codes follow the same for all figures.

Specifically, the $F_{p,\,max}$ ~157.70 GN/m^3 ML_10 nm (2 Hz) is about four times higher than SL film. This observation illustrates that the defective BZO 1D APC/YBCO interface has a more detrimental impact on high-field pinning efficiency. This result is therefore important to the applications that require high performance HTSs in strong fields. At the same time, it further

explores that for the thickness of ~10 nm of CaY-123 spacer layer, the laser RR of ~2 Hz provides the best result of pinning efficiency. Interestingly, in the separate measurements (figures are not included) for the ML_5 nm (4 Hz), the ML_10 nm (4 Hz), and the ML_15 nm (4 Hz) nanocomposite thin films, an identical T_c of 85.0 K is measured. All these films are deposited with the same PLD repetition frequency of 4 Hz. Intuitively, the result indicates that T_c is independent of the thickness of the CaY-123 spacer layer. In addition, it suggests that the diffusion of Ca into the YBCO matrix is less likely to happen by varying the Ca concentration through the thickness of CaY-123 spacer layer. This suggests the precision in controlling the amount of Ca into the interface is important to reach high pinning efficiency and deserves further study.

To add further insight to the pinning efficiency of the ML nanocomposite with respect to SL film, the ratio of $F_{p,max}$ (ML)/$F_{p,max}$ (SL) (black symbols) and H_{max} (ML)/H_{max} (SL) (red symbols) for the ML nanocomposite deposited at different PLD repetition rate at 77 K (solid) and 65 K (open) are compared in Figure 42. Overall, the values of both ratios are in exceeding one (1), suggesting enhanced pinning efficiency by Ca-doping in ML nanocomposites. The $F_{p,max}$ ratio from 1.03, 2.0, and 1.64 for ML_10 nm (1 Hz), ML_10nm (2 Hz), and ML_10 (4 Hz) nanocomposite films at 77 K is increased to 2.27, 4.36, and 2.64 respectively, compared to SL film. This suggests the Ca diffusion is optimized at growth parameter of 2 Hz RR by maximizing the interface repair and minimizing the T_c drop, and enhances the $F_{p,max}$. The $F_{p.max}$ ~157.7 GN/m^3 for ML_10 nm (2 Hz) is the highest reported so far at 65 K, and is about 1.30 and 1.53 times higher than the highest claimed $F_{p,max}$~120.0 GN/m^3, ~103.0 GN/m^3, and 122.0 GN/m^3 for BHO/REBCO, BSO/YBCO, and (BaNbOy + Y_2O_3)/YBCO films, respectively [65, 74, 75].

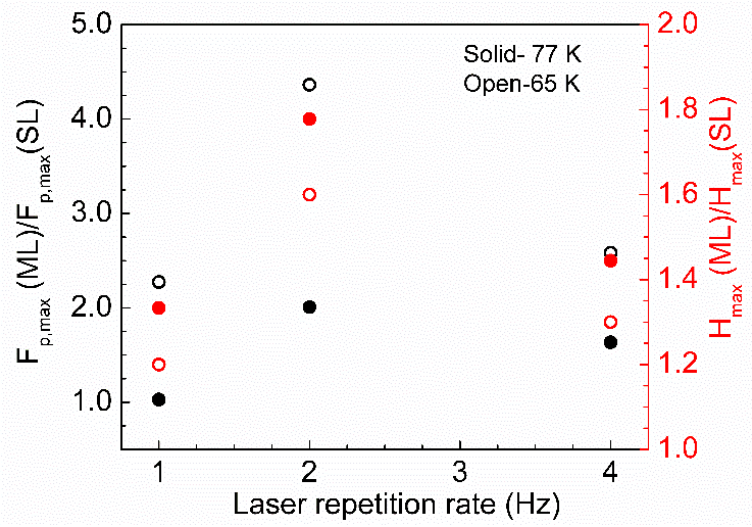

Figure 42: Laser repetition rate (Hz) dependence of ratio of the $F_{p,max}$ (ML)/$F_{p,max}$ (SL) (black) on left Y-axis and H_{max} (red) on right Y-axis measured at 77 K (solid) and at 65 K (open), on H//c-axis of multilayer films.

Calcium diffusion leads to a reduction in the oxygen deficient condition between APC and YBCO matrix of the ML nanocomposite film compared to SL nanocomposite film. The SL film contains high interfacial defects that release the strain field at the 1D APC/YBCO interface. In addition, such reduction of oxygen deficiency in ML film leading to coherent APC/YBCO interface enhances the pinning efficiency.

The higher ratio of H_{max} (ML)/H_{max} (SL) indicates the effective areal density of APCs in the ML film compared to the SL film (Figure 42). The similar trend of the ratio of the H_{max} (ML)/H_{max} (SL) to that of the ratio of the $F_{p,max}$ (ML)/ $F_{p,max}$ (SL) indicates that below or above the specific RR (2 Hz in this study), the pinning strength of APCs is decreased. It further suggests that the Ca diffusion at APC/YBCO interface is particularly dependent on diffusion time through the laser repetition rate that might possibly alter the effectiveness of the 1D APCs. For example, at 77 K, the ratio of H_{max} (ML)/H_{max} (SL) ~1.33 and 1.44 for ML_10 nm (1 Hz), and ML_10 nm (4 Hz)

nanocomposite is lower than that of the ratio of H_{max} (ML)/H_{max} (SL) ~1.78 for ML_10 nm (2 Hz) nanocomposite, which supports the earlier statement. At 65 K, although the ratio of H_{max} (ML)/H_{max} (SL) follows the similar trend, the values are decreased to 1.2, 1.6, and 1.3 for those nanocomposite films, respectively (Figure 42), which suggests the decreasing trend of the effectiveness of APCs in ML nanocomposite films to that of SL film with temperature. In other words, SL film leads to increases in the pinning strength over ML films regarding temperature effect. However, this could indicate that the Ca facilitated APC/YBCO interface in ML films could modify the effectiveness of the microstructure to enhance the pinning strength.

5.4 Conclusions

In this work, we have investigated the correlation of the calcium diffusion at the BZO 1D APC/YBCO interface and pinning efficiency of the BZO 1D APCs through a systematic study of the transport $J_c(H)$ measurements and microstructure analysis of the 6 vol.% BZO+YBCO/$Ca_{0.3}Y_{0.7}Ba_2Cu_3O_{7-x}$ (CaY-123) multilayer (ML) nanocomposite films. Those results are compared to 6 vol.% BZO+YBCO single layer (SL) nanocomposite film as well. The key findings of these results are as follows.

The pinning efficiency of ML film is almost independent of the thickness of the CaY-123 spacer layer while it is dependent on the laser RR. It is observed that the higher $F_{p,max}$ for RR of 2

Hz and lower $F_{p,max}$ on either low or high RR for fixed CaY-123 thickness of 10 nm indicate that higher diffusion time may not be favorable for Ca diffusion.

Compared to the pinning force density $F_{p,max}$ ~36 GN/m^3 at H_{max} ~5.0 T of SL film at 65 K, a much higher pinning force density, $F_{p,max}$ ~157 GN/m^3 at H_{max} ~8.0 T for the best results ML film is found.

The significantly lower pinning efficiency in terms of $F_{p,max}$ and H_{max} in high doping of BZO is mainly due to defective 1D APC/YBCO interface leading to severe oxygen deficiency. In ML films, the enhanced pinning efficiency must be due to reducing the oxygen deficiency condition and maintaining coherent 1D APC/YBCO interface via calcium diffusion.

Chapter 6 Conclusions and Future Directions

6.1 Conclusions

The high critical current density of superconductors has led to many applications in the field of telecommunications, electric power generation, and medical application in magnetic resonance imaging (MRI). A type II superconductor, such as Yttrium barium copper oxide, $YBa_2Cu_3O_{7-x}$ (YBCO), with T_c~92 K, has the potential to have a high critical current density ~10^8 A/cm^2. However, reduction of critical current density (J_c) due to the vortex motion is an issue when the high magnetic field application is required. J_c anisotropy due to the structure of YBCO itself and magnetic field orientation J_c is another issue for devices such as motors and generators. For the applications, these devices require J_c independent of the orientation of the magnetic field. The addition of secondary phase nanoinclusions enhances flux pinning and subsequently increases the critical current density by incorporating additional artificial pinning centers (APCs). Many previous studies have been focused to generate APCs with specific dimensions and morphology to improve the vortex pinning and current density by combining different pinning mechanisms. However, the challenge remains to generate an optimal pinning landscape of APCs to enhance the isotopic pinning with mixed APC morphology and pinning efficiency of the specific APCs. The first objective of this thesis was to generate the controllable APC pinning landscape to enhance strong and isotropic pinning. The second objective was to explore the effect of the 1D APC/YBCO interface on pinning efficiency of different doping materials. The third objective was to study the diffusion of calcium at the APC/YBCO interface to improve the pinning efficiency of 1D APC in

repairing a defective APC/YBCO interface, especially to reduce the oxygen deficient condition by addition of calcium-rich materials as a spacer layer.

To fulfill the first objective, electrical transport properties were carried out on 2-6 vol.% BZO (and BHO) plus 3 vol.% Y_2O_3 at their optimal growth temperature and those results correlate with the nanostructure morphology through TEM images. Doping materials were added to YBCO targets to generate mixed phase nanoinclusions in nanocomposite films during pulsed laser deposition (PLD) on single crystal (100) $SrTiO_3$ substrates. As illustrated in Figure 14, the material of less lattice mismatch with YBCO and less rigid to form *c*-axis aligned 1D APCs can form mixed (1D+2D+3D) APCs morphology. A landscape of mixed APCs morphology is essential to provide strong isotropic pinning. A low volume (2 vol.%) of less rigid materials such as BHO (form 1D APCs) was mixed with 3 vol.% of Y_2O_3 (form 3D APCs) to deposit BHO/YBCO double doped nanocomposite films. $J_c(H, T, \theta)$ values were measured for those nanocomposite films at different temperatures and at different magnetic field varying orientations from *H*//*c*-axis to *H*//*ab*-plane**.** The results were compared to the same volume of BZO dopant mixed 3 vol.% Y_2O_3. From the results of the electrical transport measurement, significantly low J_c anisotropy ~18% was calculated for 2 vol.% BHO+ 3 vol.% Y_2O_3 at 65 K and at 9.0 T due to the mixed APCs morphologies. The result was consistent with the mixed nanostructures observed from TEM images.

Keeping 3.0 vol.% Y_2O_3 constant, the BHO (and BZO) concentration was increased to 6 vol.% and the electrical transport measurement was conducted. As usual, the results correlated

with the nanostructure morphology obtained from TEM images. At lower doping (2 vol.%) nanocomposite films, the overall higher $J_c(H, T, \theta)$ was observed for BHO doped film compared to BZO doped film. Surprisingly, at higher doping (6 vol.%) of nanocomposite film, $J_c(H, T, \theta)$ doesn't show the similar trend of results as observed in lower doping (2 vol.%). The 6 vol.% BZO doped films showed overall strong isotropic pinning; and hence higher J_c (H//c-axis), and J (θ) for the entire angular range of $\theta=0^o$ (H//c-axis), to 90^o(H//ab-plane), except J_c peak at H//ab-plane for 6 vol.% BHO DD film. This could be possible if the direction of alignment for **a** significant number of 1D APCs were switched from *c*-axis to *ab*-plane. The results of the transport measurements agreed to TEM images. Many BHO 1D APCs were observed s being aligned along *ab*-plane by connecting short and segmented APCs. This allowed a room to study concentration dependence of BHO DD film. A significantly reduced J_c anisotropy is found in 2-4 vol.% BHO DD films due to the formation of short, misaligned and mixed APCs morphologies enhancing isotropic pinning. When BHO doping is increased to 6 vol.%, a significant number of *c*-axis aligned 1D APCs are switched to *ab*-plane aligned 1D APCs and hence J_c anisotropy is increased**.** The overall best J_c (H, θ) was observed for 4 vol.% BHO DD nanocomposite films at 65-77 K. This suggested that double doping is an effective approach for the generation of mixed APCs morphology and engineering the strong and isotropic pinning landscape only up to moderate doping of BHO (4 vol.%) and BZO (6 vol.%) in this study.

To explore the effect of interface on pinning efficiency of 1D APCs, J_c in 2.0-6.0 vol.% BZO/YBCO and 2.0-4.0 vol.% BHO/YBCO nanocomposite thin films were measured. A

significantly high $F_{p,max}$ ~182 GN/m^3 at 65 K for 4 vol.% BHO/YBCO was found**.** Such a high value of $F_{p,max}$ could only be possible for a sharp APC/YBCO interface (a coherent interface). Thus, a highly coherent BHO 1DAPC/YBCO interface was concluded qualitatively, which could be due to low rigidity of the BHO 1D APCs and their smaller lattice mismatch with the YBCO matrix. A semicoherent BZO 1D APC/YBCO was due to less adaptive BZO lattice and a comparatively higher lattice mismatch with the YBCO matrix. This resulted in the interfacial defect which was one of the prime causes of lowering pinning efficiency.

Calcium-rich spacer layer was added to a high volume of 6 vol.% BZO/YBCO nanocomposite to repair the defective APC/YBCO interfaces expecting to increase pinning efficiency of 1D APCs. The results were compared with the same doping concentration of BZO/YBCO single layer film. The experimental results suggest that calcium was induced at the APC/YBCO interface. The induced calcium at the interface might repair the defective interface between 1D APC/YBCO matrix and hence enhanced the pinning efficiency of the BZO 1D APCs. Compared to $F_{p,\,max}$ ~36 GN/m^3 at H_{max} ~5.0 T of single layer film at 65 K, a significantly higher pinning force density, $F_{p,\,max}$ ~157 GN/m^3 at H_{max} ~8.0 T for the best results multilayer film was found. The best result multilayer film was deposited with CaY-123 spacer layers of thickness of 10 nm at 2 Hz of laser repetition rate of PLD. Pinning efficiency of 1D APCs was dependent on Ca diffusion time which could be controlled through the repetition rate of PLD while the ML were deposited.

6.2 Future directions

Even though we have addressed several important current issues of the control landscape of APCs for isotropic pinning, many questions remain unanswered about pinning efficiency of the APCs and interface effect. Theoretical and experimental researches may begin to address them in the future. Quantitative evaluation of pinning efficiency and accommodation field H^* need to be addressed for controlling the pinning landscape of APCs morphology. Strain distributions at the vicinity of APC/YBCO remain a challenge because they are unclear in the present experiments.

Future work could progress towards several directions: whether it may require further analyzing the vortex pinning mechanism or new doping materials need to be investigated which may reduce the interfacial strain between APC/YBCO matrix. One of the immediate works could progress on the continuation of the current work of pinning efficiency of BHO/YBCO nanocomposite thin films. These films could be evaluated at the low temperature of 20-50 K and at the high field of 20 T. In this work, a high-resolution TEM analysis is lacking for the complete evaluation of defective interface or oxygen deficiency mapping which could be done for future work. Experimental results presented henceforth confirm the strong pinning of vortices and higher pinning efficiency of 1D APCs with the coherent APC/YBCO interface**.** Theoretical studies would be useful for further explanation of strong pinning of 1D APCs.

Analysis of accommodation field (H^*) and pinning force density (F_p) indicate that all APCs are not involved in the effective pinning of the vortices. Only a fraction of APCs is efficient pins. An immediate question is; what determines the pinning efficiency, and to what extent? The

sharpness of the APC/YBCO interface at an atomic level is related to the pinning potential, and an optimal pinning efficiency, future work may focus on this direction. For this; it may need to introduce new doping materials with much less lattice mismatch to YBCO matrix and can form comparatively smaller diameter of 1D APCs. In addition, calcium-rich compounds would be useful to repair the defective interface because we have shown that Ca diffusion at the APC/YBCO interface increases the pinning efficiency of 1D APCs in the multilayer film.

Out of many materials, $CaHfO_3$ with lattice mismatch ~1.5% to YBCO (less than lattice mismatch ~6.7% of BHO to YBCO) could be one of the options of doping material [87]. This material could form 1D APC of the diameter close to the diameter of BHO 1D APCs or even smaller than BHO 1D APCs. Calcium itself may repair the defective APC/YBCO interface.

References:

1. Narlikar, A.V., Superconductors. 2014: Oxford University Press.
2. Kittel, C., Introduction to Solid State Physics. 2004: Wiley.
3. Narlikar, A.V., High Temperature Superconductivity 1: Materials. 2004: Springer.
4. Saxena, A.K., High-Temperature Superconductors. Vol. 125. 2012: Springer Science & Business Media.
5. Norton, D.P., Synthesis and properties of epitaxial electronic oxide thin-film materials. Materials Science and Engineering: R: Reports, **43**.5-6 (2004): 139-247.
6. Bednorz, J.G. and K.A. Müller, Perovskite-type oxides—the new approach to high-Tc superconductivity. Reviews of Modern Physics, **60**.3 (1988): 585.
7. Chu, C.W., Superconductivity above 90 K. Proceedings of the National Academy of United States of America **84**.14 (1987): 4681.
8. Erbe, M., et al., BaHfO3 artificial pinning centres in TFA-MOD-derived YBCO and GdBCO thin films. Superconductor Science and Technology, 2015. **28**(11): p. 114002.
9. Miura, S., et al., Vortex pinning at low temperature under high magnetic field in SmBa2Cu3O y superconducting films with high number density and small size of BaHfO3 nano-rods. Superconductor Science and Technology, 2015. **28**(11): p. 114006.
10. Miura, S., et al., Characteristics of high-performance BaHfO3-doped SmBa2Cu3Oy superconducting films fabricated with a seed layer and low-temperature growth. Superconductor Science and Technology, 2015. **28**(6): p. 065013.
11. Gutierrez, J., et al., Strong isotropic flux pinning in solution-derived YBa 2 Cu 3 O 7− x nanocomposite superconductor films. Nature materials, 2007. **6**(5): p. 367.
12. Ichinose, A., et al., Microstructures and critical current densities of YBCO films containing structure-controlled BaZrO3 nanorods. Superconductor Science and Technology, 2007. **20**(12): p. 1144.
13. Gautam, B., et al., Transformational dynamics of BZO and BHO nanorods imposed by Y2O3 nanoparticles for improved isotropic pinning in YBa2Cu3 O7-δ thin films. AIP Advances, 2017. **7**(7): p. 075308.
14. Blatter, G., et al., Vortices in high-temperature superconductors. Reviews of Modern Physics, 1994. **66**(4): p. 1125.
15. Llordes, A., et al., Nanoscale strain-induced pair suppression as a vortex-pinning mechanism in high-temperature superconductors. Nature materials, 2012. **11**(4): p. 329.

16. Yamasaki, H., Effect of particle size on the flux pinning properties of YBa2Cu3O7–δ thin films containing fine Y2O3 nanoprecipitates. Superconductor Science and Technology, **29**, no. 6 (2016): 065005.

17. Baca, F.J.A., In-Situ Control of BaZrO3 and BaSnO3 Nanorod Alignment and Microstructure in YBa 2 Cu 3 O 7-x Thin Films by Strain Modulated Growth. 2009, University of Kansas.

18. Emergo, R., et al., The effect of thickness and substrate tilt on the BZO splay and superconducting properties of YBa2Cu3O7− δ films. Superconductor Science and Technology, 2010. **23**(11): p. 115010.

19. der Beek, V.C.J., M. Konczykowski, and A. Abal'oshev, Strong pinning in high-temperature superconducting films. Physical Review B, **66.**2 (2002): 024523.

20. Shi, J.J. and J.Z. Wu, Structural transition of secondary phase oxide nanorods in epitaxial YBa2Cu3O7− δ films on vicinal substrates. Philosophical Magazine, 2012. **92**(34): p. 4205-4214.

21. Obradors, X. and T. Puig, Coated conductors for power applications: materials challenges. Superconductor Science and Technology, 2014. **27**(4): p. 044003.

22. Tsuruta, A., et al., The influence of the geometric characteristics of nanorods on the flux pinning in high-performance BaMO3-doped SmBa2Cu3Oy films (M=Hf, Sn). Superconductor Science and Technology **27.6** (2014): 065001.

23. Miura, S., et al., Flux pinning properties and microstructures of a SmBa2Cu3Oy film with high number density of BaHfO3 nanorods deposited by using low-temperature growth technique. Japanese Journal of Applied Physics, 2014. **53**(9): p. 090304.

24. Pahlke, P., et al., Reduced Jc Anisotropy and Enhanced In-Field Performance of Thick BaHfO 3-Doped YBa2Cu3O7-x Films on ABAD-YSZ Templates. IEEE Transactions on Applied Superconductivity, 2016. **26**(3): p. 1-4.

25. Goyal, A., et al., Irradiation-free, columnar defects comprised of self-assembled nanodots and nanorods resulting in strongly enhanced flux-pinning in YBa2Cu3O7− δ films. Superconductor Science and Technology, 2005. **18**(11): p. 1533.

26. Matsui, V., et al., Current-carrying abilities of nano-structured HTS thin films. Journal of Nanoscience and Nanoengineering, 2015. **1**(2): p. 38-43.

27. Horide, T., et al., Influence of matching field on critical current density and irreversibility temperature in YBa2Cu3O7 films with BaMO3 (M= Zr, Sn, Hf) nanorods. Applied Physics Letters, 2016. **108**(8): p. 082601.

28. Matsumoto, K. and P. Mele, Artificial pinning center technology to enhance vortex pinning in YBCO coated conductors. Superconductor Science and Technology, 2009. **23**(1): p. 014001.

29. Baca, F., et al., Control of BaZrO 3 nanorod alignment in YBa 2 Cu 3 O 7− x thin films by microstructural modulation. Applied Physics Letters, 2009. **94**(10): p. 102512.

30. Jha, A.K., et al., Controlling the critical current anisotropy of YBCO superconducting films by incorporating hybrid artificial pinning centers. IEEE Transactions on Applied Superconductivity, 2016. **26**(3): p. 1-4.

31. Ercolano, G., et al., State-of-the-art flux pinning in YBa2Cu3O7− δ by the creation of highly linear, segmented nanorods of Ba2 (Y/Gd)(Nb/Ta) O6 together with nanoparticles of (Y/Gd) 2O3 and (Y/Gd) Ba2Cu4O8. Superconductor Science and Technology, 2011. **24**(9): p. 095012.

32. Obradors, X., et al., Growth, nanostructure and vortex pinning in superconducting YBa2Cu3O7 thin films based on trifluoroacetate solutions. Superconductor Science and Technology, 2012. **25**(12): p. 123001.

33. Jha, A.K., et al., Systematic variation of hybrid APCs into YBCO thin films for improving the vortex pinning properties. IEEE Transactions on Applied Superconductivity, 2014. **25**(3): p. 1-5.

34. Baca, F.J., et al., Interactive Growth Effects of Rare-Earth Nanoparticles on Nanorod Formation in YBa2Cu3Ox Thin Films. Advanced Functional Materials, 2013. **23**(38): p. 4826-4831.

35. Horide, T., et al., Jc improvement by double artificial pinning centers of BaSnO3 nanorods and Y2O3 nanoparticles in YBa2Cu3O7 coated conductors. Superconductor Science and Technology, 2013. **26**(7): p. 075019.

36. Wu, J.Z., et al., The effect of lattice strain on the diameter of BaZrO3 nanorods in epitaxial YBa2Cu3O7− δ films. Superconductor Science and Technology, 2014. **27**(4): p. 044010.

37. Horide, T., et al., Geometric and compositional factors on critical current density in YBa2Cu3O7− δ films containing nanorods. Superconductor Science and Technology, 2018. **31**(6): p. 065012.

38. Cantoni, C., et al., Strain-driven oxygen deficiency in self-assembled, nanostructured, composite oxide films. Acs Nano, 2011. **5**(6): p. 4783-4789.

39. Gautam, B., et al., Probing the effect of interface on vortex pinning efficiency of one-dimensional BaZrO3 and BaHfO3 artificial pinning centers in YBa2Cu3O7-x thin films. Applied Physics Letters, 2018. **113**(21): p. 212602.

40. McLaren, A.C., Transmission electron microscopy of minerals and rocks. Vol. 2. 2005: Cambridge University Press.

41. Maiorov, B., et al., Synergetic combination of different types of defect to optimize pinning landscape using BaZrO 3-doped YBa 2 Cu 3 O 7. Nature materials, 2009. **8**(5): p. 398.

42. Malmivirta, M., et al., Three ranges of the angular dependence of critical current of BaZrO3 doped YBa2Cu3O7− δ thin films grown at different temperatures. Thin Solid Films, 2014. **562**: p. 554-560.

43. Wu, J., et al., Controlling BaZrO3 nanostructure orientation in YBa2Cu3O films for a three-dimensional pinning landscape. Superconductor Science and Technology, 2015. **28**(12): p. 125009.

44. Guzman, R., et al., Strain-driven broken twin boundary coherence in YBa2Cu3O7− δ nanocomposite thin films. Applied Physics Letters, 2013. **102**(8): p. 081906.

45. Chepikov, V., et al., Introduction of BaSnO3 and BaZrO3 artificial pinning centres into 2G HTS wires based on PLD-GdBCO films. Phase I of the industrial R&D programme at SuperOx. Superconductor Science and Technology, 2017. **30**(12): p. 124001.

46. Huhtinen, H., et al., The effect of BZO doping concentration and thickness dependent properties of YBCO films grown by PLD on buffered NiW substrates. Physica C: Superconductivity, 2012. **472**(1): p. 66-74.

47. Teranishi, R., et al., Superconducting properties of ErBCO films with BaMO3 nanorods (M= Zr and Sn) by pulsed laser deposition. Physica C: Superconductivity, 2008. **468**(15-20): p. 1522-1526.

48. Miura, S., et al., Superconducting properties in SmBa 2 Cu 3 O y films with high density of BaHfO 3 Nanorods fabricated with a seed layer. IEEE Transactions on Applied Superconductivity, 2015. **25**(3): p. 1-4.

49. Sebastian, M.A.P., et al., Study of the Flux Pinning Landscape of YBCO Thin Films With Single and Mixed Phase Additions BaMO3+ Z: M= Hf, Sn, Zr and Z= Y2O3, Y211. IEEE Transactions on Applied Superconductivity, 2017. **27**(4): p. 1-5.

50. Mele, P., et al., Ultra-high flux pinning properties of BaMO3-doped YBa2Cu3O7− x thin films (M= Zr, Sn). Superconductor Science and Technology, 2008. **21**(3): p. 032002.

51. Matsumoto, K., et al., Irreversibility fields and critical current densities in strongly pinned YBa2Cu3O7-x films with BaSnO3 nanorods: The influence of segmented BaSnO3 nanorods. Journal of Applied Physics, 2014. **116**(16): p. 163903.

52. Mele, P., et al., Incorporation of double artificial pinning centers in YBa2Cu3O7− d films. Superconductor Science and Technology, 2007. **21**(1): p. 015019.

53. Shi, J.J. and J.Z. Wu, Micromechanical model for self-organized secondary phase oxide nanorod arrays in epitaxial YBa2Cu3O7− δ films. Philosophical Magazine, 2012. **92**(23): p. 2911-2922.

54. Wu, J. and J. Shi, Interactive modeling-synthesis-characterization approach towards controllable in situ self-assembly of artificial pinning centers in RE-123 films. Superconductor Science and Technology, 2017. **30**(10): p. 103002.

55. Sieger, M., et al., BaHfO3 Doped Thick YBa2Cu3O7-x Films on Highly Alloyed Textured Ni-W Tapes. IEEE Transactions on Applied Superconductivity, 2014. **25**(3): p. 1-4.

56. Watanebe, M., et al. Experimental study in the development of HTS NMR probe. in Journal of Physics: Conference Series. Vol. 507. No. 1. IOP Publishing, 2014.

57. Sieger, M., et al., Tailoring microstructure and superconducting properties in thick BaHfO3 and Ba2 Y (Nb/Ta) O6 doped YBCO films on technical templates. IEEE Transactions on Applied Superconductivity, 2016. **27**(4): p. 1-7.

58. Gautam, B., et al., Microscopic adaptation of BaHfO3 and Y2O3 artificial pinning centers for strong and isotropic pinning landscape in YBa2Cu3O7–x thin films. Superconductor Science and Technology, 2018. **31**(2): p. 025008.

59. Ding, F., et al., Enhanced flux pinning in MOD-YBCO films with co-doping of BaZrO3 and Y2O3 nanoparticles. Journal of Alloys and Compounds, 2012. **513**: p. 277-281.

60. Chen, S., et al., Enhancement of isotropic pinning force in YBCO films with BaZrO3 nanorods and Y2O 3 nanoparticles. IEEE Transactions on Applied Superconductivity, 2016. **27**(4): p. 1-5.

61. Gautam, B., et al., Mixed Artificial Pining Centers by Single-Doping BaZrO3 and Double-Doping BaZrO3 +Y2O3 YBa2Cu3O7−x on Flat and Vicinal Substrates. IEEE Transactions on Applied Superconductivity, 2018. **28**(4): p. 1-4.

62. Wu, J., et al., Probing microscopic strain interplay due to impurity doping and vicinal growth and its effect on pinning landscape in YBCO films. IEEE Transactions on Applied Superconductivity, 2015. **25**(3): p. 1-5.

63. Baca, F.J., et al., Microstructural Characterization of YBa2Cu3O7- x Films With BaZrO3 Nanorods Grown on Vicinal SrTiO3 Substrates. IEEE Transactions on Applied Superconductivity, 2009. **19**(3): p. 3371-3374.

64. Huhtinen, H., et al., Superconducting Properties of Films Deposited From Micro-, Nanocrystalline and Optimally BZO-Doped YBCO Targets. IEEE Transactions on Applied Superconductivity, 2007. **17**(2): p. 3620-3623.

65. Mele, P., et al., Systematic study of BaSnO3 doped YBa2Cu3O7− x films. Physica C: Superconductivity, 2009. **469**(15-20): p. 1380-1383.

66. Wang, F., Superconducting properties enhancement of YBa 2 Cu 3 O 7− δ thin films by BaSnO 3 doping. Journal of Materials Science: Materials in Electronics, 2016. **27**(7): p. 7084-7088.

67. Tobita, H., et al., Fabrication of BaHfO3 doped Gd1Ba2Cu3O7− δ coated conductors with the high Ic of 85 A/cm-w under 3 T at liquid nitrogen temperature (77 K). Superconductor Science and Technology, 2012. **25**(6): p. 062002.

68. Sieger, M., et al. Pulsed laser deposition of thick BaHfO3-doped YBa2Cu307-δ films on highly alloyed textured Ni-W tapes. in Journal of Physics: Conference Series. Volume 507, Part 2, 2014. IOP Publishing.

69. Opherden, L., et al., Large pinning forces and matching effects in $YBa_2Cu_3O_{7-\delta}$ thin films with Ba_2Y (Nb/Ta)O_6 nano-precipitates. Scientific reports, **6** (2016): 21188..

70. Horide, T., et al., Structural Evolution Induced by Interfacial Lattice Mismatch in Self-Organized YBa2Cu3O7− δ Nanocomposite Film. ACS nano, 2017. **11**(2): p. 1780-1788.

71. Jorgensen, J., et al., Structural properties of oxygen-deficient YBa 2 Cu 3 O 7− δ. Physical Review B, 1990. **41**(4): p. 1863.

72. Wee, S.H., et al., Engineering nanocolumnar defect configurations for optimized vortex pinning in high temperature superconducting nanocomposite wires. Scientific reports, 2013. **3**: p. 2310.

73. Emergo, R.L.S., Enhancing Jc (B, theta) in YBa2Cu3O7-delta via nano-engineering of pinning structures. 2009, University of Kansas.

74. Miura, S., et al., Strongly enhanced irreversibility field and flux pinning force density in SmBa2Cu3O y-coated conductors with well-aligned BaHfO3 nanorods. Applied Physics Express, 2017. **10**(10): p. 103101.

75. Feldmann, D., et al., Improved flux pinning in YBa2Cu3O7 with nanorods of the double perovskite Ba2YNbO6. Superconductor Science and Technology, 2010. **23**(9): p. 095004.

76. Jha, A.K., et al., Tailoring the vortex pinning strength of YBCO thin films by systematic incorporation of hybrid artificial pinning centers. Superconductor Science and Technology, 2015. **28**(11): p. 114004.

77. Schmehl, A., et al., Doping-induced enhancement of the critical currents of grain boundaries in YBa2Cu3O7− δ. EPL (Europhysics Letters), 1999. **47**(1): p. 110.

78. Talantsev, E., et al., Oxygen deficiency, stacking faults and calcium substitution in MOD YBCO coated conductors. IEEE Transactions on Applied Superconductivity, 2013. **23**(3): p. 7200205-7200205.

79. Hammerl, G., et al., Enhanced supercurrent density in polycrystalline YBa2Cu 3O7-δ at 77 K from calcium doping of grain boundaries. Nature, 2000. **407**(6801): p. 162-164.

80. Daniels, G.A., A. Gurevich, and D.C. Larbalestier, Improved strong magnetic field performance of low angle grain boundaries of calcium and oxygen overdoped YBa 2 Cu 3 O x. Applied Physics Letters, 2000. **77**(20): p. 3251-3253.

81. Song, X., et al., Electromagnetic, atomic structure and chemistry changes induced by Ca-doping of low-angle YBa 2 Cu 3 O 7–δ grain boundaries. Nature Materials, 2005. **4**(6): p. 470.

82. Zhu, Y., et al., Interfacial defects distribution and strain coupling in the vertically aligned nanocomposite YBa 2 Cu 3 O 7-X/BaSnO 3 thin films. Journal of Materials Research, 2012. **27**(13): p. 1763-1769.

83. Luo, C., et al. Ultrafast dynamics in oxygen-deficient Y0. 7Ca0. 3Ba2Cu3O7-δ superconductors. in Journal of Physics: Conference Series. Volume 150, Part 2, 2009. IOP Publishing.

84. Malmivirta, M., et al., Enhanced flux pinning in YBCO multilayer films with BCO nanodots and segmented BZO nanorods. Scientific reports, 2017. **7**(1): p. 14682.

85. Chen, S., et al., Generating mixed morphology BaZrO3 artificial pinning centers for strong and isotropic pinning in BaZrO3–Y2O3 double-doped YBCO thin films. Superconductor Science and Technology, 2017. **30**(12): p. 125011.

86. Petrisor, T., et al., The Vortex Path Model Analysis of the Field Angle Dependence of the Critical Current Density in Nanocomposite YBa 2 Cu 3 O 7− x–BaZrO 3 Films Obtained by Low Fluorine Chemical Solution Deposition. Journal of Superconductivity and Novel Magnetism, 2014. **27**(11): p. 2493-2500.

87. Verma, A. and V. Jindal, Lattice constant of cubic perovskites. Journal of Alloys and Compounds, 2009. **485**(1-2): p. 514-518.

List of Publications:

1. **B. Gautam** et. al. "Probing the effect of interface on vortex pinning efficiency of one-dimensional $BaZrO_3$ and $BaHfO_3$ artificial pinning centers in $YBa_2Cu_3O_{7-x}$ thin films" *Appl. Phys. Lett.* ***113****, 212602 (2018)*

2. **B. Gautam** et.al "Microscopic adaptation of $BaHfO_3$ and Y_2O_3 artificial pinning centers for strong and isotropic pinning landscape in $YBa_2Cu_3O_{7-x}$ thin films" 2018 *Supercond. Sci. Technol.* **31** 025008

3. **B. Gautam** et. al. "Mixed Artificial Pinning Centers by Single-Doping BaZrO3 and Double-Doping BaZrO3+ Y2O3 YBa2Cu3O7-x on Flat and Vicinal Substrates" IEEE Transactions on Applied Superconductivity, 28(4), June 2018

4. **B. Gautam** et. al. "Transformational dynamics of BZO and BHO nanorods imposed by Y_2O_3 nanoparticles for improved isotropic pinning in $YBa_2Cu_3O7-\delta$ thin films" AIP Advances **7**, 075308 (2017)

5. **B. Gautam** et. al "Towards Isotropic Vortex Pinning in YBCO Films with Double-doping BHO-Y_2O_3 and BZO-Y_2O_3 Artificial Pinning Centers" 2017 *IOP Conf. Ser.: Mater. Sci. Eng.* **279** 012030

6. S. Chen, **B. Gautam** et. al "Enhancement of Isotropic Pinning Force in YBCO Films With $BaZrO_3$ Nanorods and Y_2O_3 Nanoparticles" IEEE Transactions on Applied Superconductivity, 27(4) June 2017

7. S. Chen, **B. Gautam** et. Al "Generating mixed morphology $BaZrO_3$ artificial pinning centers for strong and isotropic pinning in $BaZrO_3$–Y_2O_3 double-doped YBCO thin films" 2017 *Supercond. Sci. Technol.* **30** 125011

8. M.A. Sebastian, **B. Gautam** et.al "Comparison Study of the Flux Pinning Enhancement of YBa2Cu3O7−δ Thin Films With BaHfO3 + Y2O3 Single- and Mixed-Phase Additions" IEEE Transactions on Applied Superconductivity (Volume: 29 , Issue: 5 , Aug. 2019)

9. M.A. Sebastian, **B. Gautam** et.al "Comparison study of the flux pinning enhancement of YBCO superconductor with BZO and BZO + Y2O3 mixed phase additions" 2017 *IOP Conf. Ser.: Mater. Sci. Eng.* **279** 012031

10. J. Wu, **B. Gautam** et al. "Pinning Efficiency of One-Dimensional Artificial Pinning Centers in YBa2Cu3O7-x Thin Films" IEEE Transactions on Applied Superconductivity (Volume: 29 , Issue: 5 , Aug. 2019)

11. J. Wu, **B. Gautam et. al**. a book chapter entitled "Pinning Efficiency of Artificial Pinning Centers in Superconductor Nanocomposite Films" Springer Publication Inc. (Submitted),